ALMA MATER STUDIORUM
UNIVERSITÀ DI BOLOGNA

DOTTORATO DI RICERCA IN

MECCANICA E SCIENZE AVANZATE DELL'INGEGNERIA

Ciclo 38

Settore Concorsuale: 09/C2 - FISICA TECNICA E INGEGNERIA NUCLEARE

Settore Scientifico Disciplinare: ING-IND/18 - FISICA DEI REATTORI NUCLEARI

UNCERTAINTY QUANTIFICATION AND DATA ASSIMILATION FRAMEWORK TOWARDS THE VALIDATION OF MCNP FOR LFR APPLICATIONS

Presentata da: Laura Laghi

Coordinatore Dottorato

Lorenzo Donati

Supervisore

Domiziano Mostacci

Co-supervisore

Sandro Manservisi

Giacomo Grasso

Esame finale anno 2026

A Lucia,
a 10 anni di profonda amicizia,
sfide quotidiane, viaggi incredibili
(e forse qualche scelta discutibile)

A chi amo, a chi scelgo,
voglio offrire una sola rassicurazione:
quella di non dover mai fingere di non essere chi è.
Michela Murgia

In peace, may you leave this shore.
In love, may you find the next.
Safe passage on your travels, until our final journey to the ground.
May we meet again.
The Traveler's Blessing, The 100

Abstract

The qualification of computational tools for nuclear reactor design requires rigorous verification, validation, and uncertainty quantification. Validation and uncertainty quantification depend on the availability of experimental databases. While for traditional technologies the long operational experience has provided abundant and well-documented measurements, in the context of Lead-cooled Fast Reactors (LFRs), where such data remain limited, international benchmark projects may play an essential role. This work focuses on the uncertainty quantification to support the qualification of the MCNP Monte Carlo code for LFR applications, with specific reference to the ALFRED demonstrator.

During this PhD project, a set of experiments representative of ALFRED was carefully selected from the International Handbook of Evaluated Reactor Physics Benchmark Experiments (IRPhE) maintained by OECD-NEA, and then simulated to evaluate the MCNP accuracy in computing the criticality and reactivity effects, including the effective multiplication factor, control rod worth, sodium void reactivity, and isothermal temperature coefficient.

A dedicated Python-based framework was developed to perform post-processing, uncertainty propagation, and data assimilation. The uncertainty quantification is based on the use of sensitivity coefficients, which were calculated by MCNP with respect to the nuclide cross sections and subsequently combined with the covariance matrix to propagate nuclear data uncertainties. In addition, the Generalized Linear Least Squares (GLLS) data assimilation tool was implemented to evaluate the potential improvements of integrating experimental information to obtain a more accurate prediction for the ALFRED k_{eff} estimation. Both methodologies were thoroughly verified by comparing results from a test case with TSUNAMI-IP, a package from the SCALE code, and with the NEA SG11 intercomparison exercise.

Overall, the developed post-processing and data analysis framework provides a flexible and rigorous tool for quantifying the impact of nuclear data uncertainties on several reactivity parameters obtained from MCNP simulations and for updat-

ing model predictions through data assimilation with available measurements.

The results demonstrate good agreement with experimental data, in most cases falling within one standard deviation of total uncertainty. Nuclear data were identified as the dominant uncertainty source across all cases, while statistical contributions were generally negligible. The results of the GLLS analyses also revealed the potential for a significant improvement in the evaluation accuracy that could be obtained through nuclear data adjustment. This opportunity clearly suggests further investigations to extend the scope and confirm the preliminary results here reported before inclusion in a validation dossier.

Contents

List of Figures

List of Tables

Listings

Acronyms

ADS Accelerator Driven Systems.

ALFRED Advanced Lead-cooled Fast Reactor European Demonstrator.

ASN French Nuclear Safety Authority.

CRW Control Rod Worth.

DA Data Assimilation.

DOE U.S. Department of Energy.

ENEA Italian National Agency for New Technologies, Energy and Sustainable Economic Development.

GIF Generation IV International Forum.

GLLS Generalized Linear Least Square.

IAEA International Atomic Energy Agency.

ICSBEP International Criticality Safety Benchmark Evaluation Project.

IRPhE International Reactor Physics Evaluation.

ITC Isothermal Temperature Coefficient.

LFR Lead-cooled Fast Reactor.

LMFR Liquid Metal-cooled Fast Reactors.

LWRs Light Water Reactors.

M&S Modeling and Simulation.

MCNP Monte Carlo N-Particle code.

MOX Mixed Oxide Fuel.

NEA Nuclear Energy Agency.

NRC U.S. Nuclear Regulatory Commission.

SFR Sodium-cooled Fast Reactor.

SVR Sodium Void Reactivity.

UQ Uncertainty Quantification.

WPNCS Working Party on Nuclear Criticality Safety.

Chapter 1

Introduction

1.1 General Context - Nuclear Power landscape

In the last decade, global energy demand grew at a 1.3% annual average rate, while in 2024, it accelerated to a 2.2% growth rate. Electricity demand grew more rapidly than energy demand itself, increasing by 3.2% in 2024 [1]. These trends reflect the expansion of electricity use in various sectors, from data centers and artificial intelligence applications to the electrification of end-uses and the increasing use of air conditioning, especially in areas affected by heatwaves more frequently than in recent decades [2]. On the other hand, environmental pollution and climate change clearly underscore the need to mitigate human impact on global warming and foster the energy transition from fossil fuel sources to more sustainable solutions in the coming decades. Both conditions result in the necessity to deploy more low-carbon sources, such as nuclear power [3].

Historically, nuclear energy has avoided around 70 billion tonnes of CO_2 emissions [2] and continues to play a crucial role in providing low-carbon electricity [4, 5]. Currently, there are over 400 nuclear reactors in operation and more than 50 under construction [6] in around 30 countries. This renewed commitment to nuclear power expansion reflects a global recognition of nuclear as an essential component to mitigate greenhouse gas emissions and thus meet climate goals [2, 7]. Besides its low-carbon, high-density, and reliability features, as a programmable generation source, nuclear power will be fundamental to support the increasing shares of variable renewable sources, such as solar and wind power [8].

As shown in Figure 1.1, between 2017 and 2024, 52 nuclear reactors began construction. Nuclear market leadership has shifted away from advanced economies towards China and Russia. Table 1.3 presents the reactors under construction.

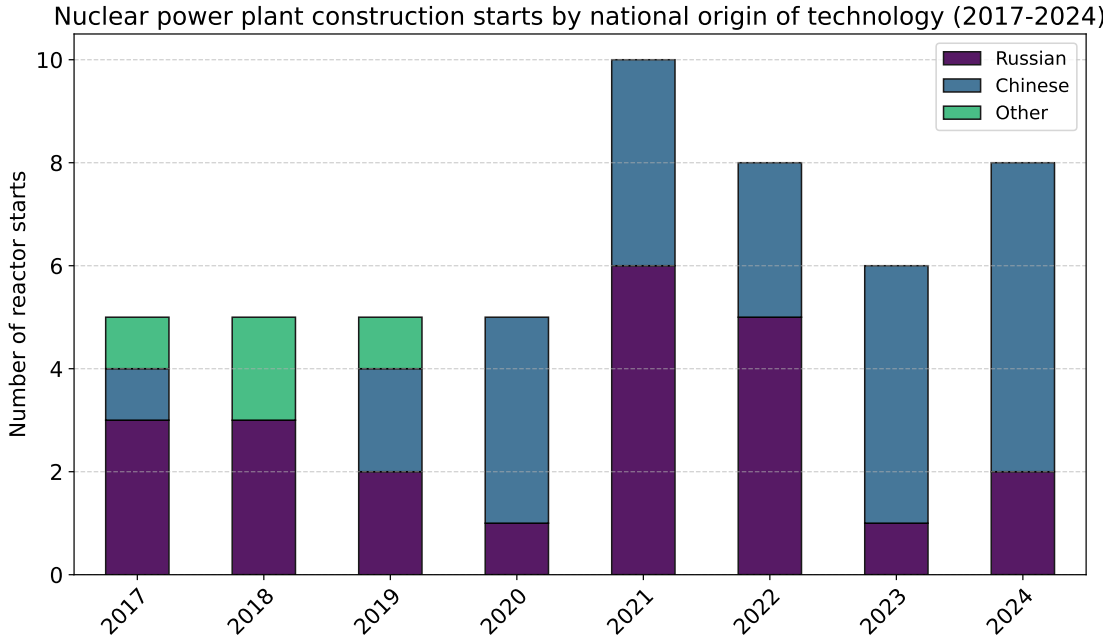

Figure 1.1: Nuclear power plant construction starts by national origin of technology (2017-2024). Data from [9].

The majority of these reactors are of Chinese design, followed by Russian designs. India, Egypt, Turkey, Bangladesh, and Ukraine are using Russian designs, making Russia the leading exporter of nuclear technology, with a total of 23 GW of reactor capacity under construction in six countries (another four reactors with a capacity of 4 GW are being built domestically). On the other side, reactors under construction in Japan, Korea, the United Kingdom, and Brazil are based on domestic designs or those from other advanced economies [9].

As countries seek to meet the growing demand for electricity while also addressing climate objectives, the deployment of Generation III+ reactor designs has become the most common choice [10]. However, when considering 2050 net-zero goals, the advanced designs of the Generation IV reactors are seen as a strategic response to future challenges [11]. These next-generation reactors offer enhanced safety, improved fuel efficiency, and scalability, making them increasingly attractive options. They are well-suited to provide continuous power, manage peak load demands, and support the integration of renewable energy sources. Additionally, they can provide reliable capacity and ancillary services that stabilize the grid when the output from wind and solar sources fluctuates.

Table 1.1: Nuclear Reactors Under Construction by Country (Net Electrical Capacity and Number of Reactors) in 2025 [10]

Country	**Net Electrical Capacity [GWe]**	**Number of Reactors**
China	30.85	29
India	4.77	6
Egypt	4.40	4
Russia	3.85	4
Türkiye	4.46	4
Bangladesh	2.16	2
Japan	2.65	2
Korea, Republic of	2.68	2
Ukraine	2.07	2
United Kingdom	3.26	2
Argentina	0.03	1
Brazil	1.34	1
Iran, Islamic Republic of	0.97	1
Pakistan	1.12	1
Slovakia	0.44	1
Total	**65.04**	**62**

1.2 Generation IV International Forum and Lead-cooled Fast Reactors

The GIF is a collaborative initiative established to outline the path for developing advanced nuclear reactors that offer significant performance advantages over existing systems. This international effort began with the preparation of the Generation IV Technology Roadmap in 2002 [12] by the U.S. Department of Energy (DOE) Nuclear Energy Research Advisory Committee (NERAC) and the GIF itself, which was further updated in 2014 [13]. The Roadmap defined challenging design goals for advanced reactor systems based on four pillars: Sustainability, Economics, Safety and reliability, and Proliferation resistance and physical protection.

Moreover, the Roadmap identified six technologies for reactor systems to achieve these goals and thereby enhance the future role of nuclear energy. These reactor technologies are the Molten Salt Reactor (MSR), the Supercritical Water Reactor (SCWR), the Very High Temperature Reactor (VHTR), the Gas-cooled Fast Reactor (GFR), the Sodium-cooled Fast Reactor (SFR), and the LFR [14].

LFRs are fast-spectrum reactors that use liquid lead or lead-bismuth eutectic (LBE) alloy as coolant. Figure 1.2 presents a schematic representation of an LFR reactor.

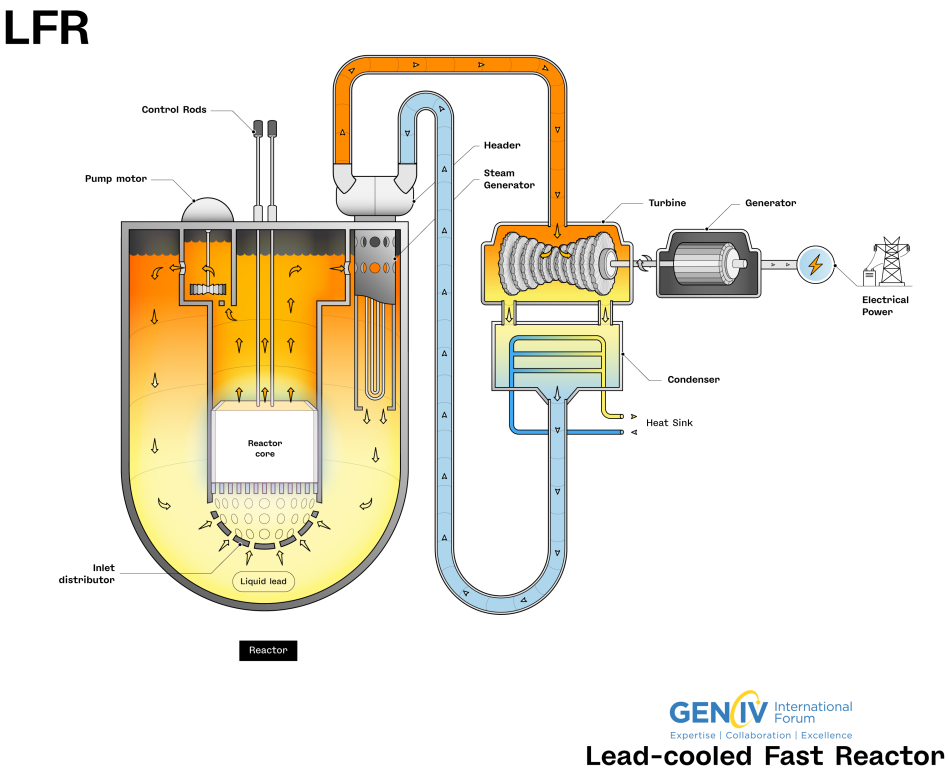

Figure 1.2: Scheme of LFR reactor [13].

The neutronic properties of lead, specifically its low neutron absorption and moderation, are among the crucial advantages that enable LFRs to achieve the ambitious GIF goals [15]. The LFR characteristics that align with the GIF objectives are briefly outlined below.

- **Sustainability**: The low neutron moderation enables LFRs to sustain a hard neutron energy spectrum, providing good neutron economy and performance flexibility. This characteristic is fundamental for the LFR's ability to efficiently breed new fissile material or consume transuranic elements, hence maximizing fuel utilization and reducing waste volume and radioactivity.

- **Economics**: The practical chemical inertness of lead (notably, with water) eliminates the need for an intermediate heat transfer loop and overall allows for design simplifications, while the high boiling point avoids a high-pressure system [16, 17]. LFRs can operate at moderately high temperatures (e.g.,

320–480°C for SUMMER [18], 510°C for Westinghouse DLFR [17], 400-550°C for SEALER-One [19]), leading to high thermodynamic efficiencies (often exceeding 40% [16]). Both the simplified design and high efficiency performance make the technology economically competitive.

- **Safety and Reliability**: The favorable neutronic characteristics of lead allow for larger pin pitches and this design choice offers multiple safety advantages. The larger spacing results in low core pressure loss, significantly improving the natural circulation capability of the coolant in the primary circuit. This strong natural circulation is a cornerstone of LFR passive safety, enabling effective decay heat removal even without off-site or on-site backup power, making the system resilient to loss of flow accidents, even in ultimate (e.g., unprotected) conditions. It also reduces the risk of flow blockage. In addition, the extremely high boiling point of lead (1749°C) reduces the risk of core voiding [16, 18]. Ultimately, the neutronic properties of lead also allow for designing the LFR core with a small reactivity margin, easing the prevention of uncontrolled power increases [17].

- **Proliferation Resistance and Physical Protection**: These features can be enhanced by maintaining a hard neutron spectrum that supports self-sustaining cycles and allows for a longer core life, thereby reducing the frequency of handling operations [16].

In contrast to sodium-cooled fast reactors [20], LFRs do not present the risk of explosion in the event of contact between water/air and the coolant, so it avoids the need for an intermediate heat exchanger between the primary and secondary circuits [16]. Currently, the coolant temperature at the core exit is designed to be between ∼480°C (for bare steels) and ∼530°C (for coated steels) due to material limitations in corrosion resistance, although it is anticipated that in the future it could be in the region between 750-880°C. The expected efficiency of the secondary cycle for the LFR system is at least 42% [21], higher than that of thermal reactors used to date.

Table 1.2 introduces the main characteristics of the three systems selected as reference in the LFR provisional system steering committe of GIF for the Gen IV LFR concepts: the European Lead Fast Reactor (ELFR), a reference commercial reactor with a capacity of 600 MWe [16]; the Russian BREST-OD-300, a 300 MWe system of intermediate size [22]; and the US Small Secure Transportable Autonomous Reactor (SSTAR), a small system of 10-100 MWe size with a very long core life [23].

Table 1.2: Key design parameters of the GIF lead-cooled fast reactor reference systems [24]

Parameters	ELFR	BREST	SSTAR
Core power (MWth)	1500	700	45
Electrical power (MWe)	600	300	20
Primary system type	Pool	Pool	Pool
Core inlet temp. (°C)	400	420	420
Core outlet temp. (°C)	480	535	567
Secondary cycle	Superheated steam	Water steam	Supercritical CO_2
Net efficiency (%)	42	42	44
Turbine inlet pressure (bar)	180	170	200
Feedwater temp. (°C)	335	340	402
Turbine inlet temp. (°C)	450	505	553

The GIF member countries that participate in the memorandum of understanding for collaboration on LFR R&D are Euratom, the United States, China, Japan, South Korea, and Russia. Table 1.3 introduces the LFR projects under development in the GIF countries. A brief summary of the main ongoing design is presented in the following paragraphs, divided by geographical area.

Russia

The most advanced LFR design is the BREST-OD-300, a pilot demonstration prototype for a commercial reactor with a closed fuel cycle. In February 2021, the developed design was licensed by Rosatom [25], and the construction of the power plant started in June 2021. In 2024, the first stage of reactor vessel installation was completed. To fulfill the license conditions, various tests were conducted, including experiments at the BFS test facility. The assembly demonstrated good agreement with the calculated effective multiplication factor and reactivity effects for the BREST reactor. Other experimental data were obtained on the following neutronics key parameters: spatial distributions of flux and reaction rates, worth of control rods, and reactivity effects [21].

Europe

In Europe, activities related to LFR technology are conducted in four countries: Belgium, Italy, Romania, and Sweden. Belgium, which has always been focused on ADS LBE-cooled solutions, selected in 2022 LFR as a key technology to meet national targets, with the national Nuclear Research Centre (SCK CEN) leading research and demonstration activities. Moreover, Belgium is progressing in the pre-licensing of MYRRHA (an LBE-cooled multipurpose facility for irradiation testing and ADS demonstration) with FANC/Bel-V, the Belgian nuclear safety

authorities [26].

Italy has been investing in LFR research since the 2000s, with Italian National Agency for New Technologies, Energy and Sustainable Economic Development (ENEA) and Ansaldo Nucleare playing key roles on the international stage. They are working together on Advanced Lead-cooled Fast Reactor European Demonstrator (ALFRED) in collaboration with the Romanian nuclear research center RATEN-ICN, as part of the FALCON (Fostering ALFRED Construction) International Consortium. ALFRED is a 300 MWth reactor that uses a mixture of uranium and plutonium oxides as fuel, usually known as Mixed Oxide Fuel (MOX), and aims to demonstrate the safety and reliability of LFR technology. Additionally, the company newcleo is engaging since 2021 in several research and development activities in partnership with various EU organizations to develop two models, the LFR-AS-30 (an experimental reactor for irradiation) and the LFR-AS-200 (the commercial system) [21]. At the same time, newcleo is working to establish a large-scale research infrastructure in collaboration with the ENEA Brasimone Research Centre in Italy, as well as to set up a MOX fuel factory in France to support its commercial LFR program. Recently, the Italian government has expressed renewed interest in nuclear technologies [27, 28, 29].

Romania, through RATEN-ICN, has been actively involved in European LFR projects since 2010. It declared its interest in hosting ALFRED in 2011 and subsequently joined the FALCON consortium in 2013. The country has included ALFRED and related research infrastructures in its national strategies and is now financing ATHENA, the largest experimental lead facility in Europe [26].

In Sweden, the company Blykalla is conducting R&D activities for the construction of the Swedish Advanced Lead Reactor (SEALER), a 140 MWth LFR demonstrator designed for commercial power production [19, 21].

Asia

The China Lead-based Reactor (CLEAR), in its 10 MWth version, was selected for the technology development of the Gen IV LFR. The CLEAR-M10 project aims to build a small modular energy supply system. Currently, an electrically heated pool-type LBE-cooled facility is being used to perform experiments on thermal-hydraulic characteristics and prototype components [30]. Other Chinese companies and universities are also involved in LFR R&D. The research domain varies from code development for advanced reactor design to thermal-hydraulics and multiphysics coupled analysis.

In Japan, the Tokyo Institute of Technology continues its research on innovative small, fast reactors that utilize lead or lead-bismuth as a coolant and employ either natural uranium or depleted uranium in the fuel composition. In 2024, the analysis

of this reactor from the start-up core to the equilibrium burnup state through the transient phase was conducted using nitride fuel.

In Korea, the MicroURANUS conceptual design is being advanced towards a standard design edition [31]. This small design for maritime applications has a 20-30 MWe power rating, LBE coolant and a minimum 40-year full-power core life. Assessments of passive safety and the risk of steam explosions have been conducted, along with advancements in the development and testing of new component materials.

North America

In the United States, the Massachusetts Institute of Technology and the University of Pittsburgh are following projects directly related to the corrosion in and irradiation of lead and LBE coolants [32], while a third one is addressing the compatibility and chemical interactions of uranium nitride fuel, alumina-forming austenitic alloys, and lead coolants and sublayers. Moreover, the DOE funded two Technology Commercialization Fund projects, which support the adaptation of the fast reactor analysis software developed at national laboratories to meet industry needs [33, 34, 35, 36].

Table 1.3: LFR Projects Under Development [37]

Project Name	**Country**	**Power Rating**	**EDD**[1]	**Fuel/Notes**
ALFRED	EU	300 MWth	2035–2040	MOX
ELFR	EU	1500 MWth	2040–2050	MOX
G4M	USA	70 MWe	N/A[2]	UN[3]
MYRRHA	Belgium	100 MWth	2036	MOX
PEACER	South Korea	300 MWe	N/A	U-TRU-Zr alloy
SEALER-55	Sweden	55 MWe	End of 2020s	UN
SVBR-100	Russia	100 MWe	Unknown	Uranium oxide, LBE-cooled SMR
LFR-AS-30	Italy/UK/ France	90 MWth	2030	MOX, Irradiation reactor in fast spectrum
LFR-AS-200	Italy/UK/ France	200 MWe	2033	MOX

1.3 ALFRED

Since the ALFRED demonstrator will serve as the reference reactor for the uncertainty quantification of some neutronics key parameters conducted during this study, this section provides a brief description of the core.

The European Commission co-founded the LEADER project as part of the 7 [th] Framework Program, aiming to develop a conceptual design for an LFR demonstrator. ALFRED was designed to represent a fully industrial-sized reactor [38]; however, it has lately been designated as a prototype for an LFR Small Modular Reactor (LFR-SMR) [39]. Following the conclusion of the LEADER project, the ALFRED design had been carried on by the FALCON International Consortium, with ENEA serving as the coordinator of the core design activities. Concerning the ALFRED core, the reference configuration comprises 134 Fuel Assemblies (FAs), 12 Control Rods (CRs), 4 Safety Devices (SDs), and 1 Test Assembly for material qualification, as shown in Figure 1.3, where the 102 Dummy Assemblies (DAs) surrounding the core are also present.

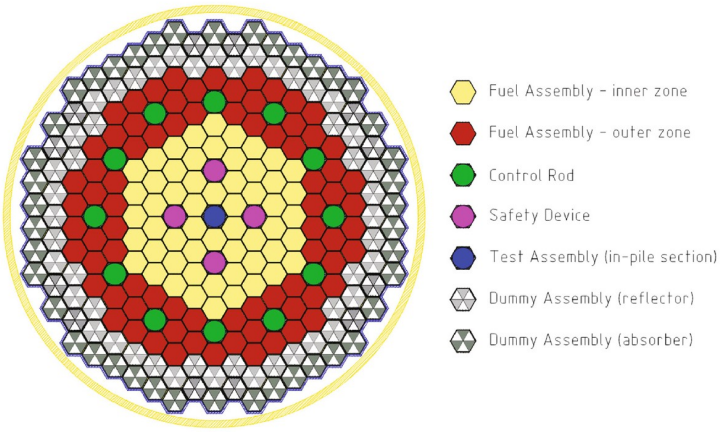

Figure 1.3: Cross-sectional view of ALFRED core map [40].

Regarding the fuel, ALFRED will carry MOX with two different plutonium enrichment zones to flatten the power distribution. Following neutronic analyses, it was decided to have 56 FAs with an enrichment of 20.5 wt.% in $PuO_{1.97}$ in the inner zone and 78 FAs with an enrichment of 26.2 wt.% in the outer zone [40].

[1]EDD = Expected Deployment Date
[1]N/A = Deployment date not available since it is still in the conceptual design phase
[3]UN = Uranium Nitride

1.4 Licensing context for a new reactor design

There is no unified methodology for nuclear regulation and licensing, even within the existing fleet of nuclear power plants (NPPs). The only international standards recognized to help the national safety authorities develop their own regulations are the *SSR-2/1 Rev. 1* (Specific Safety Requirements) [41] and the *SSG-2 Rev.1* (Specific Safety Guide) [42] provided by the International Atomic Energy Agency (IAEA). The first publication outlines criteria that are specifically relevant to the design of NPPs. It also discusses the safety goals, fundamental safety principles, and concepts that serve as the foundation for developing the safety requirements necessary for a nuclear power plant's design. The latter publication aims at providing guidance in the performance of deterministic analyses as required to substantiate the safety claims on a reactor design upon its licensing, taking due account of the current methodologies and experience from deterministic safety analyses for NPPs conducted around the world. Both documents are kept up to date to maintain consistency with the overall safety framework established by the IAEA and with the state of the art, the last update having been brought to reflect the knowledge derived from the Fukushima Daiichi accident.

Regulatory and licensing practices differ from country to country, shaped by each nation's laws and established procedures [43]. Regarding the criticality validation, the U.S. Nuclear Regulatory Commission (NRC) methodology may be used as an example [44]. Here, the criticality safety limits are established through computer-based calculation methods and evaluated to ensure compliance with the safety margin. In the evaluation of safety margins, uncertainties play a crucial role, giving the confidence to the regulatory body to accept (or refuse) a reactor design undertaking the licensing process.

Generally, best estimate codes are used for a wide range of applications, including design, safety evaluations, and licensing. Their use in Light Water Reactors (LWRs) is commonly acknowledged and accepted owing to the comprehensive and well-documented qualification database accompanying them, which forms the basis for an accurate quantification of the uncertainties associated to best estimate results. Unfortunately, innovative designs such as LFRs lack the experimental history to compare simulations with. To prove the reliability of the modeling & simulation tools employed in new reactor design, and assess the requested confidence in their accuracy, experimental facilities sharing common characteristics with the reference reactor can be used within the scope, as it will be described in the following section 3.

The license of innovative designs is mandatory on the road to building the future fleet of NPPs. Since only qualified codes can be used for the license application, this

approval is a fundamental aspect of the process. A typical software qualification procedure can be divided into three steps:

1. Verification
2. Validation
3. Uncertainty Quantification

possibly complemented by a fourth, Domain Transposition, if required.

Verification
Verification is a formal process made along and just downstream coding, to determine whether the equations are solved correctly from both a numerical and a computational point of view. It concerns numerical methods, algorithms, along with their implementation, the data flow diagrams, and the architecture of the IT software [45]. Verification may include comparing with analytical results or results supplied by a reference code. During the verification phase, the accuracy of the input data provided is not relevant.

Validation
Validation consists of establishing that a code can accurately simulate the physical phenomena inside a range, which eventually becomes the validation domain of the code. During this step, the precision of the code is evaluated with a specific set of input data, by comparison with experimental measurements.

Uncertainty Quantification
Uncertainty quantification is the last mandatory step for qualification, and builds on the results of validation to establish the confidence to be credited to the computational results when the code is used inside of the validation domain.

Domain Transposition
If the application and validation domains do not fully overlap, the UQ results must be transposed to the application domain to derive new confidence as required to apply the code to the cases of interest.

Neutronic code object of the study
Regarding the neutronics analysis, one of the most widespread and reliable codes is Monte Carlo N-Particle code (MCNP) [46]. MCNP is a versatile, continuous-energy, generalized-geometry, time-dependent Monte Carlo code designed to track several types of particles across a broad range of energies. Originally developed in 1977, it is the first comprehensive Monte Carlo particle transport code. The global user community has developed a strong confidence in the MCNP code's predictive capabilities, thanks to its performance in verification and validation test suites [47],

access to high-quality nuclear and atomic databases, and extensive application by worldwide users in various scenarios.

MCNP has been used for the neutronic characterization of the ALFRED core, along with the ERANOS deterministic code [38]. Both deterministic and Monte Carlo methods solve the neutron transport equation, but they differ in the approximations they introduce. Deterministic codes usually discretize the energy variable using multigroup format, where cross-sections are condensed in the desired energy-groups using a weighting spectrum. Moreover, deterministic codes usually require the homogenization of material regions, which introduces spatial approximation. On the other hand, Monte Carlo codes are capable of modeling complex geometry without major simplifications, using continuous-energy cross-sections. For this reason, they have acquired the status of reference transport codes [48], and are often selected to verify deterministic ones [48, 45]. MCNP was indeed chosen as the reference Monte Carlo code by ENEA [49], mainly due to its outstanding level of development and validation compared to other Monte Carlo codes. In particular, MCNP has been used to validate less mature Monte Carlo codes such as Serpent [50], or OpenMC for photon transport and criticality applications [51].

The focus of this work is indeed not the validation itself, but the third step in the qualification process: the uncertainty quantification of reactor physics parameters such as the multiplication factor, control rod worth, coolant void worth, and the temperature coefficient calculated with MCNP. Consistently with the purpose of uncertainty quantification, the validation domain here considered is that of lead-cooled fast reactors with neutronic characteristics close to those of ALFRED.

1.5 The role of international benchmark projects

As the fifty years of LWRs operation can attest, experimental data are crucial for validating computer codes, proving that they can accurately simulate the behavior of a nuclear reactor during normal operations (or in an accident scenario). Validating code and nuclear data sets requires high-quality experiments. To achieve this, an international initiative has been launched by OECD/NEA (Organisation for Economic Co-operation and Development/Nuclear Energy Agency) to create a global database of neutronics experiments [52]. This effort aims to provide accurate descriptions of each experiment, which are subject to peer review by international experts before being added to the database. Such standardized experiments are commonly referred to as *benchmarks* [48].

The OECD-NEA acts as a central international body to maintain the historical insights gained from comprehensive experiments, particularly those performed in

decommissioned facilities, as well as insights from experts who have retired. Three main types of experiments lead to the creation of computerized databases: criticality, reactor physics, and shielding.

The first one is the International Criticality Safety Benchmark Evaluation Project (ICSBEP) [53], which collects about 598 evaluations with benchmark specifications for 5159 critical, near-critical, or subcritical configurations. This database focused on criticality appears relevant to reactor physicists. However, other neutron variables need to be assessed to confirm transport codes.

To sustain the current and future reactor physics validation necessities, following the success gained by ICSBEP [52], the International Reactor Physics Evaluation (IRPhE) project was developed [54]. This second project is dedicated to evaluating benchmark experiments covering a wide range of applications, from thermal LWRs and high temperature reactors (HTRs) to fast reactors of various designs. IRPhE handbook [55] includes several nuclear facilities: a total of 166 of the 170 evaluations are published as approved benchmarks. The experiments are dedicated to reactor physics topics, but going beyond criticality, such as reactivity coefficient measurements and local reaction rate distributions. In some cases, the evaluations also include the study of sensitivity to material temperatures, material composition, or material insertion in the reactor, as well as spectrum measuring, kinetics, and power distribution. The goal of the IRPhE Project is indeed to meet neutron physicists' unique needs.

International nuclear regulatory organizations, governmental facilities, universities, as well as industrial and commercial entities, use these databases for validating their codes and data, and to continuously support the neutronics Modeling and Simulation (M&S) of the existing reactor fleet. These benchmark handbooks are recognized as the quality standard for international benchmarking efforts. They are employed worldwide for the development of analytical and computational methods, validation and verification, reactor design and licensing, training, criticality and reactor safety analyses, fuel cycle and associated activities, experiment design, and the refinement of nuclear data by a broad spectrum of actors in the nuclear field.

The quality of benchmark cases benefits from a meticulous evaluation of experimental uncertainties, particularly those related to the measurements of the effective multiplication factor (k_{eff}) [56], the spectral characteristics, reactivity effects and coefficients, kinetics, and other measurements [57]. Integral parameters, such the afore mentioned, occupy a unique and critical role in the validation chain of neutron transport codes. They are measurable in critical or subcritical experiments and, at the same time, computable with simulation tools. Unlike the differential measurements, which refers to individual microscopic cross-sections, integral experiments characterize the combined response of the entire physical system or, in

other words, they reflects the cumulative effect of uncertainties propagation from the underlying input data though the computational methodology. Because integral parameters can be both directly measured and independently simulated, they provide a consistency test of the whole modelling framework. Without using these integral experiments, it would be even more challenging to identify and diminish the uncertainties in nuclear data, which are essential for maintaining accurate and reliable computational analyses.

Current experimental facilities for LFR developments

While uncertainty quantification in the case of existing power plants benefits from an extensive database of operating reactor experimental results, new designs such as LFRs can rely on a smaller number of past integral experiments that can be considered representative enough. On the first place, the representativeness is often derived from qualitative considerations regarding the type of fuel, the geometry of the core and/or size. On the second place, the representativeness parameter can be calculated using, for example, sensitivity coefficients (as it will be introduced later for this work). Building mock-up facilities appears out of reach for most projects due to the high costs involved. In fact, there are very few available facilities currently in operation:

- **VENUS-F** [58], a fast zero-power reactor at the Belgian Nuclear Research Centre SCK-CEN, which in the recent past served as a mock-up of MYRRHA [59];
- **BFS** [60], two fast criticality facilities situated at the Institute of Physics and Power Engineering (IPPE) in Russia, one of which was employed in support of the BREST project.

VENUS-F

The VENUS facility, originally designed and operated to reproduce thermal reactor conditions, was transformed into the VENUS-F configuration (2007-2010), featuring lead blocks and a fast spectrum, to support Accelerator Driven Systems (ADS) like MYRRHA. Since 2011, ten critical VENUS-F configurations have been studied to advance in MYRRHA ADS and LFR core designs, with variations in fuel assembly number and composition, reflector materials, and in-pile section mock-ups [61]. In 2016, lead was replaced with bismuth, and a new experimental campaign was initiated to validate the properties of bismuth in integral experiments, particularly in the neutron energy range from 1 keV to 10 MeV. Since 2017, lead and bismuth have been combined in fuel assemblies to simulate lead-bismuth eutectic [62]. These zero-power experiments served two primary purposes: full-scale (mock-up) and benchmark experiments. Mock-up experiments were focused on various reactor physics parameters, including criticality, absorber rod worth,

spectral indices, fission rate distributions, and safety-related reactivity effects like coolant voiding, which directly support the safety and licensing of MYRRHA and LFRs. The second kind of experiments involves simplified models to improve cross-section data, comparing results with calculations through Calculated-to-Experiment (C/E) analysis. Multiple computational tools were used for pre- and post-test analysis of these experiments: both deterministic (ERANOS) and stochastic codes (MCNP, SERPENT) using various nuclear data libraries (JEFF, JENDL, ENDF/B) [61]. The general aim was to represent new core designs as closely as possible to verify the reliability of computer codes and nuclear data.

BFS
At the BFS complex, various full-scale reactor mock-ups can be simulated. The configurations can use different types of fuel, such as metal, mixed oxide, and nitride, as well as various coolants, including sodium, lead, lead-bismuth, and water. Different materials can also be employed for the control rods. The first criticality experiment was performed in 1961 at the BFS-1 facility. Among the assemblies tested during the 60+ years of operations, the BFS-61, a benchmark model of an LFR with mixed nitride fuel, was the starting configuration from which a series of experiments was conducted to study the BREST reactor. The assemblies built for this purpose were the BFS-77 in 1999, the BFS-64 and the BFS-95 in 2002, all of which were employed as benchmarks to verify and validate the software and cross-section, and to confirm the neutronics analysis of the BREST-OD-300 core [63]. Besides criticality, several quantities were measured, including void reactivity, spectral indices, delayed neutron fraction, fission rate distribution, and control rod worth. The mentioned assemblies were, though, not shared in the IRPhE benchmark database.

As highlighted in this section, integral experiments are crucial for new LFR designs because they are essential for nuclear data validation, licensing, and supporting the design and operation of new reactor cores. Despite advancements in computational tools and nuclear data libraries, zero-power facility experiments remain crucial, especially for those new core designs that feature non-traditional neutron spectra. Therefore, when the availability of experiments is limited, having databases such as ICSBE and IRPhE is paramount for testing and improving the modeling and simulation capabilities.

1.6 Thesis objectives

In the previous sections, it was highlighted that experimental campaigns are needed to evaluate the reliability of computer codes and nuclear data sets used for design

and to improve cross-section data. Uncertainty quantification indeed plays an essential role in assessing the quality of simulation tools to predict the behavior of a physical system. Moreover, it may often be considered a necessary requirement for any innovative reactor system design [64].

The PhD project aims to provide a UQ step to evaluate the accuracy of the MCNP code by comparing simulations with benchmark experimental data from the IRPhE database, thereby supporting the qualification of MCNP for LFR (ALFRED-like) applications. Moreover, a data assimilation tool is developed with the scope of improving the estimated values for ALFRED. This effort proposes to assess the modeling capability provided by MCNP, determining the levels of accuracy that can be achieved through experiments that are representative of ALFRED.

When LFR design is concerned, the accuracy of the computational code needs to be assessed using state-of-the-art and reliable uncertainty quantification techniques. In this thesis, the post-processing tools have been developed using the Python language. As recommended by the French Nuclear Safety Authority (ASN) in their Guide no.28 [45], the post-processing software used to analyze the results of the code that aspires to be qualified should also be considered in the whole qualification approach. Thus, adequate verification of these tools is required. In Sections 2.6.3 and 2.5.5, the verification of the developed algorithms will be presented.

Following the general introduction presented in this chapter, Chapter 2 is dedicated to the methodologies used in this work. Firstly, an introduction about MCNP and its capabilities to perturb the input data is given, followed by a section dedicated to the uncertainties involved in neutronics analysis. Afterwards, the data assimilation method is proposed. Chapter 3 is devoted to the experimental cases selected from IRPhE and used to perform representativeness calculations. Chapter 4 summarizes the obtained results, and finally, Chapter 5 will draw the conclusions and explore future applications/developments.

This work has been conducted in collaboration with the Laboratory for Design and Analysis of Nuclear Systems (NUC-ENER-PRO), part of the Division for Nuclear Energy Systems of the ENEA Nuclear Department, which has a long experience in LFR core design and neutronics analyses. The verification of the implemented algorithms was conducted during the research period abroad at the Department of Energy Engineering — Nuclear section — of the Escuela Técnica Superior de Ingenieros Industriales (ETSII), within the Universidad Politécnica de Madrid (UPM).

Chapter 2

Methodology

Neutronic analysis of nuclear reactors relies on accurate predictions of neutrons' behavior within a reactor environment. Such predictions are typically obtained through numerical simulation codes that solve the Boltzmann transport equation using nuclear data libraries that include the microscopic cross sections of the isotopes composing the material. However, both the calculation methods and the nuclear data themselves are subject to uncertainties, which ultimately influence the reliability of the simulation results. In the context of reactor core design and safety assessment, quantifying and managing these uncertainties is therefore essential.

The objective of this chapter is to present the theoretical and computational framework adopted in this work to assess, and possibly improve, the predictive capabilities of the MCNP code when applied to LFRs neutronic analysis and core design, using ALFRED as a test bed, with all other reactors represented by ALFRED benefitting of the same results. The first sections are dedicated to a general overview of the Boltzmann transport equation and to an introduction to the MCNP Monte Carlo code used to solve it.

Next, the role of nuclear data libraries and their associated covariance information is examined, as these represent the primary source of uncertainty in neutronics calculations. Perturbation theory and sensitivity coefficients calculation methods are then introduced as key quantities to evaluate how variations in nuclear data propagate to reactivity parameters. The capabilities of MCNP for perturbation and sensitivity analysis are also detailed.

The chapter then focuses on the theoretical formulation of Uncertainty Quantification (UQ), distinguishing between different classes of uncertainties and emphasizing those arising from nuclear data. The methodology adopted to propagate

these uncertainties to system-level quantities of interest is discussed and verified.

Finally, the chapter introduces the Data Assimilation (DA) method implemented in this work, which combines experimental benchmark data with prior simulation results to reduce nuclear data uncertainties (as embedded effect) and improve predictions for ALFRED-like reactor configurations. The Generalized Linear Least Square (GLLS) method is presented as the basis of the assimilation approach, together with its verification procedure.

Overall, this chapter provides the methodological foundation for the two main objectives of the thesis: first, the qualification of MCNP for LFR applications through uncertainty quantification based on a selected set of integral experiments, and second, the development of a data assimilation tool to enhance neutronic predictions for the ALFRED reactor concept.

2.1 The Boltzmann transport equation

The behavior of neutrons in a multiplying system is governed by the time-dependent Boltzmann transport equation, which describes the evolution over time t of the balance of neutrons in the six-dimensional phase space defined by spatial position $\mathbf{r}$, energy E, and flight direction $\mathbf{\Omega}$. The neutron field may be characterized by the angular neutron flux

$$\phi(\mathbf{r}, E, \mathbf{\Omega}, t) \quad ,$$

defined as the neutron density n in phase space multiplied by the particle speed $v(E)$:

$$\phi(r, E, \Omega, t) \equiv v(E) n(r, E, \Omega, t) \quad [\mathrm{cm}^{-2}\,\mathrm{MeV}^{-1}\,\mathrm{sr}^{-1}\,\mathrm{s}^{-1}] \quad . \tag{2.1}$$

To derive the governing equation for ϕ, consider an arbitrary volume V bounded by a closed surface S. We focus on particles with energies within dE of E and directions within $d\mathbf{\Omega}$ of $\mathbf{\Omega}$ at time t. The change in the number of such particles inside V is determined by a balance of gains and losses:

a) rate of increase of particles inside V,

b) net streaming of particles out of V across the surface S,

c) removal due to interactions in the volume (absorption or scattering out),

d) addition due to scattering from other energies and directions into $(E, \mathbf{\Omega})$,

e) contributions from external or independent sources in V.

The total number of particles with energies in $\mathrm{d}E$ about E and with directions in $\mathrm{d}\mathbf{\Omega}$ about $\mathbf{\Omega}$ in V is

$$\left[\int_V \mathrm{d}V n(\mathbf{r}, E, \mathbf{\Omega}, t)\right] \mathrm{d}E\, \mathrm{d}\mathbf{\Omega} = \frac{1}{v}\left[\int_V \mathrm{d}V \phi(\mathbf{r}, E, \mathbf{\Omega}, t)\right] \mathrm{d}E\, \mathrm{d}\mathbf{\Omega} \quad . \tag{2.2}$$

Therefore, the rate of change can be expressed as

$$\frac{1}{v}\frac{\partial}{\partial t}\left[\int_V \mathrm{d}V \phi(\mathbf{r}, E, \mathbf{\Omega}, t)\right] \mathrm{d}E\, \mathrm{d}\mathbf{\Omega} = \left[\int_V \mathrm{d}V \frac{1}{v}\frac{\partial \phi(\mathbf{r}, E, \mathbf{\Omega}, t)}{\partial t}\right] \mathrm{d}E\, \mathrm{d}\mathbf{\Omega} \quad . \tag{2.3}$$

The net flow rate out of V across S is written as

$$\left[\int_S \mathrm{d}S \hat{\mathbf{n}} \cdot \mathbf{\Omega} \phi(\mathbf{r}, E, \mathbf{\Omega}, t)\right] \mathrm{d}E\, \mathrm{d}\mathbf{\Omega} \quad . \tag{2.4}$$

Using the Gauss integral theorem, it can be seen as a volume integral

$$\left[\int_V \mathrm{d}V \nabla \cdot \mathbf{\Omega} \phi(\mathbf{r}, E, \mathbf{\Omega}, t)\right] \mathrm{d}E\, \mathrm{d}\mathbf{\Omega} \quad . \tag{2.5}$$

Since $\mathbf{r}$ and $\mathbf{\Omega}$ are independent with respect to ∇, the streaming of particles across the boundary is given by

$$\left[\int_V \mathrm{d}V \mathbf{\Omega} \cdot \nabla \phi(\mathbf{r}, E, \mathbf{\Omega}, t)\right] \mathrm{d}E\ \mathrm{d}\mathbf{\Omega} \quad . \tag{2.6}$$

Particle interactions within the medium remove flux at a rate proportional to the total macroscopic cross section $\Sigma_t(\mathbf{r}, E, t)$, which is obtained by multiplying the microscopic cross-sections by the density of the nuclide:

$$\left[\int_V \mathrm{d}V \Sigma_t(\mathbf{r}, E, t) \phi(\mathbf{r}, E, \mathbf{\Omega}, t)\right] \mathrm{d}E\ \mathrm{d}\mathbf{\Omega} \quad . \tag{2.7}$$

Scattering and other interactions that produce secondary particles contribute by an integral term over all possible incoming energies E' and directions $\mathbf{\Omega}'$:

$$\left[\int_V \mathrm{d}V \int_0^\infty \mathrm{d}E' \int_{4\pi} \mathrm{d}\mathbf{\Omega}'\, \Sigma_s(\mathbf{r}, E' \to E, \mathbf{\Omega}' \to \mathbf{\Omega}, t)\, \phi(\mathbf{r}, E', \mathbf{\Omega}', t)\right] \mathrm{d}E \mathrm{d}\mathbf{\Omega} \quad , \tag{2.8}$$

where Σ_s is the macroscopic scattering cross section, here used as scattering kernel describing both energy and angular redistribution of neutrons at fixed position $\mathbf{r}$.

Finally, primary sources that introduce particles independently of the radiation field are described by $S(\mathbf{r}, E, \mathbf{\Omega}, t)\mathrm{d}E\mathrm{d}\mathbf{\Omega}$. Putting all contributions together, the

balance relations is obtain as

$$\int_V \left[\frac{1}{v(E)} \frac{\partial \phi(\mathbf{r}, E, \mathbf{\Omega}, t)}{\partial t} + \mathbf{\Omega} \cdot \nabla \phi(\mathbf{r}, E, \mathbf{\Omega}, t) + \Sigma_t(\mathbf{r}, E, t) \phi(\mathbf{r}, E, \mathbf{\Omega}, t) \right.$$
$$\left. - \int_0^\infty \mathrm{d}E' \int_{4\pi} \mathrm{d}\mathbf{\Omega}' \, \Sigma_s(\mathbf{r}, E' \to E, \mathbf{\Omega}' \to \mathbf{\Omega}, t) \, \phi(\mathbf{r}, E', \mathbf{\Omega}', t) - S(\mathbf{r}, E, \mathbf{\Omega}, t) \right] \mathrm{d}V = 0 \quad . \tag{2.9}$$

Being the volume arbitrary, thus the integral must be identically zero, and the equation can be written as

$$\frac{1}{v(E)} \frac{\partial \phi(\mathbf{r}, E, \mathbf{\Omega}, t)}{\partial t} + \mathbf{\Omega} \cdot \nabla \phi(\mathbf{r}, E, \mathbf{\Omega}, t) + \Sigma_t(\mathbf{r}, E, t) \phi(\mathbf{r}, E, \mathbf{\Omega}, t) =$$
$$\int_0^\infty \mathrm{d}E' \int_{4\pi} \mathrm{d}\mathbf{\Omega}' \, \Sigma_s(\mathbf{r}, E' \to E, \mathbf{\Omega}' \to \mathbf{\Omega}, t) \, \phi(\mathbf{r}, E', \mathbf{\Omega}', t) + S(\mathbf{r}, E, \mathbf{\Omega}, t) \quad , \tag{2.10}$$

obtaining the time-dependent transport equation, also known as the linearized Boltzmann equation. In situations where the radiation field changes slowly in time, or the medium is stationary, the time derivative can often be neglected, leading to the steady-state form:

$$\mathbf{\Omega} \cdot \nabla \phi(\mathbf{r}, E, \mathbf{\Omega}) + \Sigma_t(\mathbf{r}, E) \phi(\mathbf{r}, E, \mathbf{\Omega}) =$$
$$\int_0^\infty \mathrm{d}E' \int_{4\pi} \mathrm{d}\mathbf{\Omega}' \, \Sigma_s(\mathbf{r}, E' \to E, \mathbf{\Omega}' \to \mathbf{\Omega}) \, \phi(\mathbf{r}, E', \mathbf{\Omega}') + S(\mathbf{r}, E, \mathbf{\Omega}) \quad . \tag{2.11}$$

In multiplying media, neutron-induced fission introduces an additional internal source term. The rate at which fission neutrons are born with energy in $\mathrm{d}E$ and direction in $\mathrm{d}\mathbf{\Omega}$ can be expressed as:

$$\int_0^\infty \mathrm{d}E' \int_{4\pi} \mathrm{d}\mathbf{\Omega}' \, \nu(E') \, \Sigma_f(\mathbf{r}, E', t) \, \chi(E) \, \frac{1}{4\pi} \, \phi(\mathbf{r}, E', \mathbf{\Omega}', t) \quad , \tag{2.12}$$

where $\nu(E')$ is the average number of neutrons emitted per fission and $\chi(E)$ is the fission neutron spectrum. Including fission, the transport equation becomes:

$$\frac{1}{v(E)} \frac{\partial \phi(\mathbf{r}, E, \mathbf{\Omega}, t)}{\partial t} + \mathbf{\Omega} \cdot \nabla \phi(\mathbf{r}, E, \mathbf{\Omega}, t) + \Sigma_t(\mathbf{r}, E, t) \phi(\mathbf{r}, E, \mathbf{\Omega}, t) =$$
$$= \int_0^\infty \mathrm{d}E' \int_{4\pi} \mathrm{d}\mathbf{\Omega}' \, \Sigma_s(\mathbf{r}, E' \to E, \mathbf{\Omega}' \to \mathbf{\Omega}, t) \, \phi(\mathbf{r}, E', \mathbf{\Omega}', t) +$$
$$+ \frac{\chi(E)}{4\pi} \int_0^\infty \mathrm{d}E' \, \nu(E') \Sigma_f(\mathbf{r}, E', t) \phi(\mathbf{r}, E' \mathbf{\Omega}, t) + S(\mathbf{r}, E, \mathbf{\Omega}, t) \quad . \tag{2.13}$$

In quasi-static conditions ($\partial\phi/\partial t \sim 0$) with no external source ($S = 0$), the time-dependent problem can be simplified, reducing it to the steady-state form, so as to leverage a relevant computational simplification for reactor analysis. In such cases, the transport equation is written in k-eigenvalue form:

$$\begin{aligned}\boldsymbol{\Omega}\cdot\nabla\phi(\mathbf{r},E,\boldsymbol{\Omega})+\Sigma_t(\mathbf{r},E)\phi(\mathbf{r},E,\boldsymbol{\Omega}) = \\ \int_0^\infty \mathrm{d}E' \int_{4\pi} \mathrm{d}\boldsymbol{\Omega}'\,\Sigma_s(\mathbf{r},E'\to E,\boldsymbol{\Omega}'\to\boldsymbol{\Omega})\phi(\mathbf{r},E',\boldsymbol{\Omega}')+ \\ \frac{1}{k_{\text{eff}}}\frac{\chi(E)}{4\pi}\int_0^\infty \nu(E')\Sigma_f(\mathbf{r},E')\phi(\mathbf{r},E',\boldsymbol{\Omega})\,\mathrm{d}E' \quad , \quad (2.14)\end{aligned}$$

where k_{eff} is the effective multiplication factor:

$$k_{\text{eff}} < 1 \Rightarrow \text{subcritical}, \quad k_{\text{eff}} = 1 \Rightarrow \text{critical}, \quad k_{\text{eff}} > 1 \Rightarrow \text{supercritical}.$$

2.2 Neutronics Code: MCNP

2.2.1 Monte Carlo methods for neutronics calculations

The integro-differential form of the Boltzmann transport equation (Eqs. 2.10 or 2.14) is exact but cannot be solved analytically for systems of practical interest. Deterministic solution methods approximate the neutron field by discretizing one or more of the variables $(\mathbf{r}, E, \boldsymbol{\Omega}, t)$ into finite meshes or group structures. This introduces systematic numerical errors associated with spatial meshing, angular quadrature, and multigroup energy treatment.

Monte Carlo methods, by contrast, avoid these discretization errors by simulating particle transport directly in continuous space, energy, and angle [65, 66]. A Monte Carlo transport calculation proceeds by random sampling of individual particle histories, beginning from source emission, traveling along straight-line paths between interactions, and undergoing collisions such as scattering, absorption, or fission. Secondary neutrons, which can be produced by fission events, are recorded and subsequently tracked as new histories. The distance to the next interaction, interaction type, scattering angle, and secondary particle production are all sampled according to probability distributions of the neutrons' behavior: in other words, they are derived from evaluated nuclear data libraries. The expected value of any quantity of interest (e.g., cell-averaged flux, reaction rate, escape probability) is then estimated from the accumulated contributions over many histories.

Monte Carlo calculations are therefore capable of accurately treating complex three-dimensional geometries using geometrical primitives, heterogeneous material compositions, and highly realistic physics models without requiring variable discretization for criticality calculations. This makes Monte Carlo solvers particularly well-suited for:

- detailed reactor core models containing control rod and internal structures;
- shielding analyses involving labyrinths, penetrations, and streaming paths;
- benchmark-quality reference solutions for verifying deterministic models.

However, because Monte Carlo solutions are obtained by statistical sampling, the resulting estimates carry a statistical uncertainty. Achieving the desired confidence level may require a large number of simulated particle histories N, especially when the quantity of interest is localized in a small, remote region of phase space with respect to the source. In such cases, Monte Carlo simulations may converge slowly. For this reason, modern codes employ importance sampling and other variance reduction techniques to accelerate convergence while preserving physical fidelity.

2.2.2 The MCNP Monte Carlo Code

MCNP is a widely used general-purpose radiation transport code that leverages the Monte Carlo approach to solve neutron, photon, electron, and coupled transport problems. MCNP supports a broad range of physics, geometries, and source definitions through its input schema, making it a highly flexible and robust tool for research, design, and verification in nuclear science and engineering. MCNP operates through a structured input deck composed of the so-called *cards*: each line or group of continued lines encodes one element of the problem. MCNP cards are divided into three main blocks, which must appear in order: `CELL`, `SURFACE`, and `DATA` cards. A *cell* represents a volume of space with assigned material properties, a *surface* defines the mathematical boundaries used by cells, while *data* ones comprise material definitions, source distributions, type of calculations, particle tracking functions, etc. [46] In the following bullet points, a brief explanation of how MCNP works is presented.

- **Problem setup**: users can define the geometry using combinatorial geometry (cells and surfaces), specify material compositions, assign cross-section data (from ENDF/B and other evaluated nuclear data libraries), and describe sources (position, energy, direction, time) using input cards.

- **Particle Tracking**: MCNP simulates each neutron's lifetime from emission to absorption, escape, or other terminal events. Random numbers are used to sample outcomes at every step, including initial position/energy, flight distances, collision types, secondary particle creation, and the subsequent transport of these particles.
- **Tallies and Results**: during each history, scores of user-specified "tallies" (e.g., flux, reaction rate, dose) are incremented as neutrons interact with designated geometry features. Statistical summaries, including estimates of relative error and precision, are accumulated as the simulation progresses. Special variance reduction techniques, such as splitting, Russian roulette, and importance sampling, can be employed to improve simulation efficiency, for example, in shielding cases.
- **Statistical convergence**: the central limit theorem underpins the Monte Carlo estimation. Repeated histories ensure that the sample means converge toward the true means, and confidence intervals for computed results are calculated using the variance across all histories.

Monte Carlo methods embodied in MCNP offer significant advantages for problems involving complicated geometries, heterogeneous materials, and coupled particle physics with respect to deterministic approximations. Their flexibility and accuracy are balanced by the significant computational resources required. Since statistical uncertainty decreases with the inverse square root of the number of histories, it necessitates large numbers of simulations for high-precision results.

However, nowadays the MCNP code supports high-performance parallel execution via both shared-memory threading (OpenMP) and distributed-memory message-passing (MPI) [46, 67]. In practice, when the code is installed on a server or cluster with many CPU cores, the user can significantly reduce the total run time by distributing the simulation of many neutron histories across multiple processing units, either by running multiple threads on a single node or by executing many MPI ranks across nodes (or a hybrid of both). Because each particle's history is independent, MCNP scales well with increasing core number, making it feasible to perform detailed high-fidelity geometry of full core reactors and perform criticality calculations in hours instead of days when run on multiple-core systems, compared to a simple workstation. All the simulations used in this thesis have been run on the high-performance computing cluster *karakuri* provided by the NUC-ENER-PRO Laboratory from ENEA research center in Bologna. *karakuri* is a 7-node cluster with 64 cores per node.

2.3 Nuclear data library and covariance matrix

2.3.1 Nuclear data libraries

Nuclear data are a fundamental resource for nuclear physics research, supporting both scientific knowledge and technological applications. Reliable nuclear structure and reaction data provide the quantitative basis for simulations and calculations of neutron interactions, fission, activation, and radioactive decay, critical for fields such as reactor engineering, safety analysis, and medical isotope production. Among the internationally recognized evaluated nuclear data libraries, ENDF/B-VIII.0 is adopted in this work because the objective is to assess the performance of the package code-data library, namely MCNP 6.3.0 and ENDF/B-VIII.0 distributed from LANL. In addition, this library was previously used during the design and study of ALFRED. Therefore, ENDF/B-VIII.0 is retained to ensure consistency and enable direct comparisons between codes without introducing discrepancies that can be due to differences in nuclear data.

Nuclear data consist of experimentally measured and theoretically derived quantities describing how particles interact with nuclei, as well as the changes in nuclei due to processes such as fission or radioactive decay. The acquisition and validation of nuclear data follow a structured process: experimental measurements are obtained and interpreted using physical models; evaluators then select, compare, renormalize, and average the available information to create evaluated datasets. These evaluated data are compiled into nuclear data libraries in standardized formats such as ENDF6, which specialized software, such as NJOY [68], can subsequently process for specific applications to generate ACE (A compact ENDF) files [69, 70].

Generally, the evaluation process of a new nuclear data library comprises the validation using benchmark experiments to compare calculated and experimental results. This feedback loop identifies deficiencies and guides future measurements or re-evaluations [71]. It is important to remember that all nuclear data inherently contain uncertainties, both from experimental limitations and model approximations. Evaluations aim to quantify these through covariance matrices, but completeness and consistency may vary.

2.3.2 ENDF/B-VIII.0

The Evaluated Nuclear Data File (ENDF/B) library, maintained by the Cross Section Evaluation Working Group in the US and Canada, is widely used in applica-

tions requiring evaluated neutron data. ENDF/B-VIII.0, released in 2018 [70], represents the eighth major update, reflecting advances since its predecessor ENDF/B-VII.1 [69]. ENDF/B-VIII.0 features can be summarized as follows:

- **Content Expansion**. It comprises neutron data for 556 isotopes with coverage for both ground and metastable states.
- **Data Formats**. Evaluated nuclear reaction data are published in the ENDF-6 format and distributed as part of libraries such as the ENDF/B series. However, these evaluations are not directly usable in most Monte Carlo codes, thus they must first be processed into specific formats (ACE). ACE files are generated at multiple temperatures (see Table 2.1). These ACE libraries are typically used in Monte Carlo codes such as MCNP, GEANT4, and others, and they are distributed through the official Los Alamos National Laboratory website [72].
- **Rigorous Testing**. Each data table has undergone thorough testing, including physical consistency checks and benchmarking against critical and pulsed sphere experiments [73].
- **Improved Accuracy**. Benchmark results demonstrate that ENDF/B-VIII.0 matches experimental measurements more closely than its predecessor for the cases compared in [70].
- **Covariance Data**. ENDF/B-VIII.0 provides covariance matrices for many reactions, supporting uncertainty quantification in applications.

Table 2.1: Temperatures and extensions for ZAIDs in ENDF/B-VII.0 [70]

Temperature [K]	ZAID Extension
293.6	.00c
600	.01c
900	.02c
1200	.03c
2500	.04c
0.1	.05c
250	.06c

2.3.3 Covariance Matrix

There are two types of uncertainties associated with nuclear data evaluation: statistical and systematic. Statistical uncertainties arise from random errors in counting rate measurements, whereas systematic uncertainties stem from consistent biases affecting the experimental setup. Typical sources of systematic uncertainty in microscopic measurements can introduce a common offset across multiple data points. Systematic uncertainties include: the composition of the sample, detector dead-time corrections, background signal estimation, uncertainties in the neutron flux standard, normalization procedures in transmission experiments, and effects related to the energy resolution [71].

Systematic uncertainties are accounted for through the correlations between measurements obtained with the same experiment. These measurements, along with their associated covariance matrices, form the basis for nuclear data evaluations. Since the same models, approximations, and experimental data are often used to adjust model parameters over an entire energy range, correlations naturally arise between cross sections corresponding to different energy intervals.

To incorporate these effects, nuclear data covariance matrices are computed, capturing both the magnitude of the uncertainties and the correlations they introduce between data points. These covariance matrices are typically generated on a predefined energy grid — consistent with that used in neutronic simulations — to enable accurate uncertainty propagation analyses [73].

The covariance matrix used later on in this work to propagate nuclear data uncertainty for the ENDF/B-VIII.0 library has been provided by ENEA NUC-ENER-PRO Laboratory. It comprises the nuclear data uncertainties of:

- 78 isotopes;
- six reaction data, namely
  - elastic scattering cross section,
  - inelastic scattering cross section,
  - (n,xn) or (n,2n) cross section (mechanisms for the release of n-1 or 1 free neutrons),
  - fission cross section,
  - radiative capture, or simply "capture", cross section,
  - $\bar{\nu}$, average total (prompt plus delayed) number of neutrons released per fission;

- 33 energy groups (generally suitable for fast-spectrum reactor applications).

The data file provided by ENEA has the form of a correlation matrix: it contains standard deviation instead of variances, and correlation instead of covariances. Considering the following mathematical relationship:

$$var(\alpha_i) = \sigma_i^2 \tag{2.15}$$

$$corr(\alpha_i, \alpha_j) = \frac{cov(\alpha_i, \alpha_j)}{\sqrt{var(\alpha_i) \cdot var(\alpha_j)}} \quad , \tag{2.16}$$

$$\tag{2.17}$$

where σ_i indicates the standard deviation of the i^{th} parameter α (that in this case indicates a cross-section). The correlation matrix can thus be converted into the covariance matrix through a Python script implementing this formula

$$cov(\alpha_i, \alpha_j) = corr(\alpha_i, \alpha_j)\sqrt{var(\alpha_i) \cdot var(\alpha_j)} \tag{2.18}$$

for each isotope/reaction pair to generate the corresponding covariance matrix. In addition, it combines the singular matrices into the final one, including all isotopes and reactions of interest among the available ones.

2.4 Perturbation Theory (Sensitivity Coefficients)

Sensitivity coefficients are defined as quantities that express the relative change in a system response due to a small change in an input parameter. For systems containing fissile materials, an appropriate response variable is the effective neutron multiplication factor, k_{eff} . For the scope of this work, nuclear data are considered as the input parameters of interest.

The sensitivity coefficients are commonly represented as functions of the neutron energy, illustrating the dependence of k_{eff} on perturbations in the nuclear data. Such sensitivity profiles can be generated for each material within the system and may include a variety of nuclear reactions (e.g., scattering, absorption, fission, $\bar{\nu}$), as well as other nuclear parameters such as the fission neutron spectrum χ.

Sensitivity coefficients serve various purposes:

1. they enable the characterization of the system's physical behavior by quantifying the response variations due to changes in the parameters;

2. they facilitate the identification of the most influential processes (e.g., the most relevant effective cross-sections) and the assessment of their relative importance.

3. they allow propagation of the uncertainties of the input parameters to the response of interest.

There are two ways to express the sensitivity coefficients.

- **Absolute sensitivity coefficient.** The absolute sensitivity coefficient of the k_{eff} to an energy group of a given effective cross section (corresponding to a particular nuclide-reaction pair), is defined as the variation of the k_{eff} with respect to that effective cross section:

$$S_{k,\sigma} = \frac{\mathrm{d}k_{\text{eff}}}{\mathrm{d}\sigma} \quad . \tag{2.19}$$

- **Relative sensitivity coefficient**. It represents the relative change of the k_{eff} to a relative change in an effective cross section:

$$S_{k,\sigma} = \frac{\mathrm{d}k_{\text{eff}}/k_{\text{eff}}}{\mathrm{d}\sigma/\sigma} \quad . \tag{2.20}$$

Besides the sensitivity profiles, the integrated sensitivity coefficient (ISC) is another quantity often used in the sensitivity analysis. It defines the sensitivity coefficient integrated over the entire energy range:

$$ISC = \int_{E_i}^{E_f} S_{k,\sigma}\mathrm{d}E \quad . \tag{2.21}$$

This value quantifies the sum of the values of the sensitivity profile over all energy groups. This coefficient has the advantage of condensing the information of the sensitivity profile in a single value, but it is not very representative in the case of sensitivity profiles where negative and positive contributions compensate each other. For example, the compensation of positive and negative terms is significant in the case of the fission spectra of ^{239}Pu (χ reaction, MT = 1018), as noticed in [74].

2.4.1 Methods of calculating sensitivity coefficients in MCNP

MCNP 6.3.0 provides two types of perturbation theory: one utilizes the differential operator through the `PERT` card, while the other two employ adjoint weighting via

the KPERT and KSEN cards [46]. Each method comes with its own set of advantages and disadvantages. The differential operator technique relies on a Taylor series expansion, making it particularly effective for generalized responses in fixed-source problems [75]. However, in eigenvalue problems, the differential operator approach may yield inaccurate results because MCNP 6.3.0 implementation does not account for the perturbation of the fission source distribution.

Differential Operator Technique

The Differential Operator technique is based on the premise that the parameter α has an exponential form such as $\exp(\theta)$ where θ is a dimensionless parameter. The change in the response due to a perturbation in θ can be expressed as a Taylor series expansion around the nominal value of θ:

$$R(\alpha) = R(\exp\theta^0) + \left(\frac{\partial R}{\partial \theta}\right)_{\alpha^0} + \frac{1}{2}\left(\frac{\partial^2 R}{\partial \theta^2}\right)_{\alpha^0} (\delta\theta)^2 + ... \tag{2.22}$$

Normally, this expression is truncated with one or two terms (theory of first- or second-order perturbations), and there are no cross-terms between derivatives, which can have an impact on the accuracy of the results in some problems. In the case of the Monte Carlo code MCNP, the PERT card is used, giving a response in the following form:

$$R(\alpha) - R(\alpha^0) = (\Delta R)_{PERT\,1^{st}} + (\Delta R)_{PERT\,2^{nd}} \quad . \tag{2.23}$$

For an answer based on the neutron path, to calculate the derivatives that appear in the equation, it would be necessary to estimate three terms. The first would be the change in response when disturbing the parameter; the second would be the change in the probability of that random trajectory occurring; the third would be the change in the fission source due to the effect of the disturbance.

To determine the sensitivity to a given parameter, the magnitude of the perturbation is chosen. Even if the perturbed problem is not solved, the sensitivity coefficients can be obtained from estimators of the change in the particle's path for a sample of particle histories. Example for neutron flux ϕ:

$$[\Delta\phi(\Delta\sigma_x)]_{PERT} = [\Delta\phi(\Delta\sigma_x)]_{PERT\,1^{st}} + [\Delta\phi(\Delta\sigma_x)]_{PERT\,2^{nd}} \tag{2.24}$$

$$[\Delta\phi(\Delta\sigma_x)]_{PERT\,1^{st}} = \left.\frac{\mathrm{d}\phi}{\mathrm{d}\sigma_x}\right|_{\sigma_x,0} \Delta\sigma_x \tag{2.25}$$

$$[\Delta\phi(\Delta\sigma_x)]_{PERT\,2^{nd}} = \frac{1}{2}\left.\frac{\mathrm{d}^2\phi}{\mathrm{d}\sigma_x^2}\right|_{\sigma_x,0} (\Delta\sigma_x)^2 \quad . \tag{2.26}$$

The sensitivity with respect to an effective cross section would be:

$$S_{k,\sigma_x} = \frac{1}{\phi_0 p_x}[\Delta k(\Delta\sigma_x)]_{1^\circ} \quad where \quad p_x \equiv \frac{\Delta\sigma_x}{\sigma_x} \quad . \tag{2.27}$$

Adjoint-weighting method

Following the derivation presented in [76], the steady-state Boltzmann transport equation can be written as

$$[A - \lambda B]\phi = 0, \tag{2.28}$$

where A and B are the neutron loss and production operators, ϕ is the angular neutron flux, and λ is the eigenvalue whose dominant value corresponds to $1/k_{\text{eff}}$.

Perturbations to the operators and eigenvalue are defined as

$$\begin{aligned} A' &= A + \delta A, \\ B' &= B + \delta B, \\ \lambda' &= \lambda + \delta\lambda \quad , \end{aligned} \tag{2.29}$$

where δA and δB denote small linear perturbations, and $\delta\lambda$ is the associated change in the eigenvalue. The perturbed transport equation is thus expressed as

$$[A' - \lambda' B']\phi' = 0 \quad . \tag{2.30}$$

The adjoint of Eq. (2.28) is given by

$$[A^* - \lambda B^*]\phi^* = 0 \quad , \tag{2.31}$$

where ϕ^* represents the adjoint flux (also known as the importance function), and A^*, B^* are the corresponding adjoint operators.

Multiplying Eq. (2.30) by ϕ^* and integrating over the entire phase space yields

$$\langle \phi^*, (A' - \lambda' B')\phi' \rangle = 0 \quad , \tag{2.32}$$

where $\langle \cdot \rangle$ denotes integration over all spatial, angular, and energy variables.

Substituting Eq. (2.29) into Eq. (2.32) gives

$$\langle \phi^*, (A - \lambda B + \delta A - \lambda\delta B - B\,\delta\lambda - \delta\lambda\,\delta B)\phi' \rangle = 0 \quad . \tag{2.33}$$

By invoking the adjoint property,

$$\langle \phi^*, (A - \lambda B)\phi' \rangle = \langle \phi', (A^* - \lambda B^*)\phi^* \rangle \quad , \tag{2.34}$$

and substituting Eq. (2.31), the expression simplifies to

$$\langle \phi^*, (\delta A - \lambda \delta B - B\,\delta\lambda - \delta\lambda\,\delta B)\phi' \rangle = 0 \quad . \tag{2.35}$$

Neglecting the second-order term ($\delta\lambda\,\delta B$) and assuming $\phi' \approx \phi$ (i.e., perturbations do not significantly modify the flux distribution), the eigenvalue perturbation becomes

$$\frac{\delta\lambda}{\lambda} = \frac{\langle \phi^*, (\delta A - \lambda \delta B)\phi \rangle}{\langle \phi^*, \lambda B \phi \rangle} \quad . \tag{2.36}$$

Replacing the perturbations δA and δB with their partial derivatives with respect to a macroscopic cross section Σ_x, the relative sensitivity of λ is written as

$$\frac{\Sigma_x}{\lambda}\frac{\partial\lambda}{\partial\Sigma_x} = \frac{\Sigma_x}{\lambda}\frac{\langle \phi^*, \left(\frac{\partial A}{\partial\Sigma_x} - \lambda\frac{\partial B}{\partial\Sigma_x}\right)\phi \rangle}{\langle \phi^*, B\phi \rangle} \quad . \tag{2.37}$$

Since $\lambda = 1/k_{\text{eff}}$, it follows that $\frac{\partial\lambda}{\lambda} = -\frac{\partial k_{\text{eff}}}{k_{\text{eff}}}$, and thus the sensitivity of k_{eff} to Σ_x is

$$S_{k,\Sigma_x} = \frac{\Sigma_x}{k_{\text{eff}}}\frac{\partial k_{\text{eff}}}{\partial\Sigma_x} = -\frac{\Sigma_x}{\lambda}\frac{\partial\lambda}{\partial\Sigma_x} = -\frac{\Sigma_x}{k_{\text{eff}}}\frac{\langle \phi^*, \left(\frac{\partial A}{\partial\Sigma_x} - \frac{1}{k_{\text{eff}}}\frac{\partial B}{\partial\Sigma_x}\right)\phi \rangle}{\langle \phi^*, B k_{\text{eff}}^{-2}\phi \rangle} \quad . \tag{2.38}$$

In practice, the terms $\frac{\partial A}{\partial\Sigma_x}$ and $\frac{\partial B}{\partial\Sigma_x}$ are simple functions of the scattering, capture, and fission cross sections. Hence, evaluating Eq. (2.38) involves integrating the direct and adjoint fluxes together with the relevant cross sections over the complete phase space.

When the energy dependence of Σ_x is represented using energy groups, the macroscopic quantity is expressed as $\Sigma_{x,g}$. The groupwise sensitivity of k_{eff} is then

$$S_{k,\Sigma_x,g} = \frac{\Sigma_{x,g}}{k_{\text{eff}}}\frac{\partial k_{\text{eff}}}{\partial\Sigma_{x,g}} \quad . \tag{2.39}$$

By varying g over all energy intervals, one obtains the complete energy-dependent sensitivity profile. Thus, it is possible to determine the perturbation in the response due to a perturbation in a parameter and, therefore, the sensitivity coefficient without the need to solve the perturbed problem (as would be done in the Direct Perturbation method). The equations that need to be solved are the direct equation for the nominal case and the adjoint equation for the nominal equations.

As suggested in the MCNP manual, to analyze the effects of the nuclear data uncertainties on k_{eff} parameters, the sensitivity profiles should be calculated using the `KSEN` card. Using the `KPERT` card is not a suitable option. Even if it is based

on the adjoint-weighted perturbation approach and can ideally accommodate a wider range of perturbations, it introduces an approximation in the treatment of scattering laws, which may cause significant or even unacceptable variations in the scattering sensitivities. Furthermore, the user interface was designed specifically for material substitution, which may make sensitivity coefficient calculations challenging for some users.

2.4.2 KSEN

When users are looking for estimates of changes in reactivity for reactor physics applications or sensitivity coefficients related to the k-eigenvalue, the adjoint-based methodology implemented in the `KSEN` card is the adequate choice. However, they need to be aware of a significant limitation in the adjoint-based methods as implemented in MCNP 6.3.0: these methods do not account for perturbations that may arise from scattering laws or fission emission spectra. For scenarios where the dominant effects are due to absorption or where scattering is mostly isotropic, the results tend to be consistent with those obtained through direct cross-section substitutions and from the adjoint-methodology package TSUNAMI-3D [77] of the SCALE code [78] which employs multigroup cross-section data rather than continuous-energy data.

`KSEN` card and `KSENTAL` options
Here, a brief description of the card characteristics is presented. Sensitivity can be computed if the `KSEN` card is added to a `KCODE` calculation. Multiple cards are permitted in a single input file [79].

After the card name, some values need to be specified for our scope:

- `XS` is the type of sensitivity (the only available at this time);
- `iso`: list of ZAIDs for which sensitivities are desired. The default is all data tables present in the problem;
- `mt`: list of reaction MT numbers or special reaction numbers. Table 2.2 provides a list of acceptable entries from the MCNP user manual [46];
- `erg`: list of energy bin boundaries, in ascending order, over which to provide the sensitivities. In the example (see Listing 2.1), there are 33 energy groups, which is a typical discretization for fast reactors, as well as the same energy ranges of the covariance matrix previously introduced.

Listing 2.1 reports an example of two KSEN cards. Since MCNP version 6.3.0, sensitivity profiles can also be printed directly in *.sdf* format [78] adding at the KOPTS card the option KSENTAL = TSUNAMI-B. Previous versions of the MCNP code, such as MCNP 6.2, could only choose KSENTAL = MCTAL (mctal is a structured ASCII text file that contains detailed tally data output from an MCNP simulation). Appendix A presents different sensitivity output formats that can be obtained with the described input settings. During this study, a Python-based post-processing tool was developed to accurately reproduce the *.sdf* format. Even if the KSENTAL = TSUNAMI-B was already available, developing an in-house script has a twofold advantage: first, it can be used to print *.sdf* format when a combined sensitivity vector is created (as will be introduced in the next section); second, MCNP simulations are lighter/faster since there is no need for the code to create a further output dedicated to the sensitivity coefficients.

Listing 2.1: Example of a KSEN card

```
kcode  1e5  1  100 250
ksrc   0 0 0
c
ksen1  xs iso= 92235.00c  92238.00c
               94239.00c  94240.00c  94241.00c  94242.00c
       mt= 2 4 16 18 102 452 -1018
       erg= 1.100000E-10 1.000000E-07 5.400000E-07 4.000000E-06 8.315287E-06
            1.370959E-05 2.260329E-05 4.016900E-05 6.790405E-05 9.166088E-05
            1.486254E-04 3.043248E-04 4.539993E-04 7.485183E-04 1.234098E-03
            2.034684E-03 3.354626E-03 5.530844E-03 9.118820E-03 1.503439E-02
            2.478752E-02 4.086771E-02 6.737947E-02 1.110900E-01 1.831564E-01
            3.019738E-01 4.978707E-01 8.208500E-01 1.353353E+00 2.231302E+00
            3.678794E+00 6.065307E+00 1.000000E+01 1.964033E+01
c
ksen2  xs iso= 5010.00c   6012.00c  8016.00c
               11023.00c  13027.00c
               14028.00c  14029.00c  14030.00c
               24050.00c  24052.00c  24053.00c  25055.00c
               26056.00c  28058.00c  28060.00c
               42092.00c  42094.00c  42095.00c  42096.00c  42097.00c
               42098.00c  42100.00c
       mt= 2 4 16 102
       erg= 1.100000E-10 1.000000E-07 5.400000E-07 4.000000E-06 8.315287E-06
            1.370959E-05 2.260329E-05 4.016900E-05 6.790405E-05 9.166088E-05
            1.486254E-04 3.043248E-04 4.539993E-04 7.485183E-04 1.234098E-03
            2.034684E-03 3.354626E-03 5.530844E-03 9.118820E-03 1.503439E-02
            2.478752E-02 4.086771E-02 6.737947E-02 1.110900E-01 1.831564E-01
            3.019738E-01 4.978707E-01 8.208500E-01 1.353353E+00 2.231302E+00
            3.678794E+00 6.065307E+00 1.000000E+01 1.964033E+01
```

Table 2.2: Allowed reaction numbers for `KSEN` with continuous-energy physics [46].

Nuclear Data	MT Number	Special Reaction Number
Total	1	—
Total and $S(\alpha, \beta)$	—	−1
Capture	—	−2
Elastic	2	—
Total Inelastic	4	—
Elastic and $S(\alpha, \beta)$	—	−3
Total Fission	18	−6
First-Chance Fission	19	—
Second-Chance Fission	20	—
Third-Chance Fission	21	—
Fourth-Chance Fission	38	—
Total Fission ν	452	−7
Prompt Fission ν	456	—
Delayed Fission ν	455	—
(n,2nd)	11	—
(n,2n)	16	—
(n,3n)	17	—
(n,nα)	22	—
(n,n3α)	23	—
(n,2α)	24	—
(n,np)	28	—
(n,n2α)	29	—
(n,2nα)	30	—
(n,nd)	32	—
(n,nt)	33	—
(n,n^{3}He)	34	—
(n,nd2α)	35	—
(n,nt2α)	36	—
(n,4n)	37	—
(n,2np)	41	—
(n,3np)	42	—
(n,2p)	44	—
(n,npα)	45	—
(n,γ)	102	—
(n,p)	103	—
(n,d)	104	—
(n,t)	105	—
(n,^{3}He)	106	—
(n,α)	107	—
Inelastic Levels (1–40)	51, 52, . . . , 90	—
Inelastic Continuum	91	—
Total Fission χ	—	−1018
Prompt Fission χ	—	−1456
Delayed Fission χ	—	−1455
Total Scatter Law	—	−1001
Elastic Scatter Law	—	−1002
Inelastic Scatter Law	—	−1004

2.4.3 Sensitivity coefficient for reactivity effects

To calculate the worth of the coolant void and/or the control rod, two simulations must be conducted. The first simulation should represent the nominal case for the conditions we wish to observe. The second simulation will involve a perturbed state. The difference in the k_{eff} values obtained from these simulations will provide the magnitude of the effect resulting from moving the control rods or creating voids in regions/volumes within the core. The sensitivity coefficients related to the multiplication factor of the nominal case and the perturbed case are $S_{\sigma,1}$ and $S_{\sigma,2}$, respectively. The relative sensitivity coefficients of a reactivity response are calculated following the derivation in [80]:

$$S_{\rho_{1\to2},\sigma} = \frac{\sigma}{|\rho_{1\to2}|}\frac{\partial\rho_{1\to2}}{\partial\sigma} = \frac{\sigma}{|\rho_{1\to2}|}\left(\frac{\partial\lambda_1}{\partial\sigma} - \frac{\partial\lambda_2}{\partial\sigma}\right) = \frac{\lambda_1 S_{\sigma,1} - \lambda_2 S_{\sigma,2}}{|\rho_{1\to2}|} \quad , \tag{2.40}$$

where $\rho_{1\to2}$ is the change in reactivity between the $S_{\sigma,1}$ and $S_{\sigma,2}$ configurations and $\lambda = \frac{1}{k_{\text{eff}}}$.

Verification

The formula in Eq. (2.40) has been implemented in a stand-alone Python script and subsequently verified against TSAR (Tool for Sensitivity Analysis of Reactivity Responses) [81], which also employs the same methodology. TSAR is a SCALE functional module that computes nuclear data sensitivity coefficients for eigenvalue-difference responses such as reactor reactivity and worth coefficients [78]. TSAR reads previously computed sensitivity coefficients for the k-eigenvalues at two states of a reactor system (or for two different systems) and combines them to obtain sensitivity coefficients for the difference. The reactivity sensitivity coefficients are then combined with nuclear data covariance information to determine the uncertainty in the reactivity response.

For the verification process, a sodium void coefficient case that will be included in the study has been chosen, namely the reference case ZPPR2-12 Loading 26 and the perturbed case ZPPR2-12 Loading 37. The sensitivity profiles of ^{239}Pu fission cross section are represented in Figure 2.1, using the Sensitivity Viewer visualization tool. Sensitivity Viewer is a Java-based software that can read sensitivity files and plot sensitivity profiles [82]. It is a free, standalone application maintained by OECD-NEA. Currently, the supported formats are TSUNAMI (A and B), SUSD3D, MCNP output, ABBN.

The combined coefficients for the reactivity effect were computed both with the in-house Python script and with TSAR, which resulted in perfect agreement of

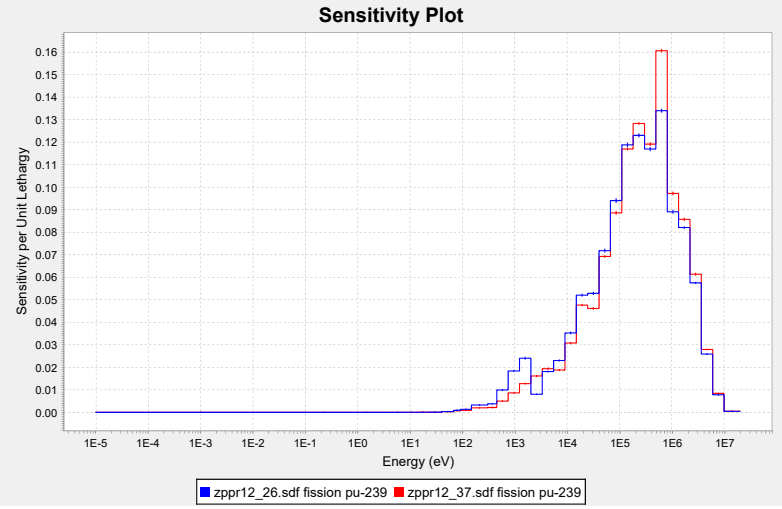

Figure 2.1: Comparison among sensitivity coefficients of the reference case ZPPR2-12 (loading 26) and of the perturbed case ZPPR2-12 (loading 37).

the coefficients. The L2 norm can be used as a synthetic indicator to prove the consistency between the two codes. Indeed, the value obtained was 7.5E-6. An example is given in Figure 2.2, which presents the combined sensitivities of ^{239}Pu fission cross section from TSAR and the Python script. It can be noticed that the coefficients perfectly overlap. The red error bar is the one relative to the TSAR output. The Python script does not currently account for the statistical uncertainty in the sensitivities, so there is no blue error bar present. The coefficients are also reported in Table 2.3 to highlight the excellent agreement. The negligible inconsistencies may be due to rounding present in the algorithms.

The standalone scripts can print the sensitivity coefficients both as a *.npy* file, which is a Python format that can be loaded in other scripts, and/or as *.sdf* file, so it can be used for comparison with other sensitivities, and it is readable in tools such as the Sensitivity Viewer.

Table 2.3: Combined sensitivity coefficients for ^{239}Pu fission cross section: comparison between TSAR and the script developed.

Algorithm	TSAR
2.09599E-03	2.09598E-03
2.29020E-02	2.29019E-02
8.01831E-02	8.01827E-02
1.87591E-01	1.87590E-01
1.44697E-01	1.44696E-01
2.95174E-01	2.95173E-01
7.40758E-01	7.40755E-01
6.24984E-02	6.24974E-02
1.89127E-01	1.89126E-01
-6.23766E-02	-6.23772E-02
-1.05182E-01	-1.05183E-01
-2.10743E-02	-2.10746E-02
-1.35784E-01	-1.35784E-01
-1.20615E-01	-1.20615E-01
-1.26655E-01	-1.26655E-01
-8.98982E-02	-8.98982E-02
4.29810E-02	4.29808E-02
2.38860E-01	2.38860E-01
-2.91125E-01	-2.91124E-01
-2.59198E-01	-2.59198E-01
-1.46222E-01	-1.46222E-01
-4.53189E-02	-4.53188E-02
-5.78075E-02	-5.78074E-02
-1.08020E-02	-1.08019E-02
-2.58999E-03	-2.58999E-03
-1.56843E-03	-1.56843E-03
3.34694E-04	3.34693E-04
7.95249E-05	7.95244E-05
-6.93956E-05	-6.93955E-05
1.06946E-04	1.06946E-04
-8.21032E-05	-8.21030E-05
-3.78731E-05	-3.78730E-05
0.00000E+00	0.00000E+00

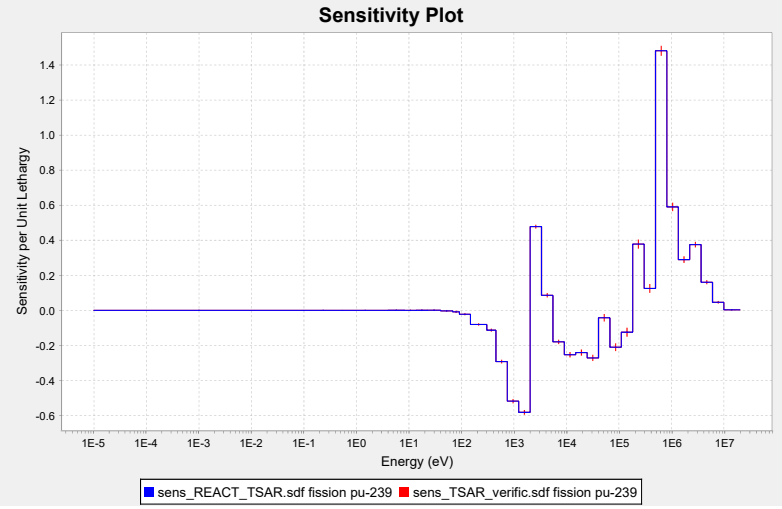

Figure 2.2: Sensitivity coefficient for reactivity effect: verification against TSAR package.

2.5 Uncertainty Quantification Theory

Transport calculations of system responses, such as the neutron multiplication factor, inherently involve biases and uncertainties. These arise from several contributing factors that can generally be classified into three main categories:

a) numerical;

b) modeling and experimental;

c) input data.

2.5.1 Numerical uncertainties

Often referred to as method uncertainties, they originate from limitations inherent in the computational solvers used for transport calculations.

In Monte Carlo methods, such uncertainties may arise from imperfections in random number generation, approximations in techniques used to estimate neutron

multiplication (e.g., incomplete convergence of the fission source distribution or neglected correlations between neutron generations), and biases introduced by algorithms that represent nuclear data or sample probability distributions. Additionally, the intrinsic statistical uncertainty associated with the stochastic nature of Monte Carlo simulations contributes to this class.

Computational benchmark studies are often employed to assess the upper bounds of these effects, determining whether they can be considered negligible or require the application of conservative biases in practical calculations. Typically, numerical uncertainties are assumed to be reduced to an acceptable level by increasing the number of particle histories or at least quantified and bounded by appropriate margins.

2.5.2 Modeling and experimental uncertainties

Modeling uncertainties are those related to the evaluation of an experiment to be used as a benchmark. Here, the evaluator may simplify the representation of the experiment in the benchmark model to make the configuration easier to model (e.g., homogenization of system components). In the ICSBEP Uncertainty Guide [56], an example of this modeling uncertainty is provided. In some cases, the evaluator may use a single temperature that is representative of all the experiments conducted at the same facility, even though the real temperature slightly differs between individual measurements. This assumption implies a constant moderator density in the computational model, whereas the physical system experiences small density variations. The impact of this simplification can be assessed by evaluating the sensitivity of k_{eff} to temperature changes. If the reactivity response is negligible, the mismatch between modeled and measured temperatures can be incorporated into the overall uncertainty related to the temperature, together with the measurement error. On the other hand, when the temperature effect is noticeable but still moderate, a reactivity correction is applied to account for the model-experiment temperature offset, and an additional uncertainty component is assigned to the correction.

Even in highly controlled critical benchmark experiments, uncertainties persist in parameters such as fuel enrichment, impurity levels, material densities or composition, and geometrical tolerances. Such variations lead to discrepancies between the measured and computed values. These effects are collectively referred to as experimental uncertainties, as they remain even when the computational model includes no simplifications.

Although the criticality of a benchmark system may be well established, signif-

icant uncertainty can exist in the measured system parameters that define the configuration. This contribution to the response uncertainty may be interpreted as either experimental, since it originates from experimental characterization, or computational, because it influences the model used in calculations.

The combined effects of both described uncertainties define the overall experimental uncertainty associated with the value of interest. Descriptions of benchmark experiments in the ICSBEP commonly provide quantitative estimates of such parameter uncertainties and their corresponding impact on the neutron multiplication factor. These standard deviations in k_{eff} are typically assigned by evaluators based on experimental documentation, archived data, and other relevant sources [56, 57].

2.5.3 Input (nuclear data) uncertainties

For many applications, the predominant contributor to response uncertainty is the nuclear data component. These involve uncertainties in evaluated quantities such as microscopic cross sections, fission spectra, neutron yields ($\bar{\nu}$), and scattering distributions, as compiled in libraries like ENDF/B.

Such uncertainties arise from both limitations in experimental nuclear data measurements and approximations inherent in the evaluation process, which combines differential experimental data with theoretical nuclear models. Uncertainties are typically represented by probability distributions: the evaluated data are assumed to correspond to the mean values of these distributions, while the reported variances characterize their widths.

One of the objectives of this study is to assess the contribution of nuclear data uncertainty to criticality calculations and the main reactivity effects of fast reactors representative of the ALFRED LFR. Therefore, the propagation of this kind of uncertainty is included in the following section.

2.5.4 Nuclear data uncertainty propagation

Let's suppose that the calculation response depends on parameters α:

$$R = f(\alpha_1, \alpha_2, ..., \alpha_k)$$

and that the true values of the parameters are not known. The nominal values are known, taken as the average value: $(\alpha_1^0, \alpha_2^0, ..., \alpha_k^0)$. The uncertainties given by the standard deviation are known: $(\delta\alpha_1^0, \delta\alpha_2^0, ..., \delta\alpha_k^0)$. The objective of an uncertainty analysis is to obtain the expected value and uncertainty in the response due to

the uncertainties in the parameters on which it depends. As stated in Section 2.4, the sensitivity coefficients can be useful in propagating nuclear data uncertainties. Consequently, a general formulation of the uncertainty quantification based on sensitivity coefficients is introduced.

Considering the input parameters and the response developed around its nominal value

$$\alpha = \alpha^0 + \delta\alpha \tag{2.41}$$

$$\alpha = \left(\alpha_1^0 + \delta\alpha_1, \alpha_2^0 + \delta\alpha_2, \ldots, \alpha_k^0 + \delta\alpha_k\right) \tag{2.42}$$

$$R\left(\alpha_1, \alpha_2, \ldots, \alpha_k\right) = R\left(\alpha_1^0 + \delta\alpha_1, \alpha_2^0 + \delta\alpha_2, \ldots, \alpha_k^0 + \delta\alpha_k\right) \quad , \tag{2.43}$$

then expanding in Taylor series around the nominal values

$$\begin{aligned} &R\left(\alpha_1, \alpha_2, \ldots, \alpha_k\right) = \\ &R\left(\alpha_1^0, \alpha_2^0, \ldots, \alpha_k^0\right) + \sum_{i_1=1}^{k} \left(\frac{\partial R}{\partial \alpha_{i_1}}\right)_{\alpha^0} \delta\alpha_{i_1} + \frac{1}{2} \sum_{i_1, i_2=1}^{k} \left(\frac{\partial^2 R}{\partial \alpha_{i_1} \partial \alpha_{i_2}}\right)_{\alpha^0} \delta\alpha_{i_1}\delta\alpha_{i_2} + \ldots \end{aligned} \tag{2.44}$$

and keeping only the first-order terms (k_{eff} is made a linear function of the parameters):

$$R\left(\alpha_1, \alpha_2, \ldots \alpha_k\right) = R\left(\alpha_1^0, \alpha_2^0, \ldots \alpha_k^0\right) + \sum_{i=1}^{k} \left(\frac{\partial R}{\partial \alpha_i}\right)_{\alpha_1^0} \delta\alpha_i = R_1^0 + \sum_{i=1}^{k} S_i \delta\alpha_i \quad , \tag{2.45}$$

where the quantity $\left(\frac{\partial R}{\partial \alpha_i}\right)_{\alpha^0}$ is equivalent to the absolute sensitivity coefficient as defined in Section 2.4.

If the variance of k_{eff} is calculated considering that the parameters α are distributed according to a probability density function $p(x)$, we obtain:

$$\begin{aligned} \text{var}[R] = E\left[\left(R - R^0\right)^2\right] &= \int_{\alpha\in} \left[\sum_{i=1}^{k} S_i \delta\alpha_i\right]^2 p\left(\alpha_1, \alpha_2 \ldots \alpha_k\right) \mathrm{d}\alpha_1 \mathrm{d}\alpha_2 \ldots \mathrm{d}\alpha_k = \\ &= \left[\sum_{i=1}^{k} S_i^2 \,\text{var}\left(\alpha_i\right) + 2 \sum_{i\neq j=1}^{k} S_i S_j \,\text{cov}\left(\alpha_i, \alpha_j\right)\right] \\ &= \sum_{i,j} \frac{\partial R}{\partial \alpha_i} \frac{\partial R}{\partial \alpha_j} \,\text{cov}\left(\alpha_i, \alpha_j\right) \\ &= \boldsymbol{S}\,\boldsymbol{COV}_{\alpha\alpha}\,\boldsymbol{S}^T \quad , \end{aligned} \tag{2.46}$$

where the vector containing the sensitivity coefficients is $S = (S_1, S_2, \ldots, S_k)$, and $COV_{\alpha\alpha}$ is the covariance matrix. Thus, once the sensitivity coefficients and the covariance matrix are known, the variance of the response can be obtained through the so-called "sandwich rule" [83]. The uncertainty can be expressed in absolute terms (absolute sensitivity coefficients and covariance matrix):

$$\Delta R = \sqrt{\mathbf{S}\,\mathbf{COV}_{\alpha\alpha}\,\mathbf{S}^{\mathrm{T}}} \quad , \tag{2.47}$$

or in relative terms (relative sensitivity coefficients and relative covariance matrix):

$$\frac{\Delta R}{R} = \sqrt{\mathbf{S}_{rel}\,\mathbf{COV}_{\alpha\alpha}\,\mathbf{S}_{rel}^{\mathrm{T}}} \quad . \tag{2.48}$$

2.5.5 Uncertainty quantification algorithm verification

The sandwich formula in Equation (2.48) has been implemented in a stand-alone Python script and subsequently verified against TSUNAMI-IP (Tools for Sensitivity and Uncertainty Analysis Methodology Implementation-Indices and Parameters) [84, 85]. TSUNAMI-IP uses sensitivity data (generated by another SCALE module or directly given in *.sdf* format) and cross-sections covariance data from the SCALE Nuclear Data Covariance Library in 56–energy groups to calculate the uncertainties due to the nuclear data [78].

The same sensitivity vectors, namely the 33-energy group sensitivities from a criticality calculation performed with MCNP on the SNEAK-7B reactor, were given as input to both codes to verify the sandwich rule implemented in Python. Each singular contribution was computed independently using the Python tool and compared with the corresponding TSUNAMI-IP outputs. In Table 2.4, some examples of the individual quantities are presented to show the excellent agreement between the codes. However, when the total uncertainty is computed, a difference of around 200 pcm is obtained (all the values are relative). The reason behind this mismatch is due to the use of slightly different covariance matrices. As introduced before, Python code uses a covariance matrix provided by ENEA for ENDF/B-VIII.0 and processed with NJOY, while the SCALE module uses an AMPX-formatted covariance matrix from the ENDF/B-VIII.0 nuclear data library. TSUNAMI-IP internally converts the data to have a consistent energy-group structure between the sensitivities and the covariance.

By analyzing the TSUNAMI-IP output (see Listing 2.2) and the two covariance matrices, we found out that some significant contributions are not included in either matrix. Cross-correlated values between different nuclides (e.g., fission cross sections for ^{238}U and ^{239}Pu), as well as χ cross-sections of the actinides, are present

Table 2.4: Comparison of $\Delta k_{\text{eff}}/k$ values between SCALE and Python implementations in pcm.

Quantity	TSUNAMI-IP	Python
^{239}Pu fission	625	625
^{238}U fission	136	136
^{238}U capture	308	309
Total uncertainty	1018	808

in the SCALE covariance matrix while they are absent in the ENEA one. The correlation of the fission cross-sections for ^{238}U and ^{239}Pu is represented in Figure 2.3 to illustrate that some cross-correlations between isotopes are missing in the covariance matrix provided by ENEA. Conversely, internal correlations ^{238}U (e.g., elastic-inelastic, inelastic-fission), which contribute significantly to lowering the total uncertainty obtained with Python, are not available in the TSUNAMI-IP matrix.

Listing 2.2: TSUNAMI-IP output (partial reproduction) of the case used for the verification of the sandwich rule.

```
The standard deviation of keff ( % dk/k ) is:
9.991E-01 +/- 3.235E-04 percent
------------------------------------------------------------------------
contributions to uncertainty in keff ( % dk/k ) by individual energy covariance
    matrices:

              covariance matrix
nuclide-reaction  with  nuclide-reaction     % dk/k due to this matrix
-----------------    ------------------     --------------------------
pu-239 fission         pu-239 fission        6.2509E-01 +/- 8.3795E-05
 u-238 fission         pu-239 fission        4.1223E-01 +/- 3.6096E-05
 u-238 n,gamma          u-238 n,gamma        3.0763E-01 +/- 2.3375E-05
 u-235 fission         pu-239 fission        2.9369E-01 +/- 2.8433E-05
pu-239 n,gamma         pu-239 n,gamma        2.4102E-01 +/- 2.8685E-05
 u-238 nubar            u-238 nubar          2.2007E-01 +/- 1.1942E-05
 u-238 inelastic        u-238 inelastic      2.0306E-01 +/- 2.4114E-04
pu-239 nubar           pu-239 nubar          1.9355E-01 +/- 5.9908E-06
 u-238 elastic          u-238 elastic        1.5478E-01 +/- 1.3363E-04
 u-238 fission          u-238 fission        1.3577E-01 +/- 8.1086E-06
```

In Table 2.5, the variances are reported to highlight the specific source of differences. If we take the values from the TSUNAMI-IP columns, subtract the cross-correlations and the Chi contributions, add the U-238 internal correlations, and finally compute the square root, we obtain a total uncertainty of 810 pcm against 808 pcm. These minor differences can be attributed to the different energy groups and weight functions involved during the generation of the matrices.

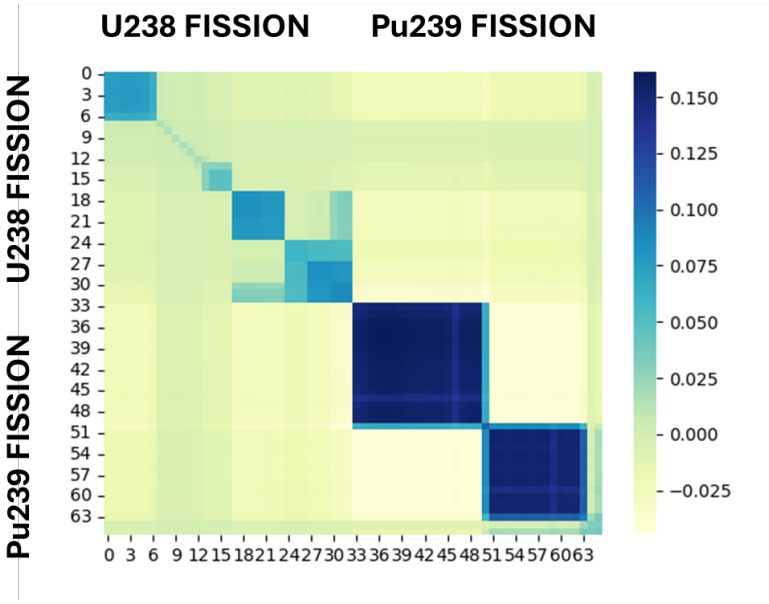

Figure 2.3: ENEA correlation matrix for ^{238}U and ^{239}Pu fission cross-sections using ENDF/B-VIII.0.

In conclusion, given the previous observations, the algorithm can be considered successfully verified, and thus, it will be applied to the selected cases.

Table 2.5: Comparison among the variances obtained from TSUNAMI-IP and Python implementation.

Quantity	**TSUNAMI-IP**	**Python**
^{239}Pu	4.79E-01	4.74E-01
^{240}Pu	7.70E-04	7.48E-04
^{241}Pu	5.09E-05	5.30E-05
^{235}U	7.60E-03	7.45E-03
^{238}U	2.25E-01	1.71E-01
^{16}O	1.29E-04	3.23E-04
^{27}Al	4.99E-05	4.90E-05
Cross-correlations (different isotopes)	2.65E-01	-
χ contributions	5.91E-02	-
^{238}U internal correlations	-	-5.68E-02
Total variance	1.04E+00	6.54E-01

2.6 Data assimilation

2.6.1 Introduction

In nuclear engineering, data assimilation generally refers to the systematic integration of prior computational results with experimental measurements in order to improve model accuracy and reduce uncertainties. In this framework, the model predictions and the covariance matrix associated with the input parameters constitute prior information. At the same time, experimental observations, along with their measurement uncertainties and correlations, are treated as observational data. Therefore, a data assimilation tool implements an inferential framework in which these two sources of information are merged to produce a posterior estimate of a quantity of interest and its updated uncertainty. In safety-critical areas such as reactor design or criticality safety, this approach provides a mechanism to leverage benchmark experiments and measurements to strengthen the credibility of computational predictions. The data assimilation technique that will be presented and used in this work is called Generalized Linear-Least Squares (GLLS).

The GLLS method has its roots in the field of nuclear-data adjustment, where it has been employed for decades to combine results from differential and integral experiments with evaluated nuclear data to produce statistically consistent adjusted libraries [86, 87, 88]. In the context of the PhD dissertation, GLLS provides a deterministic solution to the Bayesian estimation problem, producing a posterior best estimate of ALFRED k_{eff} and its relative uncertainty that minimizes the differences between experimental measurements and calculated quantities. The method relies on sensitivity coefficients that link experimental measurements to the underlying nuclear-data parameters, and on covariance data representing their prior uncertainties. Because the mathematical structure of GLLS is independent of the specific physical meaning of the parameters, the same formalism can be applied to any case where responses depend linearly – or quasi-linearly – on uncertain variables. This property allows GLLS to be extended beyond its first application regarding nuclear-data adjustment to encompass code validation and uncertainty quantification [89]. In this alternative interpretation, the objective is not to modify the evaluated nuclear data themselves but to use the same algorithm to assimilate benchmark results and to quantify the expected bias and uncertainty of a computational prediction for validation purposes.

Sensitivity analysis provides the necessary link between these two domains. By computing the derivative of the effective neutron multiplication factor with respect to each nuclear-data parameter, sensitivity profiles are obtained, and they can be used to describe how the system response varies with differential changes in micro-

scopic cross sections. When these profiles are combined with covariance matrices of nuclear-data uncertainties, they yield both the uncertainty in the calculated k_{eff} for a system and the correlations among different systems. These correlation coefficients express the degree of similarity between benchmark experiments and applications. Nonetheless, correlation analysis alone does not provide an optimal synthesis of all available experimental evidence.

The GLLS approach extends these sensitivity and uncertainty techniques into a complete data-assimilation framework. It can be interpreted as a deterministic Bayesian approach that integrates discrepancies between calculated and measured results, sensitivity profiles, and covariance data into revised estimates of system responses. In this interpretation, GLLS does not merely modify evaluated nuclear data; rather, it directly assimilates experimental evidence into the validation of computational models. Solving the least-squares equations produces a posterior bias and an updated uncertainty for the application under evaluation that are statistically consistent with both the experimental information and its associated correlations.

The following sections therefore, present the mathematical implementation of the GLLS method and its verification.

2.6.2 GLLS method

As previously discussed, GLLS is widely used in nuclear criticality safety assessments. GLLS can be derived from Bayes theory or from a linear least-squares regression analysis. Both derivations can be found in Appendix B.

The primary purpose of the GLLS technique is to correct the bias between an integral parameter's calculated value C and its experimental value E, adjusting calculated values and nuclear data (denoted $\boldsymbol{\sigma}$) using experiments with integral parameters. The adjusted values are usually referred to as posteriors.

All random variables ($\boldsymbol{\sigma}$, $\mathbf{C}$, and $\mathbf{E}$) are assumed to follow multivariate Gaussian distributions, with their uncertainties represented by covariance matrices. $\mathbf{C}$ and $\mathbf{E}$ are vectors of dimension N_E, where N_E is the number of integral parameters considered. $\boldsymbol{\sigma}$ is a vector of dimension N_σ, where N_σ equals the number of isotope/reaction pairs multiplied by the number of energy groups in the multigroup nuclear data.

$\mathbf{C}$ is a function $\mathbf{C}(\boldsymbol{\sigma})$ that expresses the influence of $\boldsymbol{\sigma}$ on the integral parameters.

In GLLS, this relation is approximated by a first-order Taylor expansion around the nominal nuclear data $\boldsymbol{\sigma}_0$:

$$\mathbf{C}(\boldsymbol{\sigma}) \approx \mathbf{C}(\boldsymbol{\sigma}_0) + \mathbf{S}(\boldsymbol{\sigma} - \boldsymbol{\sigma}_0) \quad , \tag{2.49}$$

where $\mathbf{S}$ is the matrix of sensitivity coefficients,

$$\mathbf{S} = \left.\frac{\partial \mathbf{C}}{\partial \boldsymbol{\sigma}}\right|_{\boldsymbol{\sigma}_0} \quad ,$$

with dimensions $N_E \times N_\sigma$. The nuclear data adjustment $\Delta\boldsymbol{\sigma}$ is obtained by minimizing the residual between $\mathbf{C}$ and $\mathbf{E}$ in a least-squares sense, leading to

$$\Delta\boldsymbol{\sigma} = \mathbf{M}_\sigma \mathbf{S}^T \left[\mathbf{S}\mathbf{M}_\sigma \mathbf{S}^T + \mathbf{M}_E + \mathbf{M}_M\right]^{-1} \left[\mathbf{E} - \mathbf{C}(\boldsymbol{\sigma}_0)\right] \quad , \tag{2.50}$$

where $\mathbf{M}_\sigma$ is the prior covariance matrix of the nuclear data ($N_\sigma \times N_\sigma$), $\mathbf{M}_E$ is the covariance matrix of the experimental integral parameters ($N_E \times N_E$), and $\mathbf{M}_M$ accounts for modeling and methodological uncertainties ($N_E \times N_E$).

The posterior nuclear data are then given by

$$\boldsymbol{\sigma}' = \boldsymbol{\sigma}_0 + \Delta\boldsymbol{\sigma} \tag{2.51}$$

and their posterior covariance matrix is

$$\mathbf{M}'_\sigma = \mathbf{M}_\sigma - \mathbf{M}_\sigma \mathbf{S}^T \left[\mathbf{S}\mathbf{M}_\sigma \mathbf{S}^T + \mathbf{M}_E + \mathbf{M}_M\right]^{-1} \mathbf{S}\mathbf{M}_\sigma \quad . \tag{2.52}$$

The posterior calculated integral parameters, $\mathbf{C}'$, are then approximated by

$$\mathbf{C}'(\boldsymbol{\sigma}') \approx \mathbf{C}(\boldsymbol{\sigma}_0) + \mathbf{S}\Delta\boldsymbol{\sigma} \quad , \tag{2.53}$$

and the updated uncertainty due to the nuclear data component is

$$\mathbf{V}'_C = \mathbf{S}\mathbf{M}'_\sigma \mathbf{S}^T \quad . \tag{2.54}$$

These equations represent the general form for the posterior quantities. For this application, they are declined as follows, highlighting the contribution of the integral benchmarks to obtain the posterior values for the application case:

$$\mathbf{C}'\left(\boldsymbol{\sigma}'\right) = \mathbf{C}\left(\boldsymbol{\sigma}_0\right) + \mathbf{S} \cdot \mathbf{M}_\sigma {\mathbf{S_B}}^T \left[\mathbf{S_B}\mathbf{M}_\sigma {\mathbf{S_B}}^T + \mathbf{M}_\mathrm{E} + \mathbf{M}_\mathrm{M}\right]^{-1} \left[\mathbf{E} - \mathbf{C}\left(\boldsymbol{\sigma}_0\right)\right] \tag{2.55}$$

$$\begin{aligned} \mathbf{V}'_C &= \mathbf{S}\mathbf{M}'_\sigma \mathbf{S}^T = \\ &= \mathbf{S}\left(\mathbf{M}_\sigma - \mathbf{M}_\sigma {\mathbf{S_B}}^T \left[\mathbf{S_B}\mathbf{M}_\sigma {\mathbf{S_B}}^T + \mathbf{M}_\mathrm{E} + \mathbf{M}_\mathrm{M}\right]^{-1} \mathbf{S_B}\mathbf{M}_\sigma\right)\mathbf{S}^T \quad . \end{aligned} \tag{2.56}$$

Here, the matrix of sensitivity coefficients $\mathbf{S}$ comprises both the application and the benchmarks' sensitivity coefficients, while $\mathbf{S_B}$ specifies when only the benchmark coefficients are taken into account.

Since biases in simulation results depend on the configuration of critical experiments, selecting representative experiments is essential. The selection of the experiments for the data assimilation step is guided by a sensitivity-based correlation metric, commonly referred to as representativeness (or representativit) factor. This quantity quantifies the similarity between the sensitivity profiles of the applications and those of the benchmark cases, providing a numerical criterion for ranking experiments according to their relevance to the reference case.

Nevertheless, it is not trivial to properly account for correlations among benchmark experiments. Such correlations may arise not only from shared nuclear-data sensitivities, which are explicitly treated within the GLLS formalism, but also from common experimental characteristics and modelling features (e.g., similar geometries, fuel types, fuel forms, moderation conditions, or the presence of control rods). The ORNL study [76] indicated that reliable bias estimates typically require at least five highly correlated or about ten moderately correlated experiments (with respect to the reference case/reactor), offering a practical criterion for assessing the adequacy of benchmark coverage.

Within the GLLS algorithm, the experimental contributions are incorporated following the cases with higher representativeness. These experiments present a stronger influence on the posterior bias and uncertainty estimates than less representative configurations. At this stage, it is essential to understand how benchmarks enter the GLLS formulation and how their relative importance is quantified within the covariance structure. A rigorous definition of the representativeness factor and its practical computation will be presented in the following chapter (see Section 3.3), once the experimental dataset has been established.

To summarize the methodological advantages of the approach in the context of criticality-safety validation, GLLS provides a unified, transparent statistical structure that merges nuclear-data uncertainties, benchmark results, and application sensitivities into a single covariance framework.

2.6.3 GLLS algorithm verification

The relevance of GLLS to contemporary criticality-safety methodology is underscored by ongoing activities of the OECD Nuclear Energy Agency's Working Party on Nuclear Criticality Safety (WPNCS) [90]. Subgroup 11 first established Bayesian and least-squares methods for feedback from integral experiments to

nuclear-data evaluations [91], while Subgroup 14 has extended these principles to data assimilation and uncertainty quantification for criticality-safety validation [92]. Both subgroups identify the GLLS approach as the reference deterministic realization of Bayesian data assimilation, particularly suitable when full stochastic sampling is computationally impractical.

In this framework, the first-order approximation of the posterior calculated value and the uncertainty of the reference case ALFRED were implemented in Python using Eq. (2.55) and (2.56). To verify the correctness of the code, the *"Intercomparison Exercise on Bias and Correlated Data, Comparison of Methods"*, a task of the WPNCS - Subgroup 11 (WPNCS/SG11) [91], is used as a reference to prove that the in-house script could reproduce the same results. For the posterior calculated value, the values are given as the posterior bias, defined as

$$\mathbf{C}'\left(\boldsymbol{\sigma}'\right) - \mathbf{C}_{APP} \quad [\text{pcm}] \quad . \tag{2.57}$$

The verification against the reference implementation was performed using the L_2 norm of the deviation vectors. As reported in Table 2.6, all cumulative quantities exhibit exact numerical agreement, while the singular bias differs by 1 pcm due to rounding effects. No other deviations were observed.

Table 2.6: L_2 norm of deviations with respect to reference results (pcm).

Correlation	Singular Bias	Cumulative Bias	Cumulative Uncertainty
–	1	–	–
0.00	–	0	0
0.70	–	0	0
0.99	–	0	0

The excellent agreement is also represented in the following plots. Comparing Figure 2.4, which represents the posterior biases obtained by SG11, with Figure 2.5, which shows the results obtained from the methodology implemented during this thesis, allows to visually appreciate the reproducibility of the reference results. In Figure 2.4, the posterior bias is presented for different cases representing increasing correlation among the benchmarks. On the left side of the plot, the black line represents the effect of a singular benchmark, where $BM9$ is the least similar benchmark, while the most similar is $BM1$. On the right side, the black line, the green line, and the red line indicate the effect of incrementing the number of benchmarks from the more similar to the less, for the case with no experimental correlation among the benchmarks (0.00), medium correlation (0.70), and strong correlation (0.99), respectively. Figures 2.6 and 2.7 show the trends of the

posterior uncertainty $\mathbf{V}'_C$ calculated by SG11 and by the implemented algorithm, respectively. The same considerations for the correlation cases exposed before also apply for the updated uncertainty.

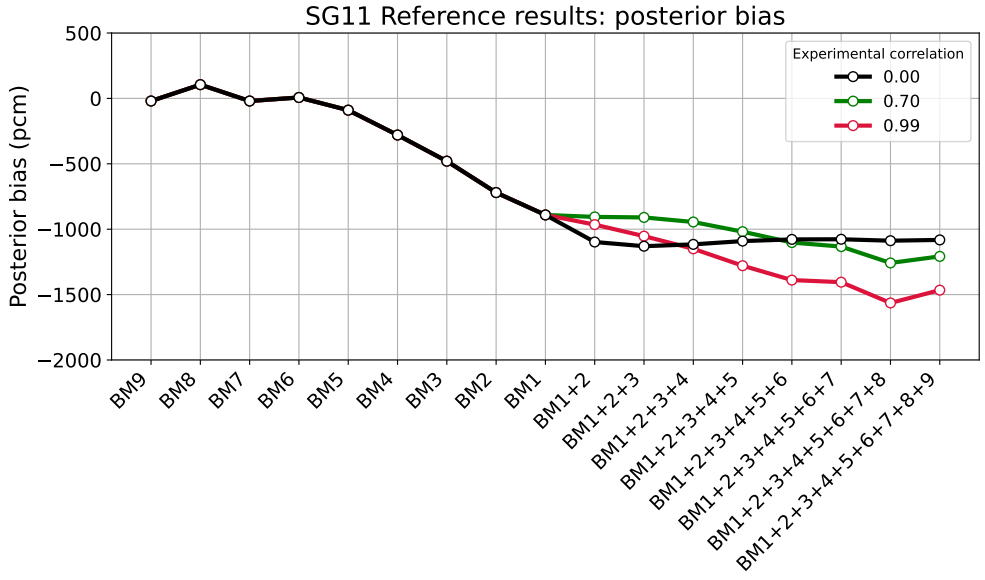

Figure 2.4: Results from SG11 for GLLS method for the application case with experimental uncertainty 0.01.

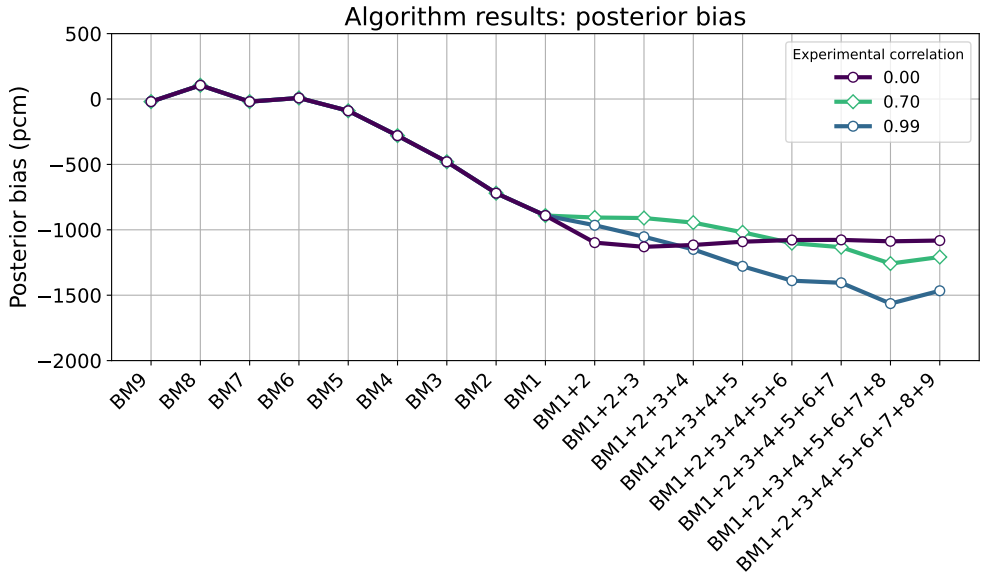

Figure 2.5: Results from the Python algorithm for the application case with experimental uncertainty 0.01.

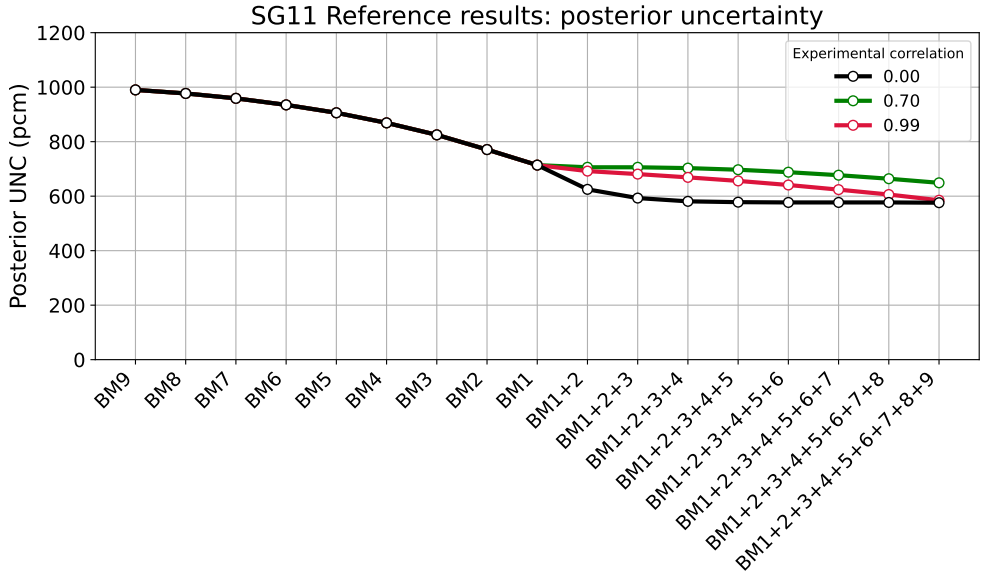

Figure 2.6: Results from SG11 for GLLS method for the application case with experimental uncertainty 0.01.

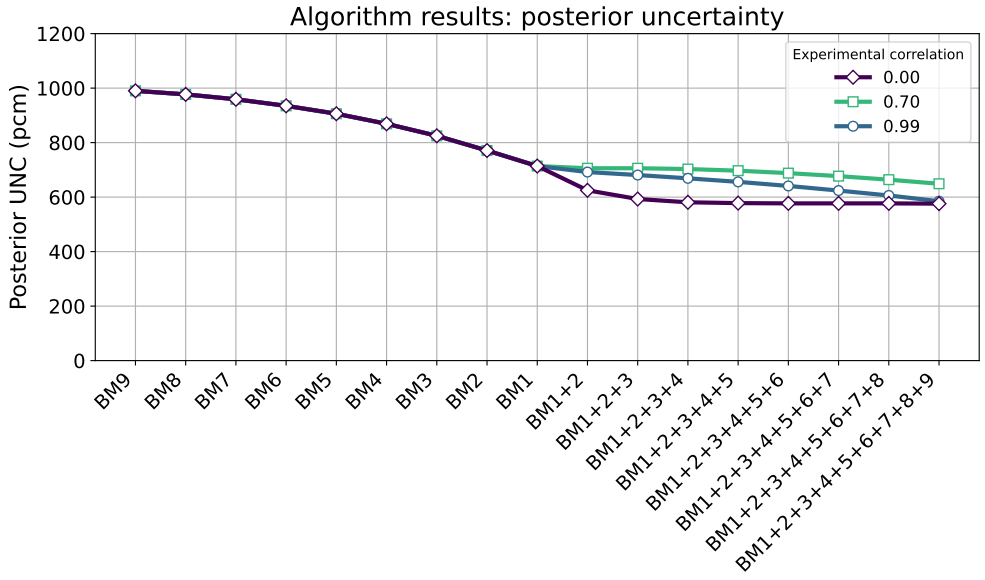

Figure 2.7: Results from Python algorithm for the application case with experimental uncertainty 0.01.

2.7 A Python-based framework for uncertainty quantification and data assimilation for LFR

Uncertainty quantification and data assimilation are critical for accurate modeling and analysis of neutronics parameters in LFRs. One of the main outcomes of this work is the development of a Python-based framework that integrates MCNP simulations' results with nuclear data uncertainty propagation, and a criticality safety assessment method was developed. The objective is twofold: to quantify the impact of nuclear data uncertainties on reactor observables and to provide an improved estimate of the effective multiplication factor for the reference case ALFRED.

Although similar capabilities exist within established codes such as TSUNAMI-IP or TSAR packages from SCALE [77, 81], one major drawback is that these tools are not open-source and offer limited integration with customized post-processing workflows. The framework proposed here addresses this limitation by providing a fully adaptable and that can easily be integrated into the internal solution. Its implementation was verified against licensed codes during a research stay at the Nuclear Engineering Department of UPM, ensuring methodological reliability while preserving the required flexibility. As already introduced in Section 1.4, besides the adaptability of the tools, the verification process is a key aspect to

support the broader qualification process of calculation packages for LFR design applications.

The framework expands the capabilities of an already established internal Python-based workflow. In addition to the first reason of using Python [93] as a programming language, a key advantage is its versatility and ease of integration with MCNP outputs. Since MCNP primarily produces raw output files, extensive efforts in post-processing are often required to extract relevant information, such as tallies or, in this case, sensitivity coefficients. The developed tools automate the parsing and manipulation of these files, enabling structured data handling and efficient extraction of numerical results. Furthermore, the Python scientific library ecosystem [94], facilitated the implementation and testing of algorithms for this project.

The framework consists of four main modules:

1. **MCNP output manipulation**:
    - Conversion of MCNP output files (which contains the computed sensitivities) into *.sdf* format, enabling standardized comparison with sensitivity files from other codes or cases.
    - Sensitivity ranking to identify the princiapl contributors.
    - Conversion from *.sdf* to *.npy* format for numerical processing.
    - Generation of new sensitivity coefficient for reactivity effects cases by combining the *.sdf* file from nominal and perturbed runs, with outputs available in both *.sdf* and *.npy* formats.
2. **Covariance Matrix generation**. A dedicated script reads the ENEA correlation matrix and builds the covariance matrix for a specific application by selecting the isotopes and reactions of interest. The resulting matrix is exported as *.npy* files for direct use in UQ and GLLS algorithms.
3. **Uncertainty Quantification**. A standalone script recalls the previously generated sensitivity and covariance *.npy* files and propagates the nuclear data uncertainty of the selected cases. The separation of these modules allows efficient handling of cases involving numerous isotope-reaction correlations.
4. **Data Assimilation**. A Python implementation of the GLLS method processes the *.npy* file for sensitivities and the covariance matrix, evaluates similarity, reorders the cases, and computes both singular and cumulative contributions for k_{eff} model updating.

Furthermore, the framework is not library-dependent, except for the covariance matrix, which is given and is part of a previous workflow. Although the ENDF/B-VIII.0 was adopted for consistency with previous works, the developed tools can be applied to different libraries, allowing for further comparison studies, which are not the focus of this thesis.

Overall, the proposed framework provides a rigorous yet flexible environment for analyzing nuclear data uncertainty contributions to several reactivity parameters derived from MCNP simulations and for updating the model predictions using available experimental measurements. Its modular architecture facilitates possible extension to other applications in the reactor core design domain. In this work, the code under study for the qualification process is MCNP version 6.3.0; however, the methodology can be adapted to any neutronics code that can provide sensitivity data, including deterministic codes, along with a consistent covariance matrix. The integrated structure of the framework is summarized in Figure 2.8.

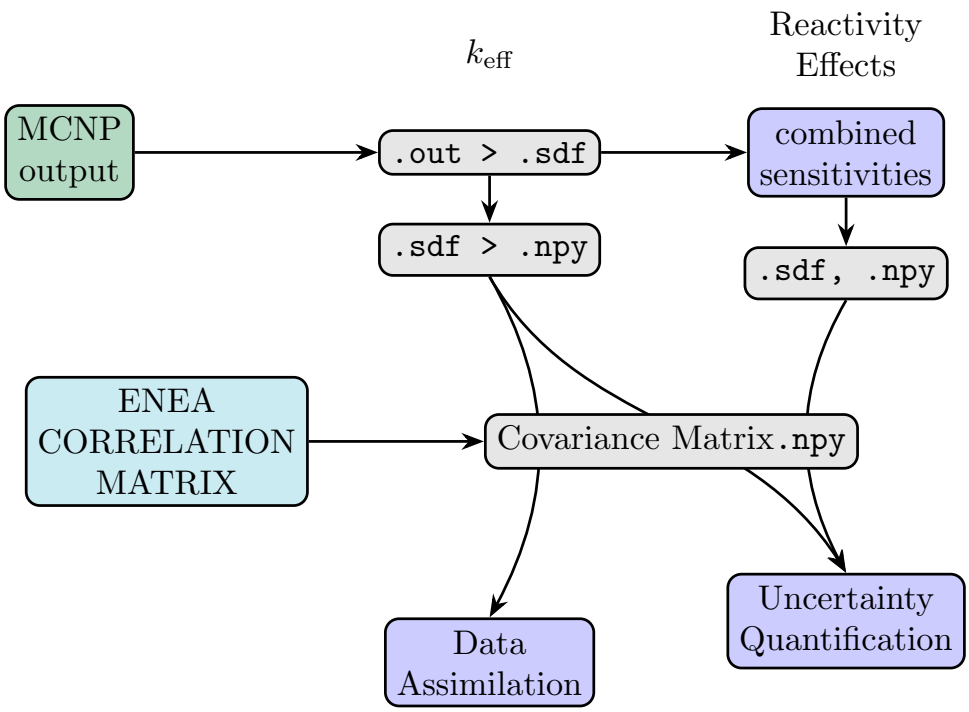

Figure 2.8: Uncertainty quantification and data assimilation framework.

Chapter 3

Experiments selection from IRPhE

As previously introduced, the uncertainty quantification assessment is based on a selection of cases from the IRPhE handbook that are representative of the ALFRED reactor. In particular, the reactor type from which the heuristic evaluation started is Liquid Metal-cooled Fast Reactors (LMFR).

This chapter is organized as follows: first, an introduction is given to the IRPhE database and its graphical interface IDAT, which allows easier searching for cases of interest. Secondly, the motivations that drove the choice of the simulated experiments for evaluating the code's reactivity parameters prediction accuracy are discussed. Then, a section is introduced, dedicated to the characterization of the selected maquettes, and the representativeness values calculated using the sensitivity coefficients obtained with MCNP calculations. Finally, the last section is dedicated to additional reactor physics parameters not considered in this work due to the computational limits of MCNP, which can be useful for code validation purposes in fast reactor applications.

IRPhE and IDAT tool

The Nuclear Energy Agency (NEA) handbooks are extensively exploited for code validation purposes. Also at Los Alamos National Laboratory, MCNP developers included fundamental reactors from ICSBEP in their verification and validation test suite [47] for criticality assessments. Several reactor types are present in the IRPhE database: Boiling Water Reactor (BWR), Gas Cooled Fast and Thermal Reactor (GCFR and GCR, respectively), Heavy Water-moderated Reactor (HWR), Liquid Metal-cooled Fast Reactor (LMFR), Light Water-moderated Reactor (LWR), Molten Salt Reactor (MSR), Pressurized Water Reactor (PWR), RBMK, SPACE, and VVER reactors. Since ALFRED is a lead-cooled fast reactor, the domain was restricted to LMFR facilities only, as the ones in the total list

that are constitutively bound to be the most representative.

The content of the ICSBEP and IRPhE handbooks, which was already extensive and continues to grow edition after edition, required the creation of a dynamic database structure to gather and enhance their usability. As a consequence, the Database for the International Handbook of Evaluated Criticality Safety Benchmark Experiments (DICE) was released specifically for the ICSBEP Handbook in 2003 [95]. About ten years later, the IRPhEP Database and Analysis Tool (IDAT) [96] was made available with the IRPhEP handbook. These relational databases include preselected information from each of the benchmark evaluations. Moreover, they also include calculated quantities of the reactor cases, such as neutron flux, fission spectrum data, or sensitivity data. For LMFR, very few sensitivities are present compared to the extension of this section, and for very limited libraries (e.g, ENDF/B-VI.0 sensitivities for BR2 facility and ENDF/B-VII.0 library for FFTF and SNEAK). Nevertheless, the interface developed for these tools allows users to query the chosen parameters to identify benchmarks suitable for their specific needs. Both DICE and IDAT have plotting capabilities for the different parameters loaded, which are useful for comparing different experiments. In general, these database tools considerably simplify the search for validation cases from the various reactor types and their respective benchmark measurements.

Due to the numerous cases and parameters involved, IDAT was indeed used for the initial heuristic selection and to identify the measurements available for the parameters of interest.

3.1 Selection Criteria

The cases available in the IRPhE are numerous, but not all of them fit the purpose of the intended study. Surely, a focus on LMFR reactors is required, which already significantly reduces the number of candidate facilities to 9, which include 36 cases. Among these, however, a further selection is needed, as not all have the technical characteristics required to represent the reference reactor of interest, ALFRED. A preliminary selection was therefore conducted using a qualitative physics-driven approach to screen the most promising cases, which will be subsequently confirmed or ultimately disregarded by means of a quantitative evaluation of the physical representativeness of each configuration.

The following physical characteristics were considered and used as driving criteria for the screening.

- Core configuration and the presence or absence of symmetries (the ALFRED core is largely symmetric).
- Presence of moderating materials that affect the spectrum hardness and the integral parameters in general.
- Spectrum profile, which has to be as close to the ALFRED one as possible, especially in the most important range from 1 keV to 1 MeV, with a mean energy of 400-450 keV.
- Fertile material, its presence having an impact on the spectrum characteristics.
- ALFRED is a power reactor, so similar systems would have been preferred. However, only FFTF and JOYO are power reactors, since most of the experiments concern zero-power configurations of critical reactors.
- The type of measurements (criticality, control rod worth, coolant void coefficients, spectral indices, etc.) available for each facility, taking the most out of the dataset.

Regarding the last bullet point, a specification that has already been introduced in Chapter 2 is mandatory. The scope of this work is to assess the reliability of MCNP simulation capabilities when applied to LFRs, but regarding the reactor physics parameters for which it is possible to compute sensitivities with the chosen Monte Carlo code, so to be able to propagate the input uncertainties via the so-called sandwich rule. Consequently, the parameters of primary interest are: the effective multiplication factor (k_{eff}), the Control Rod Worth (CRW), the coolant void coefficient, which, since all the measurements are for sodium voiding effects, can be referred to as Sodium Void Reactivity (SVR), and the temperature coefficient (or Isothermal Temperature Coefficient (ITC)) of reactivity. Section 3.4 will be dedicated to the reactivity coefficients and effects measurements that are covered in the IRPhE database, and to clarify why sodium void coefficient measurements have been included in the study.

A description of the facilities evaluated is briefly presented in the following subsections, using the information provided by the IRPhE handbook [55].

3.1.1 BFS

The Institute of Physics and Power Engineering (IPPE) in Obninsk, Russia, hosts two critical facilities, BFS-1 and BFS-2, aiming to provide a unique experimental

data source for reactor physics and criticality safety problems. At the BFS facility, integral experiments were carried out intended to study the neutronics of fast reactors with different fuels (uranium metal, uranium dioxide and nitride, plutonium metal, MOX fuel) and coolants (sodium, lead, lead-bismuth, hydrogen-containing coolants). Some of these experiments have been evaluated and included in both the IRPhEP and ICSBEP Handbooks.

The first facility, BFS-1, was established as a versatile experimental platform for detailed neutronic simulation of fast-reactor systems. Its primary objective was to reproduce core, blanket, reflector, shielding, and fuel-storage configurations and to obtain high-fidelity experimental data required for the validation of neutron constants, calculation codes, and advanced reactor design methodologies. The core volume is variable and it can enable both small-scale studies and full-scale mock-ups representative of fast reactors with thermal capacities approaching 1000 MW. Since its commissioning in June 1961, the installation has hosted numerous prototype configurations and benchmark experiments.
Between 1990 and 1991, three critical experiments using heterogeneous arrangements of plutonium, depleted uranium, graphite, and lead were conducted here. The main purpose of this campaign was to obtain supplementary integral benchmark measurements to support neutronic validation and design activities for LFRs concepts, and it still is the only benchmark case in IRPhE involving lead. All three configurations presented similar core compositions while differing in their radial reflector designs.

- **BFS-61-0**: consisted of a core surrounded by a radial reflector composed of successive layers of lead, steel, and depleted uranium dioxide (Fig. 3.1).
- **BFS-61-1**: maintained essentially the same core dimensions but utilized a reflector consisting of lead and depleted uranium dioxide layers.
- **BFS-61-2** consisted of a core of similar height with an increased diameter. In this case, the lateral reflector was composed solely of depleted uranium dioxide.

Among several configurations included in the database from the BFS-1 facility, the BFS-73-1 critical experiment is a benchmark of a sodium-cooled fast reactor with metal uranium fuel of 18.5% average enrichment. The critical assembly was a simple system, without control rods in the core. Axial and radial blankets were depleted uranium dioxide. The experiment was performed in 1997.

On the other hand, the BFS-2 critical facility was designed in IPPE for full-size simulation of the core and shielding of large fast reactors with a power up to 3000

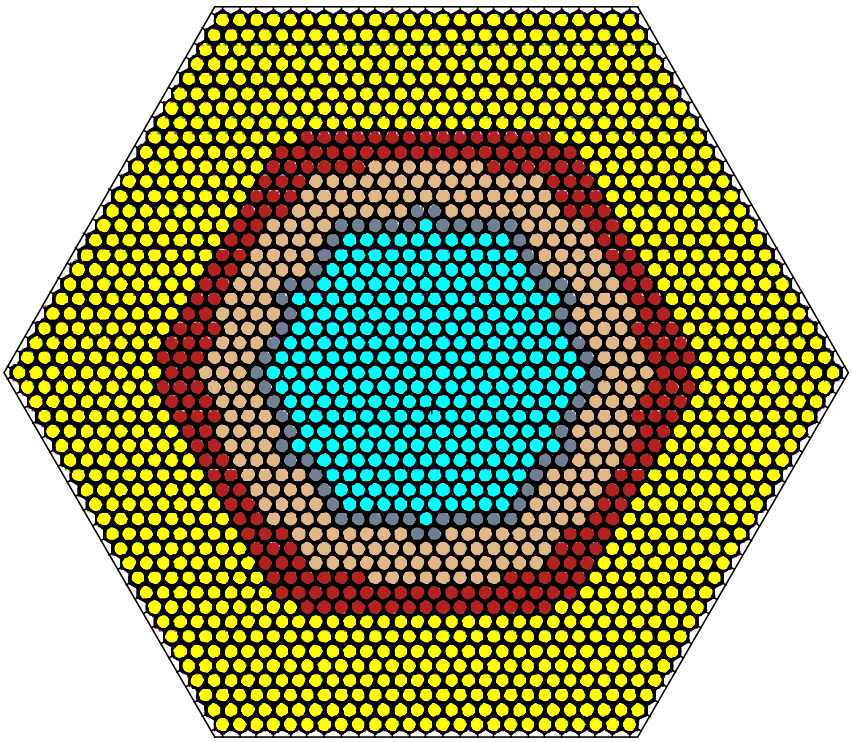

Figure 3.1: Schematic of the BFS-61-0 core map [55].

MWt, and it was put in operation in October 1969. BFS-2 included the critical experiment BFS-62-3A, which is one of the variants in the simulation series of the BFS-62 experiments for the sodium-cooled BN-600 reactor with hybrid U-Pu fuel and stainless-steel reflector. The core size is approximately 1 meter in height and 2 meters in diameter, with a thickness of 50 and 70 cm for the axial and radial blankets, respectively. BFS-62-3A core is a 4-zone system: Inner Core (LEZ), Middle Core (MEZ), Plutonium Enrichment Zone (PEZ), and Outer Core (HEZ), without any control rods within the core.

3.1.2 BR2

BR-2 reactor was also developed at IPPE in Obninsk, Russia. The system was a fast reactor with a nominal thermal power of 200 kW, cooled by mercury. The core, composed of stainless-steel-canned plutonium metal fuel rods in a hexagonal lattice, was very compact. Several kinds of rods were also used in the core, such

as depleted uranium rods, iron rods, and testing rods. The lateral reflector used depleted uranium metal. The active part of the core is pseudo-cylindrical, having a height and diameter of 13 cm. The BR-2 facility was built for research into fast neutron physics and technology developments. In fact, it was equipped with several experimental devices, such as vertical and horizontal channels, and large graphite thermal columns. Horizontal and vertical views of the BR-2 reactor are reported in Fig. 3.2.

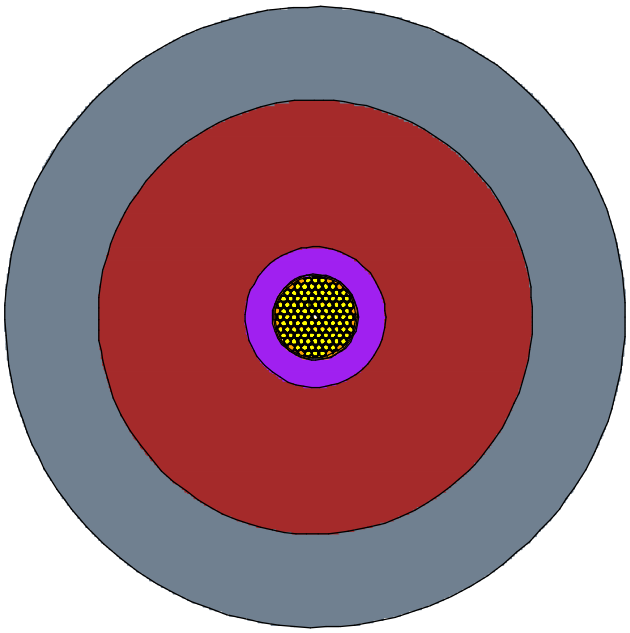

Figure 3.2: BR-2 reactor: horizontal and vertical cross sections [55]

.

3.1.3 EBR2

The Experimental Breeder Reactor-II (EBR-II) was a test reactor operated by Argonne National Laboratory from 1964 through 1994. The sodium-cooled fast reactor had a thermal output of 62.5 MW. Although initially designed to breed more fuel than it consumed, it was later reconfigured to operate as an irradiation facility. Here, a variety of fuels (enriched uranium metal alloyed with a small percentage of other elements at first, recycled fuel later) and structural materials were tested. The EBR-II had 637 vertical removable assemblies in a hexagonal lattice.

These assemblies were divided into three regions: the core, an inner blanket, and an outer blanket. The inner blanket initially contained depleted uranium to breed new fissile material. When it was turned into an irradiation facility, the depleted uranium assemblies were replaced with stainless-steel ones to reflect neutrons toward the center of the core. The outer blanket region consisted almost entirely of depleted uranium assemblies.

3.1.4 FFTF

The Fast Flux Test Facility (FFTF) was a U.S. experimental fast reactor with a 400 MW thermal power. It was a fast-spectrum reactor using sodium as coolant, under low-pressure and high-temperature conditions. The objective of the design was to study fast breeder reactors and to provide an irradiation platform for qualification and performance testing of nuclear fuels and structural materials for advanced reactors. The FFTF was employed from February 1980 to April 1992. Throughout its decade of operation, the FFTF served as a national research center to examine advanced nuclear fuels, materials, components, systems, operational and maintenance practices of nuclear power plants, as well as both active and passive safety technologies for reactors. It also generated a significant quantity of isotopes for medical and industrial applications, evaluated materials for the U.S. fusion research initiative, and engaged in collaborative international research efforts.

Due to the testing nature of FFTF, the composition and arrangement of the core were changed to meet the requirements for varying testing procedures. In the benchmark case, however, the core comprised 199 replaceable hexagonal assemblies (Fig. 3.3), with the fuel bundle bearing PuO_2-UO_2 pellets enclosed in stainless steel claddings. The assemblies had two different fuel enrichments in Pu: 22.4% and 27.4% in the inner and outer regions, respectively. FFTF had nine control rods with B_4C as absorber; inconel reflectors were utilized to reduce neutron leakage.

3.1.5 JOYO

The first Japanese experimental fast reactor employing sodium as coolant was JOYO. The facility was built at the O-arai Engineering Center of the old Power Reactor and Nuclear Fuel Development Corporation (PNC), which is now part of the Japan Atomic Energy Agency (JAEA). Construction activities began in 1970, and it was completed in 1977. The initial core configurations consisted of 64 core fuel assemblies (FAs), which represent a critical state with all control rods fully

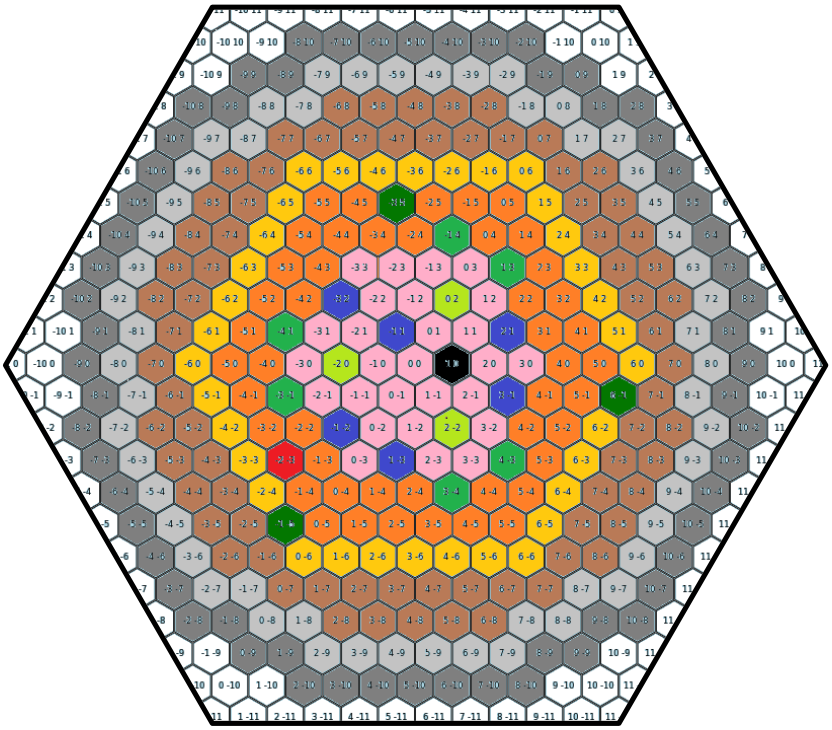

Figure 3.3: Schematic view of the FFTF core map [55]

withdrawn. The second core contains 70 FAs, with approximately half of the two regulation rods inserted into the core fuel region. FAs were disposed in a hexagonal arrangement, and the fuel was MOX, with highly enriched uranium (23% of ^{235}U). An axial blanket of depleted uranium oxide surrounded the fuel region. The power operation, initially rated at 50 MWth, was performed from April 1978 to February 1979, followed by upratings to 75 MWth (from July 1979 to December 1980) and 100 MWth (up to date). For the benchmark evaluations, two startup core cases are reported. In both cases, reactivity control was achieved using B_4C absorber rods. The first case proposed reproduces the clean core with 64 FAs, while the second case represents the subsequent extension to 70 FAs (Fig. 3.4), which corresponds to the configuration to reach 50 MWth power operation. Besides criticality, control rod worth and sodium void reactivity benchmark problems, the JOYO facility also provided measures of the coefficients of isothermal temperature reactivity and burnup, both of which are very rare and almost unique among the cases included in the LMFR evaluations of the IRPhE.

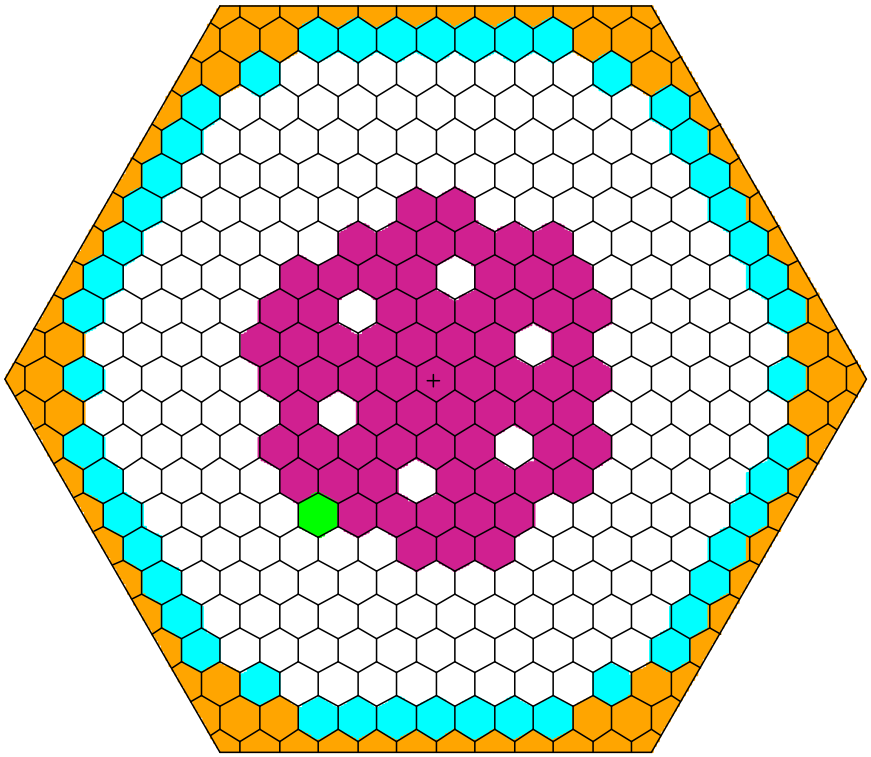

Figure 3.4: Core configuration of the JOYO 70 fuel assembly experiment [55].

3.1.6 SNEAK

At the Karlsruhe Fast Critical Facility, two fast-critical experiments were constructed under the names SNEAK 7A and 7B. Both configurations employed PuO_2-UO_2 fuel and metallic depleted uranium as reflector. SNEAK, the acronym for Fast Zero-Power Facility Karlsruhe in German, was a zero-power research installation dedicated to reactor-physics investigations and mock-up studies. The facility operated between 1966 and 1985, while the experimental campaigns for SNEAK-7A and SNEAK-7B were conducted in 1970 and 1971, respectively. The SNEAK reactor was a fixed vertical assembly with fuel elements suspended from a grid plate. Platelets of various thicknesses were stacked horizontally within square fuel element tubes. In SNEAK-7A, the core unit cell consisted of one PuO_2-UO_2 platelet (26.6% PuO_2) and one graphite platelet, of different thicknesses. Radial and axial blankets were loaded with depleted UO_2 plates. In SNEAK-7B (Fig. 3.5, the graphite platelet in the cell of the 7A configuration was replaced by a 0.6256 cm thick UO_2 slab (natural uranium was employed), resulting in an average Pu-enrichment of about 13%. By leveraging the extremely simple and clean nature

of the adopted configurations, an extensive experimental program was completed in both cores, obtaining high-quality data for code validation of different integral parameters.

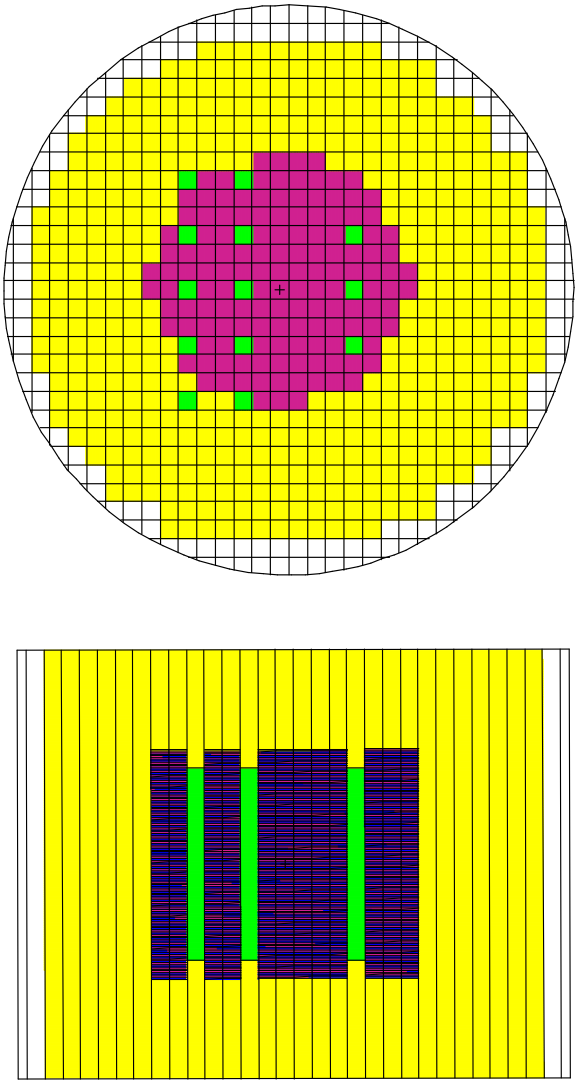

Figure 3.5: Core configuration and cross-cut of the SNEAK-7B experiment [55].

3.1.7 ZEBRA

The ZEBRA (Zero Energy Breeder Reactor Assembly) installation was a British fast-spectrum critical facility that operated from 1962 to 1982. It served primarily as an experimental platform for the validation of fast reactor neutronics methods. The facility was designed with considerable geometric and compositional flexibility, enabling the construction of cores, fertile blankets, and shielding arrangements over a broad range of material combinations and dimensional scales. Regarding the ZEBRA-001 experimental campaign, four assemblies were realized, designated from 22 to 25.Each configuration had an active core zone enclosed by a surrounding blanket region and additional layers of steel and shielding materials, thereby establishing a controlled and well-characterized experimental environment. Depending on the specific assembly, the core and breeding regions were implemented either using plate-type fuel elements or pin-cell lattice arrangements.

- Assembly 22: fuel in plate form and included sodium.
- Assembly 23: pin form (most of the material in the core) and also included sodium.
- Assembly 24: differed from Assembly 22 because the sodium plates were replaced by "dummy plates" having the same size and containing the same amount of steel but no sodium, in order to simulate a completely voided configuration.
- Assembly 25: differed from Assembly 23, having the sodium regions of the Assembly 23 elements being voided.

The core regions of Assemblies 22 and 24 were essentially uniform. In contrast, Assemblies 23 and 25 had outer rings made of plates enclosed within thin steel cladding, forming structural elements approximately 5×5 cm in cross section and about 3 m in length, and used mini-calandria containing groups of 4x4 pins having different plutonium enrichments in different regions of the core. The surrounding blanket and shielding zones were dimensioned to be sufficiently thick to decouple the core neutron field from any external materials beyond the shield, thereby minimizing boundary effects on the measured neutronic characteristics. Nine control rods were present. Between 1971 and 1973, a further series of experiments was made in the ZEBRA facility during the MOZART Programme. This was a joint project between UKAEA and PNC to support the design of MONJU, the Japanese sodium-cooled, plutonium-uranium oxide-fueled fast reactor. The measurements were performed in three phases called MZA, MZB, and MZC. MZA had

a one-region core, without control rods, with metal plutonium fuel and UO_2 plates arranged in a quite complex configuration; MZB had instead a two-region core, without control rods and with the same fuel and a similarly complex geometrical arrangement. In the MZC configuration, the reactivity worth of MONJU mock-up control rods was measured. The three versions also differed in the radial blanket arrangement.

3.1.8 ZPR

The Zero Power Reactor (ZPR) was constructed at the Argonne National Laboratory, Idaho (USA), to support fast reactor development and nuclear data validation. From 1966 to 1996 over a hundred different assemblies were built at the facility, including ZPR-6, ZPR-6, ZPR-9 and ZPPR.

ZPR-3 Assembly 48 and its variants, 48A and 48B, were the first in a series of plutonium-fueled assemblies constructed in ZPR-3 to provide integral data for benchmarking fast reactor calculation methods and data. The core of ZPR-3a48 consisted of small plates of Pu-Al alloy, Pu-U-Mo alloy, graphite, depleted uranium and sodium loaded into stainless steel drawers which were inserted into square stainless steel tubes in a 31 x 31 matrix. The core was surrounded by thick depleted uranium radial and axial blankets. ZPR-3 Assembly 48A (ZPR-3/48A) had the same core loading as ZPR-3/48. At the end of the ZPR-3a48A measurement program, ZPR-3 Assembly 48B (ZPR-3/48B) was constructed by restoring the full depleted uranium radial blanket and by replacing the first 6 in. (152.4 mm) of the column of standard Pu-Al fuel plates by highly enriched, in the $^{2}40$Pu isotope, Pu-Al fuel plates in the central 37 core drawers.

ZPR-3 Assembly 56B (ZPR-3/56B) was part of a series of critical experiments performed to support the design of the Fast Test Reactor, as was initially designated the reactor part of the FFTF plant. The geometry of Assembly 56B was relatively simple, and the principal materials used were limited to Pu-U-Mo alloy fuel, sodium, sodium carbonate, iron oxide, depleted U_3O_8, nickel, along with the stainless steel in the matrix tubes, drawers and claddings.

Finally, the ZPR-6 Assembly 7 (ZPR-6/7) comprises a series of experiments performed at the ZPR-6 facility between 1970 and 1971 as part of the Demonstration Reactor Benchmark Program. Assembly 7 simulated a large sodium-cooled LMFR with MOX fuel, depleted uranium radial and axial blankets, and a core with a height-to-diameter ratio near unity. ZPR-6a7(1) had a highly homogeneous core constituted of small plates of depleted uranium, sodium, iron oxide, depleted U_3O_8, and Pu-U-Mo alloy loaded into stainless steel drawers. The lattice design

employed a straightforward and symmetric unit cell, with the neutron balance primarily governed by the fissile contribution of ^{239}Pu and the fertile component ^{238}U. The core was surrounded by thick radial and axial reflectors of depleted uranium to simulate radial and axial blankets and to isolate the core from the surrounding room. Also, a second configuration of ZPR-6a7, named ZPR-6a7(2), with the innermost region of the core loaded with plutonium fuel highly enriched in the ^{240}Pu isotope, similarly to ZPR-3a48B (Fig. 3.6), was experimentally investigated in order to better validate the specific isotope-related nuclear data.

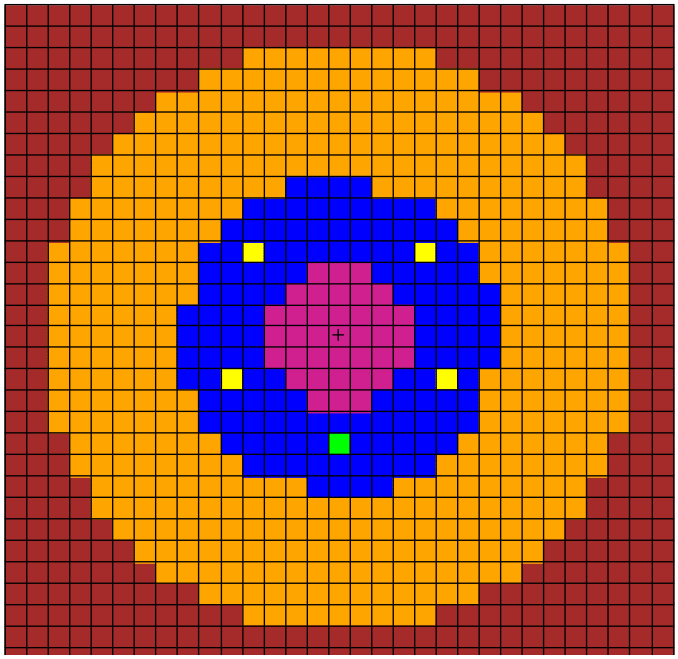

Figure 3.6: Core configuration of the ZPR-3/48B experiment [55].

3.1.9 ZPPR

The ZPPR (Zero Power Plutonium Reactor) program began in March 1969 at Argonne National Laboratory in Idaho, USA. The facility represents an enhancement over the previous ZPR facility, sharing the same fuel type and the plate-drawer core design, to examine the nuclear properties of large Fast Breeder Reactor cores. Most of its earlier assemblies (i.e., assemblies 2 through 8 and assemblies 11 and 12) supported the Demonstration Reactor Benchmark Program and the Clinch River Breeder Reactor. Accepted as benchmarks are the ZPPR-010(12) and ZPPR-011(2)configurations. The ZPPR-010(12) one-region core consisted of Pu-U-Mo

alloy, sodium, and iron oxide plates with depleted U_3O_8 radial and axial blankets surrounded by steel reflectors.

The ZPPR-011(2) core had a cylindrical shape simulating a two-region configuration. It consisted of depleted U_3O_8, iron oxide, sodium, and Pu-U-Mo alloy plates with different fuel volume fractions in the inner and outer core regions. Axial and radial blankets made of depleted U_3O_8, depleted uranium metal, iron oxide, and sodium plates were also present, surrounded by a reflector of mild steel blocks loaded directly into the matrix tubes. In Fig. 3.7 the core configuration of ZPPR-11(2) is represented.

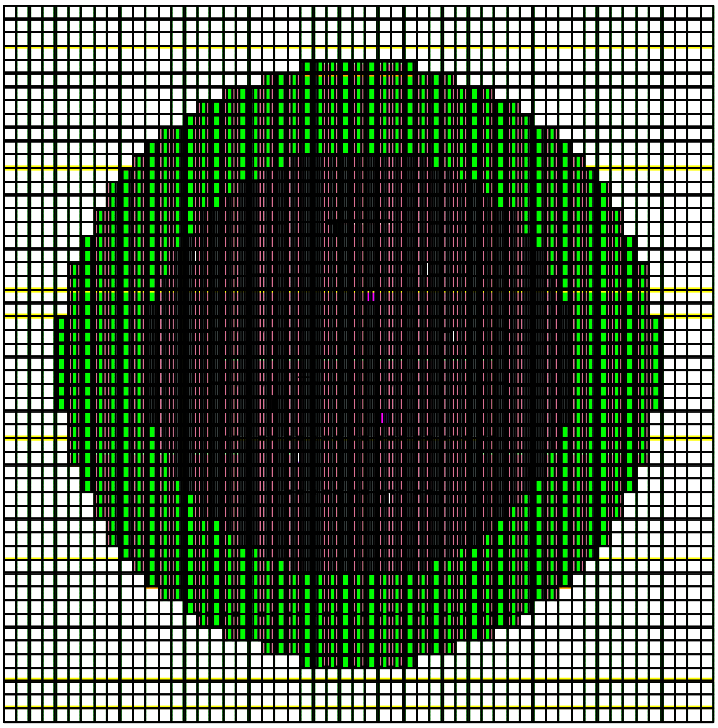

Figure 3.7: Core configuration of the ZPPR-2 experiment [55].

Other experiences on the ZPPR reactor were carried out in the framework of the JUPITER cooperative program, a joint research effort between Japan and the USA. Between 1978 and 1988, this initiative involved the construction of twenty-one zero-power experimental sodium-cooled cores for which various kinds of integral parameters were measured and evaluated as benchmarks.

Globally, experiments were divided into four series. The first one, named JUPITER-I (ZPPR-9 through ZPPR-10D/2), was a set of critical experiments simulating

cores of typical sodium-cooled commercial reactors of size between 600 and 800 MWe, with a two homogeneous zones configuration, thus including only MOX driver fuel assemblies in the active part of the core.

The following experimental campaign, designated JUPITER-II (ZPPR-13A through 13C), included six SFR core models with 650MWe of power, characterized by radial heterogeneity, and where different blanket regions were tested. The third phase of experiments, named JUPITER-III (ZPPR-17A through ZPPR-18C), comprised critical models simulating 650 MWe cores with enriched uranium used for the outer zones of the active regions. Finally, the JUPITER-IV series (ZPPR-19A through ZPPR-19B) consisted of five large models (representative of a 1000 MWe class SFR), making them the largest fast-spectrum critical configurations realized at that time.

3.2 Heuristic evaluation

The conclusions from the heuristic evaluation of the LMFR database, based on the criteria outlined in Section 3.1, are concisely presented for each facility in Table 3.1. To facilitate the identification of the experiments taken into account during the evaluation, Table 3.1 reports the IRPhE identification code in the first column, while the case label is provided in the second column. The short name version will be referred to from now on in this thesis. The third column indicates if the experiment has been chosen or not, and the final column is dedicated to the main reasons influencing each decision.

Table 3.1: Selection of the facilities with heuristic motivation

IRPhE Identification	Case label	Selected	Motivation
BFS1-LMFR-EXP-001	BFS-73-1	No	Expected low representativeness (metal uranium fuel and no control rods)
BFS1-LMFR-EXP-002	BFS-61-0	Yes	Expected good representativeness as one of the few configurations with lead in the core
BFS1-LMFR-EXP-002	BFS-61-1	Yes	Same considerations as for BFS-61-0

BFS1-LMFR-EXP-002	BFS-61-2	Yes	Same considerations as for the BFS-61-0 configuration, even if the blanket, instead of a lateral reflector, could affect spectrum hardness
BFS2-LMFR-EXP-001	BFS-63-3A	No	Low representativeness expected due to four core rings with different levels of enrichment and the reflector asymmetry
BR2-LMFR-RESR-001	BR2	No	Expected low representativeness: the core is small with respect to ALFRED, which could have a significant effect on the spectrum
EBR2-LMFR-RESR-001	EBR2	No	Low representativeness expected (metal uranium fuel, fuel is partially burnt, and the core is not symmetric)
FFTF-LMFR-RESR-001	FFTF	Yes	Good representativeness expected since MOX fuel is used, and it is one of the few power reactors (400 MWt)
JOYO-LMFR-RESR-001	JOYO 64	Yes	Sufficient representativeness expected (MOX pins with stainless steel cladding, and it is a power reactor)
JOYO-LMFR-RESR-001	JOYO 70	Yes	Same considerations as for JOYO 64
SNEAK-LMFR-EXP-001	SNEAK 7A	Yes	Sufficient representativeness expected (core is made of plates of MOX)
SNEAK-LMFR-EXP-001	SNEAK 7B	Yes	Sufficient representativeness expected (core is made of plates of MOX and depleted UO_2)

ZEBRA-LMFR-EXP-001	ZEBRA 22	No	Discarded for complying with the need of spreading measurements over different experiments so that pin-type configurations are preferred (see ZEBRA 23 and 25)
ZEBRA-LMFR-EXP-001	ZEBRA 23	Yes	Expected sufficient representativeness due to the MOX pins
ZEBRA-LMFR-EXP-001	ZEBRA 24	No	Same considerations as ZEBRA 22
ZEBRA-LMFR-EXP-001	ZEBRA 25	Yes	Expected sufficient representativeness due to the MOX pins
ZEBRA-LMFR-EXP-001	ZEBRA 11	No	Very complex geometry. Low representativeness expected due to metallic fuel in plates
ZEBRA-LMFR-EXP-001	ZEBRA 12	No	Same considerations as for ZEBRA 11
ZEBRA-LMFR-EXP-002	ZEBRA 12/4	No	Very complex geometry Considerations on representativeness shared with ZEBRA 11
ZEBRA-LMFR-EXP-002	ZEBRA 12/5	No	Same considerations as ZEBRA 12/4.
ZPR-LMFR-EXP-001	ZPR-6/7(1)	Yes	Good representativeness expected (fuel contains Pu and U, one region core)
ZPR-LMFR-EXP-002	ZPR-6/7(2)	Yes	Same considerations as ZPR-6/7(1) and ^{240}Pu enriched inner core zone
ZPR-LMFR-EXP-003	ZPR-3/48	No	Sufficient representativeness expected, but discarded for avoiding information duplication with configuration with ZPR-3/56B

ZPR-LMFR-EXP-003	ZPR-3/48B	Yes	Good representativeness expected (two regions core, symmetric configurations, fuel containing Pu and U)
ZPR-LMFR-EXP-004	ZPR-3/56B	Yes	Good representativeness expected (fuel cell composition, one region core)
ZPPR-LMFR-EXP-001	ZPPR-10A	Yes	High representativeness expected (two core regions like ALFRED, symmetric control rods, fuel cell compositions)
ZPPR-LMFR-EXP-002	ZPPR-9	Yes	Good representativeness expected due to the simple core map (divided into two regions) and fuel cell composition that simulates MOX fuels
ZPPR-LMFR-EXP-003	ZPPR-18A	No	Low representativeness expected due to asymmetry in the outer region core
ZPPR-LMFR-EXP-004	ZPPR-19B	No	Low representativeness expected (heterogeneous outer region core and core extremely large compared to ALFRED)
ZPPR-LMFR-EXP-005	ZPPR-10B	No	Discarded for the modeling effort required
ZPPR-LMFR-EXP-006	ZPPR-10C	No	Discarded for the modeling effort required
ZPPR-LMFR-EXP-007	ZPPR-13A	No	Low representativeness expected (complex and heterogeneous core with internal blankets)
ZPPR-LMFR-EXP-008	ZPPR-18C	No	Same considerations as ZPPR-18A

ZPPR-LMFR-EXP-009	ZPPR-7A	No	Low representativeness expected (complex and heterogeneous core with internal blankets)
ZPPR-LMFR-EXP-010	ZPPR-12	Yes	Good representativeness expected (fuel cells compositions, single core region, symmetric configuration)
ZPPR-LMFR-EXP-011	ZPPR-2	Yes	Good representativeness expected (two core regions, fuel cells compositions, and symmetric configuration)

After the selections from the LMFR facilities, MCNP criticality calculations were performed. Table 3.2 shows the percentage of neutrons giving fissions in thermal (< 0.625 eV), epithermal (0.625 eV - 100 keV), and fast (> 100 keV) energy ranges. The values are obtained from the simulations to confirm the fast spectrum characteristics expected from the heuristics evaluation and to compare them with the application case ALFRED.

3.3 Representativeness

To quantify the similarity between an experiment (E) and the reference application case (R), a correlation factor is used based on the nuclear data sensitivities and the nuclear data covariance matrix. This quantity is called the representativeness or representativity factor, $\boldsymbol{R}$, and it is defined as follows:

$$\boldsymbol{R}_{R,E}(Q) = \frac{S_{Q,E} COV_{\alpha\alpha} S_{Q,R}^T}{\sqrt{\left(S_{Q,R} COV_{\alpha\alpha} S_{Q,R}^T\right)\left(S_{Q,E} COV_{\alpha\alpha} S_{Q,E}^T\right)}} \tag{3.1}$$

where Q is the integral response with respect to which the representativeness between the two reactors (experimental maquette and reference) is compared - in this work, we are referring to the k_{eff}; $S_{Q,E}$ and $S_{Q,R}$ are the sensitivity vectors relative to the k_{eff} for the experimental facility E and the reference reactor R, respectively; $COV_{\alpha\alpha}$ is the covariance matrix which includes cross-section variances

Table 3.2: Selected cases from LMFR facilities of IRPhE Handbook - fission spectrum characteristics obtained from MCNP simulations

Case label	Thermal [%]	Epithermal [%]	Fast [%]
BFS-61-0	0.0	32.5	67.5
BFS-61-1	0.0	31.8	68.2
BFS-61-2	0.0	31.2	68.8
FFTF	0.0	40.6	59.4
JOYO 64	0.0	36.1	63.9
JOYO 70	0.0	35.4	64.6
SNEAK 7A	0.0	33.8	66.2
SNEAK 7B	0.0	32.6	67.4
ZEBRA 23	0.0	31.9	68.1
ZEBRA 25	0.0	26.4	73.6
ZPPR-10A: Loading 7	0.0	41.3	58.7
ZPPR-9: Loading 13	0.0	40.5	59.5
ZPPR-12: Loading 9	0.0	31.1	68.9
ZPPR-2: Loading 90	0.0	39.9	60.1
ZPR-6/7(1)	0.0	41.2	58.8
ZPR-6/7(2): Loading 99	0.0	40.6	59.4
ZPR-3/48B: Loading 6	0.0	34.3	65.7
ZPR-3/56B: Loading 17	0.0	40.8	59.2
ALFRED	0.0	40.7	59.3

and covariances for the isotopes that are present in both experimental and reference reactor. The closer the defined coefficient is to unity (in absolute value), the better the experimental facility reproduces the conditions of the reference reactor for the parameter under observation.

In this study, the computation of the representativeness has a twofold purpose: first, it allows for quantifying the similarity that up to this point, in first instance, was simply a qualitative evaluation; secondly, it is helpful for the implementation of the data assimilation tool presented in Chapter 2, where benchmark cases need to be introduced from the most similar to the least. As regards the second purpose, the correlation factor was calculated for all the experiments screened by the heuristic method, by considering two different sets of isotopes. The results are reported in Tables 3.3 and 3.4.

In Table 3.3, the covariance matrix and sensitivity vectors contain all thirteen

Table 3.3: Representativeness of the screened experiments to ALFRED (using 13 isotopes in common)

Experimental maquette	Representativeness
ZPR-6/7(2)	0.9784
ZPPR-2	0.9760
ZPR-6/7(1)	0.9749
ZPPR-10A	0.9741
ZPPR-9	0.9738
BFS-61-1	0.9581
ZEBRA-23	0.9557
FFTF	0.9555
BFS-61-0	0.9540
BFS-61-2	0.9525
ZPR-3/48B	0.9467
ZPR-3/56B	0.9436
ZPPR-12	0.9389
SNEAK-7B	0.9380
ZEBRA-25	0.9267
SNEAK-7A	0.8863
JOYO 70	0.6258
JOYO 64	0.6139

isotopes that are in common for each of the modeled experiments. In contrast, in Table 3.4, only the five actinides present among the materials of all the calculated benchmark cases were included. The mentioned actinides are ^{235}U,^{238}U, ^{239}Pu, ^{240}Pu and ^{241}Pu. Since these isotopes are the main contributors to the uncertainty due to the nuclear data, this approach was meant to investigate any differences in using a restricted (but meaningful) set of isotopes regarding the representativeness ranking and to evaluate any impact on the data assimilation outputs.

Finally, it is worth noting that the representativeness coefficients obtained are in general good agreement with the representativeness calculated in similar studies [97]. In the cited work, the sensitivity coefficients are computed with the deterministic code ERANOS using the same library (ENDF/B-VIII.0), and the reference reactor is the same (ALFRED).

Table 3.4: Representativeness of the screened experiments to ALFRED (using 5 actinides)

Experimental maquette	Representativeness
ZPPR-2	0.9771
ZPR-6/7(1)	0.9758
ZPPR-9	0.9751
ZPPR-10A	0.9750
ZPR-3/56B	0.9648
FFTF	0.9630
BFS-61-1	0.9614
BFS-61-0	0.9575
ZEBRA-23	0.9572
BFS-61-2	0.9559
ZPR-3/48B	0.9503
ZPR-6/7(2)	0.9503
ZPPR-12	0.9418
SNEAK-7B	0.9415
ZEBRA-25	0.9279
SNEAK-7A	0.8934
JOYO 70	0.6271
JOYO 64	0.6159

3.4 Reactivity coefficients and effects

In the IRPhE handbook, reactivity coefficients, namely temperature and burnup, and reactivity effects, which comprise control rod, sodium voiding, fuel worth, and other material samples measurements, are collected into two different sections (respectively, COEF and REACT). However, both categories significantly contribute to the experiments available for evaluating the accuracy of the neutronics code in predicting the reactivity behavior due to these phenomena. In the following paragraphs, the three parameters computed and analyzed in this study are presented.

Control Rod Worth

There are around 50 control rod worth measurements taken from nine different facilities. While benchmarks for control rods are not commonly used for nuclear data verification and adjustment, they are crucial to confirm the ability of codes to predict the effectiveness of these fundamental safety systems. FFTF, JOYO, ZPPR, and ZPR reported control rod worth experiments with uncertainties between 1% and 5%. In this work, only a restricted selection of these cases was

simulated, trying to favor different insertion configurations and conditions while minimizing the modeling effort required.

Coolant Void

On the other hand, coolant void benchmarks are paramount for nuclear data validation and reactivity effects accuracy evaluation. The only coolant for which benchmarks are present in IRPhE is sodium. The handbook reports 16 sodium void reactivity measurements made in 4 different facilities. Sodium void measurements are often used for nuclear data adjustment of sodium and plutonium cross sections, especially for SFR applications [98, 99, 100]. Tab. 3.5 summarizes the LMFR cases of interest. As well as for the control rods, a smaller number of experiments were reproduced compared to the total availability.

A pertinent question that may arise from the decision to incorporate these experiments into the validation efforts for LFRs is the rationale behind including sodium voiding effects in this research.

In the absence of dedicated experimental benchmark data for the coolant void reactivity coefficient in LFR, given the physical analogies between the two systems, using void coefficient experiments from SFR could be the only available choice to not neglect a key phenomenon of paramount safety relevance [64]. In fact, both SFRs and LFRs operate in a fast neutron spectrum and employ a liquid-metal coolant, thus sharing several neutronic feedback mechanisms, including those depending on coolant density changes [101].

But the lack of alternatives is not the only reason. Analyzing in more depth the phenomenon from a physical standpoint, coolant voiding involves the superpositions of three effects:

- reduction of captures in the coolant by coolant removal (positive effect in reactivity, very much coolant-dependent);
- increase in fissions in the fuel by spectrum hardening following the lack of slowing down in the coolant (positive effect in reactivity, pretty less coolant-dependent);
- increase of leakage from the core by overall increase of the neutrons mean free path (negative effect in reactivity, pretty less coolant-dependent).

While the first effect depends on the coolant, and its contribution to the representativeness of experiments with sodium against ALFRED would be minimal, the two other effects could still be well captured in the available experiments, that therefore could provide - to the extent allowed by the geometrical core configurations of the available experimental maquettes - potentially meaningful insights into

the code capability to reproduce the experimental results, and possibly transpose them to the LFR applicability domain.

Table 3.5: Coolant void reactivity benchmarks in the IRPhE handbook.

Facility	Material	Uncertainty
BFS2	Sodium	$\sim 10\%$
JOYO	Sodium	$\sim 30\%$
ZEBRA	Sodium	$\sim 5\%$
ZPPR	Sodium	$\sim 5\%$
ZPR	Sodium	$\sim 10\%$

Temperature Reactivity
For the isothermal temperature coefficient (ITC), approximately 50 measurements from eight facilities are available. Unfortunately, only two of them are among LMFRs: FFTF and JOYO. Both the system responses to changes are for increases in the total system temperature. For FFTF the temperature range is ± 30 K with $\sim 2\%$ of uncertainty, while for JOYO the experimental difference is 80 K with $\sim 5\%$ uncertainty.

3.5 Other parameters

As explained in Section 2.4.2, for eigenvalue problems, MCNP does not have the capability to compute sensitivity coefficients relative to reaction rates or spectral indices. However, to complete the description of the cases available in the IRPhE database, these reactor physics fundamental parameters are briefly described below. The purpose is to provide the reader with a comprehensive record of the available measurements that might be of interest for future evaluations, such as comparisons in terms of C/E ratios or for neutronics codes that can compute sensitivities for different quantities as well.

Kinetics Parameters
Since they influence the reactor transient response, kinetic parameters are crucial for assessing the safety of nuclear reactors. The fraction of delayed neutrons and their time constants are frequently integrated into the analysis of various experimental outcomes, where understanding these kinetic parameters helps to separate the measured signals into reactivity. Benchmarking of the β_{eff} is sometimes conducted; however, additional efforts are needed to clarify the uncertainties present in the data.

Among the LMFR section, there are only two available measurements of the delayed neutron fraction. The facilities that measured the β_{eff} are BFS2 and SNEAK, with 2% and 5% of experimental uncertainty, respectively. Over the IRPhE database, the number of cases valid as benchmarks increases up to eight.

Reation Rate and Power Distributions
Reaction rate measurements play a fundamental role in the characterization and validation of reactor physics models. Several types of experiments contribute to this objective, including flux mapping, fission chamber scans, and both fine- and macro-structure wire activation analyses. These experiments are essential for accurately characterizing the spatial distribution of the neutron flux and serve as a key reference for validating nuclear data and computational codes. Their relevance is particularly pronounced near material interfaces — such as within the core region or close to structural components, where flux gradients and spectral effects are more significant. Furthermore, fine-structure measurements of reaction rates and power distributions within reactor fuel provide valuable benchmarks for assessing fuel performance models.

The LMFR facilities that reported benchmarked values are: BFS, SNEAK, ZEBRA, ZPPR, and ZPR. An overview of the available datasets, covering both reaction rates and spectral indices, is summarized in Table 3.6. To illustrate the type of analysis that can be performed with a neutronics code, Figures 3.8 and 3.9 present an example of the radial distribution of normalized reaction rates from the SNEAK-7B configuration, as calculated with MCNP, the reference code employed in this study. In particular, Figure 3.9 presents the calculated-to-experimental trends for the f28 (fissons of ^{238}U), f49 (fissions of ^{239}Pu), and c28 (captures of ^{238}U) reaction rates, highlighting a systematic overestimation by the code at specific positions. Overall, the calculations reproduce the experimental distributions well; however, as the distance from the reactor core increases, the absolute reaction rates decrease, and the predictive accuracy correspondingly diminishes. However, these results cannot be further utilized in this work due to the previously mentioned computational limit of MCNP in calculating sensitivity profiles.

Spectral indices
Reactor systems are usually compared based on their neutron spectrum, which is not easy to measure experimentally, and even less trivial to quantitatively manage in a study like the present, due to the manifold data needed to correctly represent the information. Spectral characteristics can instead permit comparisons and studies, which are more relevant the more these characteristics are well represented by single parameters. Among those, spectral indices - representing the ratio of reaction rates - are a very good means for quantitative comparisons: if the reaction rates to relate are properly chosen so that their ratio can well provide a proxy for

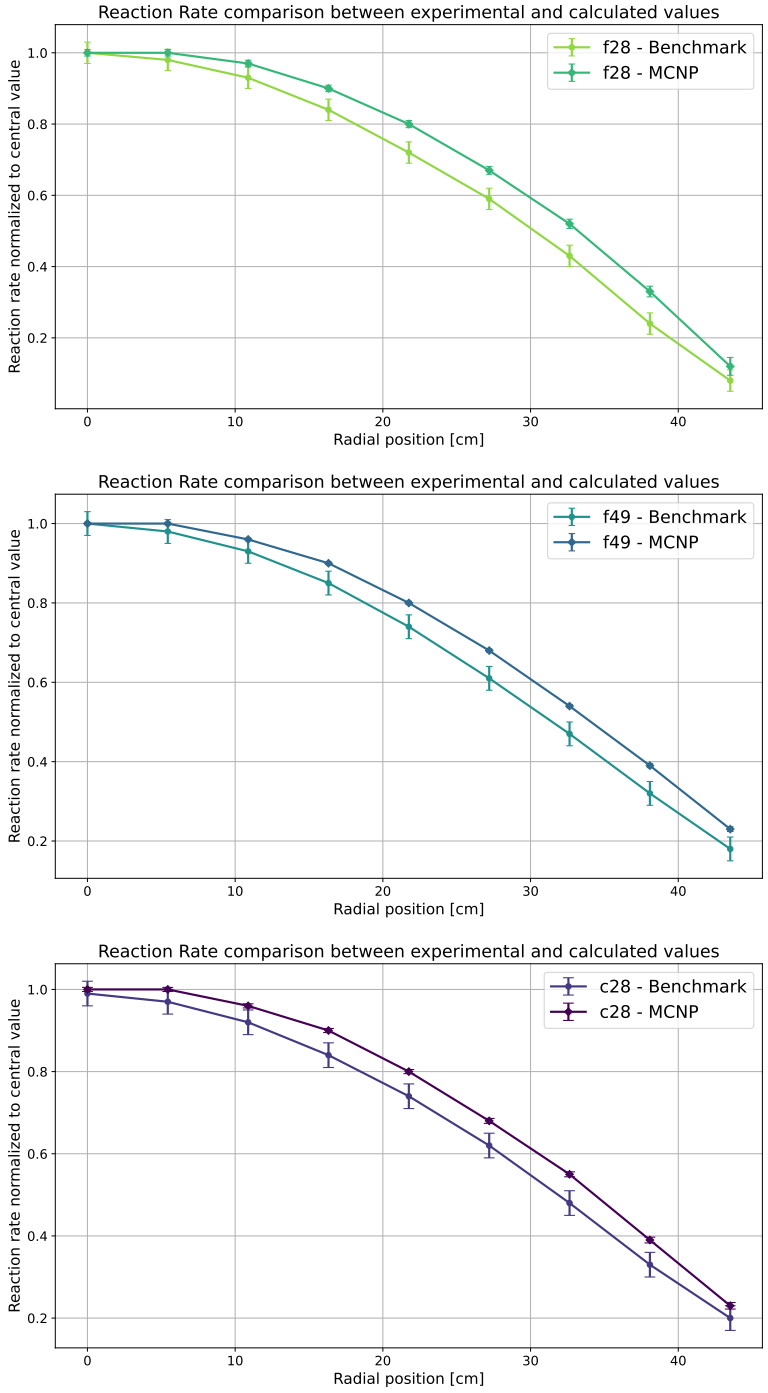

Figure 3.8: Reaction rates for SNEAK-7B, radial distribution from the core center

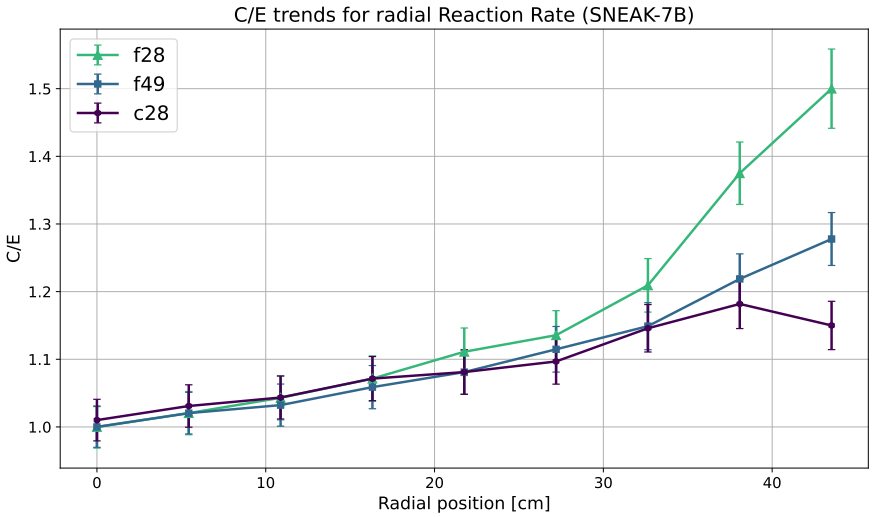

Figure 3.9: Radial reaction rates C/E trend of measurements in SNEAK-7B

the neutron spectrum, spectral indices can be very effectively used, also thanks to the possibility for their direct measurement with different techniques (the most common of which being activation foils) at different positions.

The IRPhE handbook reports 233 spectral characteristics measurements performed among 15 facilities. Most of the measurements are reaction rates relative to either f49 (^{239}Pu fission) or f25 (^{235}U fission). Specific reaction rate measurements are presented in Tab. 3.6.

Burnup

In the whole reactor physics handbook, only two cases exist for burnup reactivity, one of which is for the JOYO 70 configuration. The measurements are taken compared to the control rod Worth, and the typical uncertainty is $\sim 3\%$.

Table 3.6: Spectral characteristic experimental benchmarks in the IRPhE handbook.

Facility	**Spectral index**	**Reaction Rate**	**Uncertainty**
BFS	f51/f49, f53/f49, c37/f49, f37/f49, f49/f25, c28/f49, f28/f25, f40/f49, f41/f49, f42/f25, f23/f25, f64/f49, f48/f49, c28/f25	f25, f28, f49	∼3%
SNEAK	f49/f25, f28/f25, c28/f25	c28, f28, f49	∼3%
ZPPR	c28/f49, f28/f25, c28/f25	f28, c28, f28, f49	∼3%
ZPR	c28/f49, f28/f25, c28/f25, c28/f28	f28, c28, f28, f49	∼3%

Legend: f=fission, c=capture,
23=^{233}U, 25=^{235}U, 28=^{238}U, 37=^{237}Np,
40=^{240}Pu, 41=^{241}Pu, 42=^{242}Pu, 48=^{238}Pu, 49=^{239}Pu
51=^{241}Am, 53=^{243}Am, 64=^{244}Cm.

Chapter 4

Results and Discussion

This chapter presents and discusses the main results obtained from the analysis of the benchmark calculations and associated uncertainty quantification. The comparison between calculated and experimental values, expressed as the calculation-over-experiment (C/E) ratio, is first carried out for the effective neutron multiplication factor, providing an assessment of the uncertainties. Subsequently, the results obtained for the reactivity effects control rod worth (CRW), sodium void reactivity (SVR), and isothermal temperature coefficient (ITC) are discussed. Then, Section 4.5 will provide an overview of the accuracy of the MCNP calculations for the different parameters taken into account. Finally, the Generalized Linear Least Squares approach is presented.

The uncertainties considered here are:

- **Experimental uncertainty** σ_E: it is the uncertainty associated with the benchmark cases reported in IRPhE.
- **Statistical uncertainty** $\sigma_{\mathbf{stat}}$: the standard deviation of the Monte Carlo simulations.
- **Nuclear Data uncertainty** σ_{ND}: it is the one calculated with the sandwich rule with the given covariance matrix and the sensitivity coefficients calculated with MCNP.

The total uncertainty of the C/E ratios is calculated as follows:

$$\sigma_{\frac{C}{E}} = \frac{C}{E}\sqrt{\left(\frac{\sigma_C}{C}\right)^2 + \left(\frac{\sigma_E}{E}\right)^2}, \tag{4.1}$$

where σ_C, the uncertainty associated with the calculation, is expressed as:

$$\sigma_C = \sqrt{\sigma_{stat}^2 + \sigma_{ND}^2}, \tag{4.2}$$

given the independence between the two sources of uncertainties.

4.1 Effective multiplication factor

The results of the C/E analysis for k_{eff} are summarized in Table 4.1 and visually represented in Figure 4.1. The C/E values range from approximately 0.994 to 1.011, indicating a strong agreement between calculated and experimental results, with the majority of benchmarks showing the absolute deviation of the calculated-to-experiment ratio ($C/E - 1$) values well below 1%. Figure 4.1 highlights that the computational set-up tends to underestimate the benchmark value: for 83.3% of the cases C/E is below 1, while the other 16.7% (three cases) are above 1.

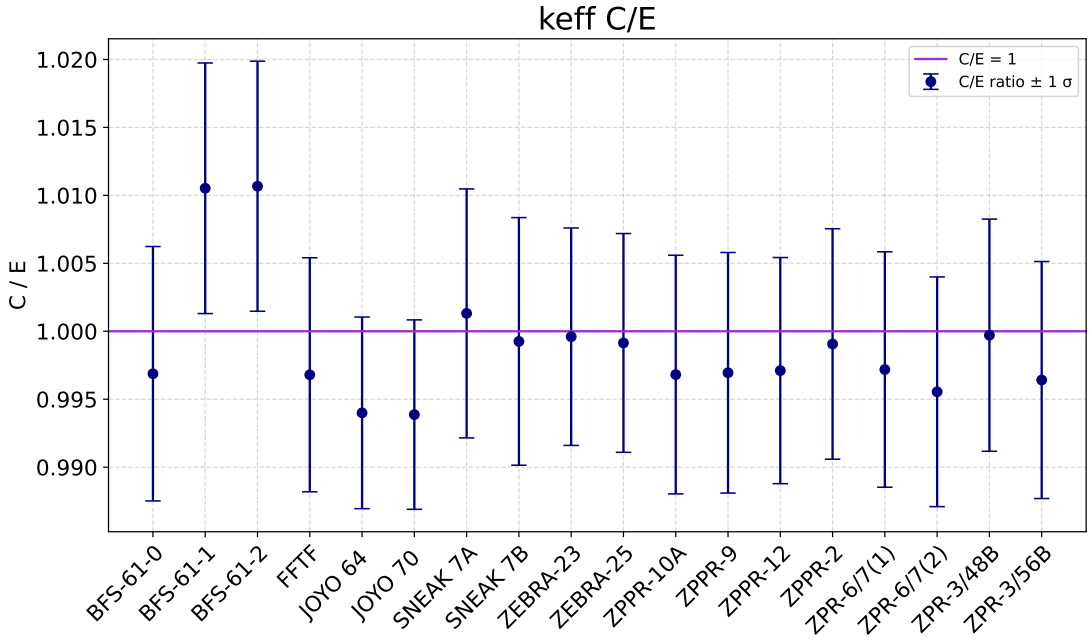

Figure 4.1: C/E values for k_{eff}

The total uncertainties, expressed both in pcm and in percentage, are relatively consistent across all benchmarks, ranging from 700 to 940 pcm. When compared to these uncertainties, most deviations fall within the margins of error, confirming that the observed differences are statistically acceptable. As shown in Figure 4.2,

Table 4.1: k_{eff} results: C/E and total uncertainties

Case label	C/E	C/E-1 [%]	Uncertainty (total) [pcm]	Uncertainty (total) [%]
BFS-61-0	0.99688	-0.31	936	0.94
BFS-61-1	1.01052	1.05	922	0.91
BFS-61-2	1.01067	1.07	920	0.91
FFTF	0.99680	-0.32	861	0.86
JOYO 64	0.99400	-0.60	705	0.71
JOYO 70	0.99387	-0.61	697	0.70
SNEAK 7A	1.00131	0.13	916	0.91
SNEAK 7B	0.99925	-0.07	911	0.91
ZEBRA 23	0.99960	-0.04	800	0.80
ZEBRA 25	0.99914	-0.09	805	0.81
ZPPR-10A	0.99681	-0.32	878	0.88
ZPPR-9	0.99695	-0.31	885	0.89
ZPPR-12	0.99711	-0.29	832	0.83
ZPPR-2	0.99906	-0.09	848	0.85
ZPR-6/7(1)	0.99719	-0.28	866	0.87
ZPR-6/7(2)	0.99555	-0.45	845	0.85
ZPR-3/48B	0.99971	-0.03	854	0.85
ZPR-3/56B	0.99641	-0.36	872	0.88

$C/E - 1$ values for k_{eff} are compared with the corresponding total uncertainty for each experimental case. The dark blue bars represent the magnitude of the deviation, while the light blue bars indicate the total uncertainty associated with each calculation.

Overall, the results reveal that for sixteen out of eighteen benchmarks, the deviations remain within the estimated uncertainty margins, suggesting a generally good consistency between calculated and experimental values. However, a few benchmarks, BFS-61-1 and BFS-61-2 specifically, exhibit significantly larger discrepancies, with absolute $C/E - 1$ values exceeding 1000 pcm. These deviations may indicate possible modeling approximations or nuclear data issues specific to these configurations. Nevertheless, in the IRPhE Handbook [55], previous calculations with MCNP5 and older ENDF/B libraries could suggest that the nuclear data could strongly affect the accuracy of the results. For example, when simulating the same model using ENDF/B-VII.0, the $C/E - 1$ is around 920 pcm, while for ENDF/B-VI.6, the absolute $C/E - 1$ is much closer ($\sim$100 pcm).

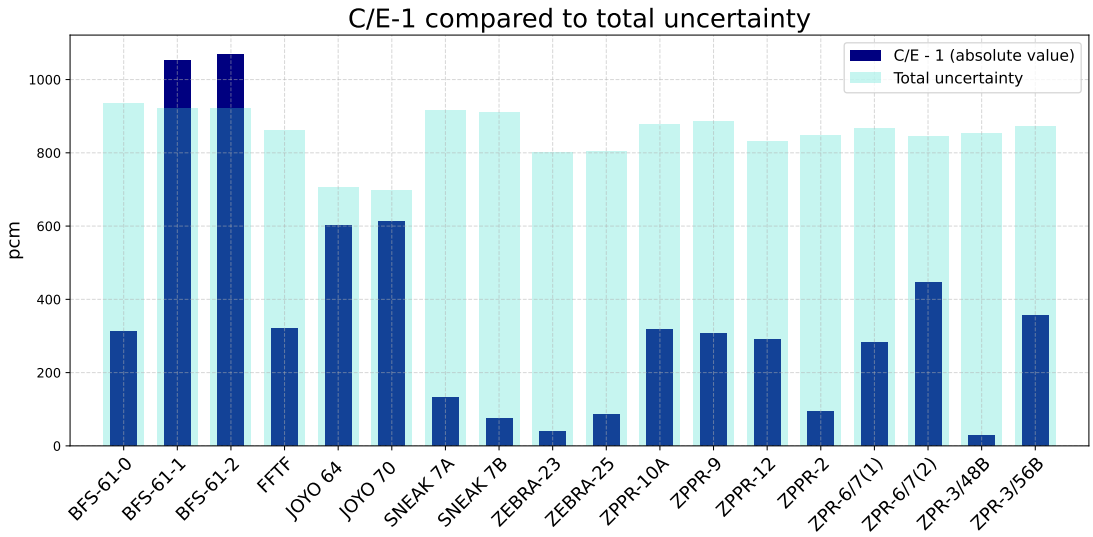

Figure 4.2: k_{eff} results: total uncertainty

Table 4.2 and Figure 4.3 present the decomposition of the total k_{eff} uncertainty into its three main components: experimental, statistical, and nuclear data contributions. The results clearly indicate that the nuclear data uncertainty is the dominant source across all benchmark cases, typically ranging between 670 and 890 pcm. This component accounts for the vast majority of the total uncertainty observed in the previous analyses, confirming that the precision of nuclear data plays a critical role in determining the overall accuracy of the k_{eff} predictions. The experimental uncertainty is considerably smaller, generally between 70 and 400 pcm, depending on the benchmark. The statistical uncertainty is consistently below 20 pcm and negligible in comparison to the other sources of uncertainties (it was excluded from Figure 4.3 indeed), demonstrating excellent convergence and computational robustness in all cases.

Table 4.2: k_{eff} results: uncertainties divided by source (absolute value)

Case label	Experimental Uncertainty [pcm]	Statistical Uncertainty [pcm]	Nuclear Data Uncertainty [pcm]
BFS-61-0	290	6	891
BFS-61-1	290	5	874
BFS-61-2	290	6	872
FFTF	210	5	835
JOYO 64	180	3	682
JOYO 70	180	4	672
SNEAK 7A	350	19	847
SNEAK 7B	400	2	821
ZEBRA 23	127	5	791
ZEBRA 25	131	5	795
ZPPR-10A	150	5	866
ZPPR-9	154	4	873
ZPPR-12	80	5	829
ZPPR-2	70	5	846
ZPR-6/7(1)	87	5	862
ZPR-6/7(2)	90	5	841
ZPR-3/48B	120	4	831
ZPR-3/56B	150	4	853

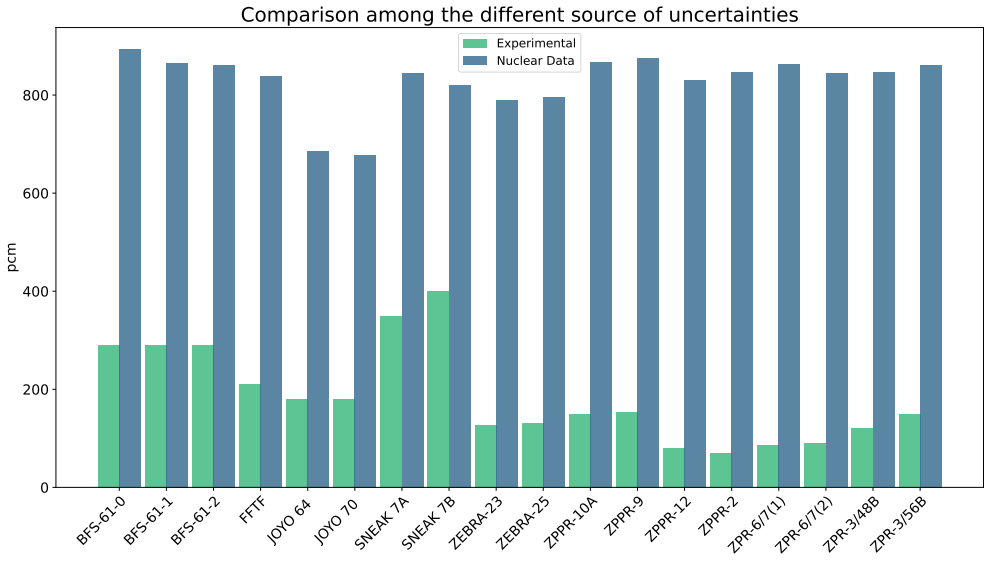

Figure 4.3: k_{eff} results: nuclear data uncertainty and experimental uncertainty

4.2 Control rod worth

The analysis of the control rod worth (CRW) results reveals a generally good consistency between the calculated and experimental values across the benchmark facilities and configurations, JOYO, FFTF, ZPPR-9, and ZPPR-10A. As shown in Table 4.3, the calculation-over-experiment ratios mostly range between 0.95 and 1.05, indicating that the Monte Carlo simulations performed with MCNP reproduce the measured values within a few percent. This level of agreement is satisfactory, suggesting that the adopted nuclear data and modeling assumptions are adequate for CRW estimation across different reactor configurations.

In Figure 4.4, trends can be detected when observing the facility taken into account. The following bullet points summarize the findings.

- **FFTF cases**: the C/E values all score below unity, with a spread (0.93–0.98) systematically larger compared to the other cases, with deviations up to 7%, and total uncertainties ranging from ∼6% to 10%. This is also due to the experimental uncertainty contribution, which is predominant in the propagation of the total uncertainty.
- **JOYO cases**: the C/E ratios are also all slightly below unity (0.96–0.99), suggesting a moderate underprediction of the control rod worths by the simulations. The associated total uncertainties are between 3 and 4.5%, dominated by experimental and nuclear data components, while statistical uncertainties are negligible.
- **ZPPR-9 and ZPPR-10A cases**: benchmarks from both configurations, which overall exhibit the best agreement, tend to overestimate the measured CRW. All C/E ratios are above unity (1.01–1.05) and bring low total uncertainties (2–3%), confirming the good performance of the computational framework.

Table 4.3: Control Rod Worth C/E results

Facility	**Experiment**	**C/E**	**C/E-1 [%]**	**Total Unc. [$]**	**Total Unc. [%]**
FFTF	State 1 - case 1	0.979	-2.08	0.061	6.21
FFTF	State 1 - case 2	0.954	-4.60	0.057	5.94
FFTF	State 1 - case 3	0.959	-4.15	0.063	6.55
FFTF	State 1 - case 4	0.928	-7.18	0.064	6.89
FFTF	State 1 - case 5	0.960	-3.96	0.096	10.02
FFTF	State 1 - case 6	0.968	-3.15	0.057	5.86
FFTF	State 1 - case 7	0.966	-3.35	0.056	5.80
FFTF	State 1 - case 8	0.956	-4.40	0.057	5.97
FFTF	State 1 - case 9	0.966	-3.40	0.054	5.64
FFTF	State 1 - case 10	0.947	-5.33	0.055	5.78
FFTF	State 1 - case 11	0.975	-2.51	0.058	5.96
JOYO	RR1	0.990	-1.05	0.032	3.22
JOYO	RR2	0.975	-2.52	0.036	3.73
JOYO	SR1	0.962	-3.79	0.043	4.52
JOYO	SR2	0.973	-2.72	0.033	3.38
JOYO	SR3	0.988	-1.22	0.045	4.56
JOYO	SR4	0.979	-2.09	0.035	3.57
ZPPR9	Loading 80	1.023	2.30	0.036	3.47
ZPPR9	Loading 86	1.021	2.10	0.016	1.60
ZPPR9	Loading 94	1.015	1.55	0.023	2.26
ZPPR9	Loading 100	1.030	2.96	0.023	2.22
ZPPR9	Loading 118	1.030	3.01	0.029	2.84
ZPPR10A	Loading 13	1.053	5.26	0.042	4.00
ZPPR10A	Loading 15	1.053	5.30	0.021	1.98
ZPPR10A	Loading 26	1.029	2.93	0.019	1.87
ZPPR10A	Loading 29	1.037	3.69	0.019	1.84

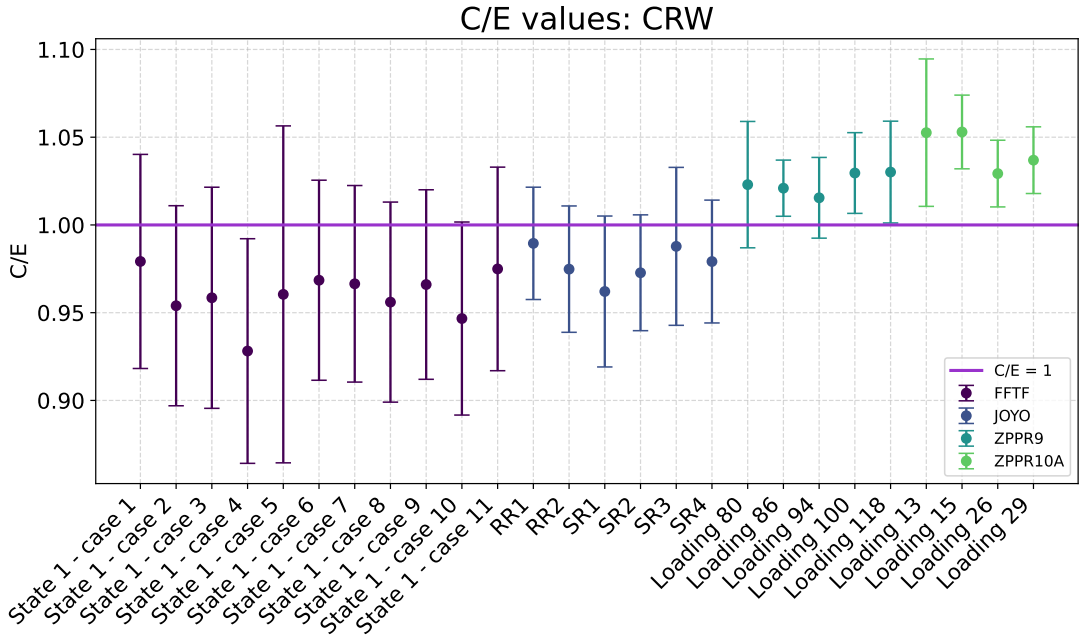

Figure 4.4: C/E values for CRW

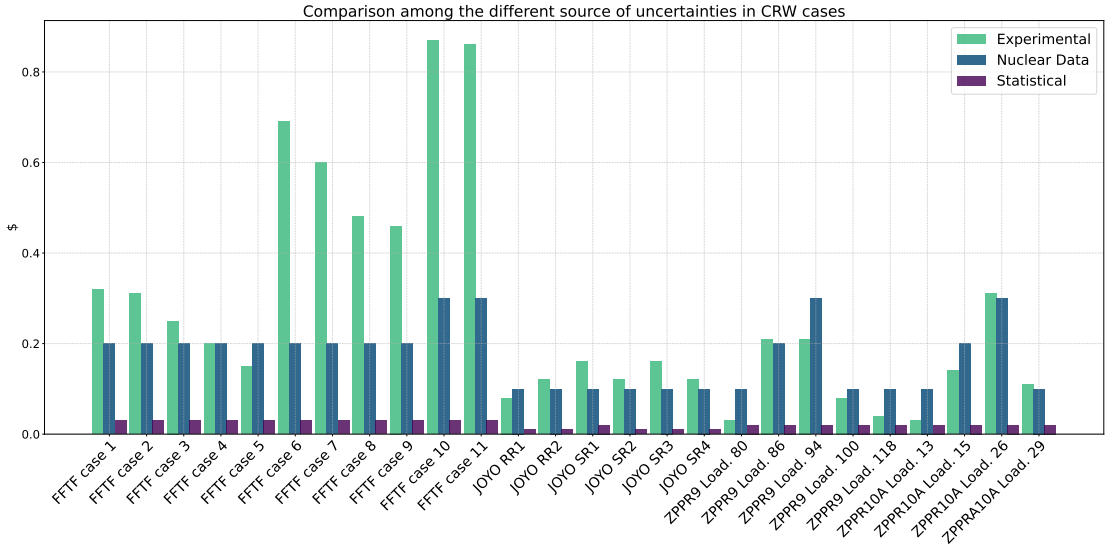

Figure 4.5: Sources of uncertainty of CRW cases

Figure 4.5 and Table 4.4 show that experimental and nuclear data uncertainties are the principal contributors to the total uncertainty, whereas the statistical component from the Monte Carlo simulations remains negligible in all cases (typically below 0.03 \$). For JOYO and ZPPR cases, experimental and nuclear data uncertainties are comparable (0.06–0.16 \$ each), whereas for FFTF cases, experimental uncertainties dominate, often surpassing 0.5\$. This pattern might reflect the more complex experimental setups and measurement challenges in large-scale fast reactors. Compared to k_{eff} results (see Figure 4.3), where the nuclear data uncertainty was $3 \div 4$ times higher than experimental ones, these results emphasize the crucial role of accurate experimental measurements when comparisons with benchmark cases are needed for code validation.

To conclude, the total uncertainty on the C/E ratios remains between 3% and 10%, depending on the facility, with FFTF showing the highest relative uncertainties. Despite the observed biases, the majority of calculated values lie within one standard deviation of the experimental data, confirming the reliability of the computational approach and the underlying nuclear data library. The balanced trend, where underestimations in two facilities (FFTF, JOYO, which account for 65.4% of the CRW results), is offset by overestimations in others (ZPPR9, ZPPR10A), suggests that there is no systematic bias in the evaluation of CRW, demonstrating consistent model performance across multiple facilities, with systematic deviations that, with one exception, remain within about $\pm 5\%$.

Table 4.4: Control Rod Worth error sources

Facility	**Experiment**	**Experimental Unc. [$]**	**Statistical Unc. [$]**	**Nuclear Data Unc. [$]**
FFTF	State 1 - case 1	0.32	0.03	0.19
FFTF	State 1 - case 2	0.31	0.03	0.15
FFTF	State 1 - case 3	0.25	0.03	0.16
FFTF	State 1 - case 4	0.20	0.03	0.16
FFTF	State 1 - case 5	0.15	0.03	0.24
FFTF	State 1 - case 6	0.69	0.03	0.23
FFTF	State 1 - case 7	0.60	0.03	0.21
FFTF	State 1 - case 8	0.48	0.03	0.23
FFTF	State 1 - case 9	0.46	0.03	0.18
FFTF	State 1 - case 10	0.87	0.03	0.27
FFTF	State 1 - case 11	0.86	0.03	0.28
JOYO	RR1	0.08	0.01	0.09
JOYO	RR2	0.12	0.01	0.07
JOYO	SR1	0.16	0.02	0.08
JOYO	SR2	0.12	0.01	0.06
JOYO	SR3	0.16	0.01	0.08
JOYO	SR4	0.12	0.01	0.07
ZPPR9	Loading 80	0.03	0.02	0.09
ZPPR9	Loading 86	0.21	0.02	0.19
ZPPR9	Loading 94	0.21	0.02	0.33
ZPPR9	Loading 100	0.08	0.02	0.12
ZPPR9	Loading 118	0.04	0.02	0.09
ZPPR10A	Loading 13	0.03	0.02	0.10
ZPPR10A	Loading 15	0.14	0.02	0.23
ZPPR10A	Loading 26	0.31	0.02	0.26
ZPPR10A	Loading 29	0.11	0.02	0.14

4.3 Sodium void reactivity

From Table 4.5 and Figure 4.6, the results of the sodium void reactivity (SVR) can be analyzed. The results present a wider dispersion of C/E ratios compared to the CRW cases, indicating higher sensitivity of the sodium void effect to modeling assumptions and nuclear data uncertainties. The C/E ratios across all benchmark facilities range between approximately 0.84 and 1.41, reflecting both underestimations and overestimations of experimental results depending on the core configuration, even though specific trends are not clearly detectable when observing the cases belonging to a single facility. Out of nineteen benchmarks, eleven cases, or 57.9%, show a C/E ratio above 1. This indicates that there is no significant tendency to overestimate the experimental value. Despite the significant spread, however, all experimental values fall within the total uncertainty ranges of the corresponding calculations. While a general concern can be raised on the simulation accuracy, from both the lack of a systematic trend and the significant dispersion of the results, no explicit issue on model accuracy can be deduced at this stage.

Table 4.5: Sodium Void Reactivity C/E results

Facility	**Experiment**	**C/E**	**C/E-1 [%]**	**Total Unc. [%]**
JOYO	Center	1.103	0.1	38.8
JOYO	1F1	0.882	-0.1	36.6
JOYO	2F1	1.209	0.2	32.3
JOYO	3F1	1.412	0.4	35.9
JOYO	4F1	0.841	-0.2	48.9
ZPPR9	Loading 37	0.881	-0.1	32.1
ZPPR9	Loading 38	1.020	0.0	39.4
ZPPR9	Loading 39	0.925	-0.1	47.8
ZPPR10A	Loading 33	0.969	0.0	56.7
ZPPR10A	Loading 34	1.072	0.1	37.3
ZPPR10A	Loading 37	1.023	0.0	25.3
ZPPR10A	Loading 40	1.003	0.0	27.8
ZPPR2	Loading 181	1.183	0.2	61.9
ZPPR2	Loading 183	1.246	0.2	22.2
ZPPR2	Loading 184	1.103	0.1	22.8
ZPPR2	Loading 185	1.172	0.2	14.0
ZPPR12	Loading 30	0.924	-0.1	11.6
ZPPR12	Loading 33	0.899	-0.1	10.3
ZPPR12	Loading 37	0.934	-0.1	8.5

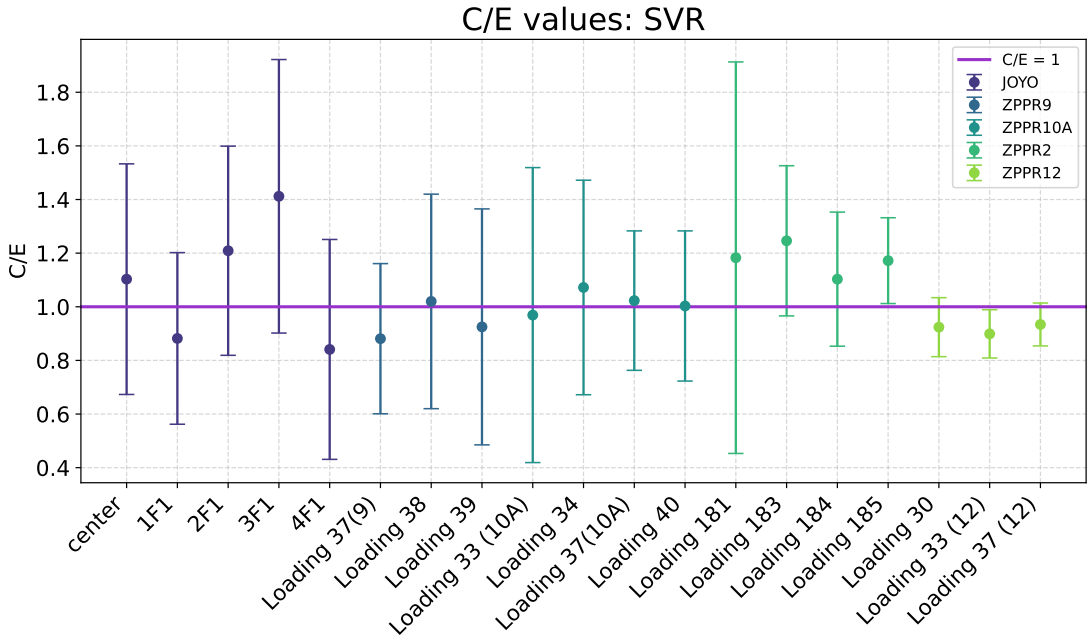

Figure 4.6: C/E values for SVR cases

For the JOYO benchmarks, the results show strong discrepancies: both C/E ratio outliers are among these experiments, corresponding to deviations up to -20% and +40%. These differences highlight the challenges in accurately predicting void effects when the experimental quantities are very small to be detected. As evidently represented in Figure 4.7, JOYO SVR cases are the only ones in which the statistical uncertainty has a substantial contribution to the overall uncertainty. It has the same order of magnitude as the experimental uncertainties ($\sim 30\%$), while nuclear data components are reduced as it could also be observed from Table 4.6. This effect may be because the k_{eff} values of the simulations are very close to each other, consistently with the small difference between the corresponding reference and the perturbed cases. Moreover, considering a typical standard deviation of 6 $\div$ 7 pcm with the MCNP runs for JOYO models, when the uncertainties are propagated with respect to the reactivity coefficient, we obtain a value that is higher than the other cases encountered. This pattern is confirmed across other experiments: the ZPPR-9 configurations present an average statistical uncertainty of 4 pcm against a difference between nominal and perturbed cases of 100 pcm, while in ZPPR-10A the k_{eff} variations range from 70–200 pcm with 4 pcm of statistical uncertainty. Similar trends are observed for ZPPR-2 experiments, and the statistical contributions remain limited also in ZPPR-12 cases, where the sodium void reactivity effect is substantially larger (575–1200 pcm) compared to the Monte

Carlo statistical error (6 pcm).

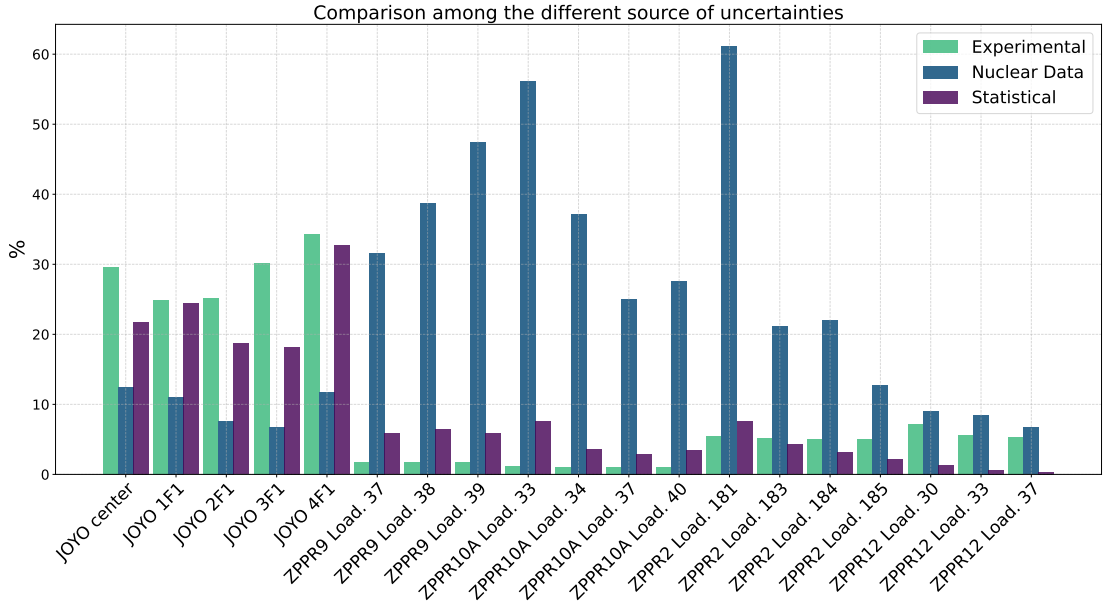

Figure 4.7: Sources of uncertainty of SVR cases

The ZPPR-9 and ZPPR-10A cases show overall better consistency, with C/E ratios close to unity (0.88–1.07) and total uncertainties between 25–55%. Although the mean spread is reduced, the uncertainty (and its variability) remains significant, driven mainly by nuclear data uncertainties, which reach up to 56% for some configurations.

The ZPPR-2 experiments present higher C/E values (1.10–1.25) accompanied by large uncertainties (14–62%) dominated by nuclear data. Conversely, the ZPPR12 results show excellent consistency, with C/E ratios between 0.90 and 0.93 and comparatively low total uncertainties (8–12%), the nuclear data component of which is comparable to other sources (notably, the experimental one). This suggests that the underlying models and nuclear data produce reliable predictions for these configurations, possibly due to their simpler voiding patterns and better-characterized experimental conditions.

Observing the breakdown of uncertainty sources in Figure 4.7 underscores that nuclear data uncertainties dominate for most ZPPR configurations. At the same time, as already mentioned, experimental and statistical components are more relevant in the JOYO cases. The large spread of total uncertainties across facilities reflects differences in benchmark characterization and sensitivity to nuclear data. The significant total uncertainties observed, particularly in some JOYO and

Table 4.6: Sodium Void Reactivity error sources

Facility	Experiment	Experimental Unc. [%]	Statistical Unc. [%]	Nuclear Data Unc. [%]
JOYO	Center	29.6	21.8	12.4
JOYO	1F1	24.9	24.4	11.1
JOYO	2F1	25.2	18.7	7.6
JOYO	3F1	30.2	18.2	6.7
JOYO	4F1	34.4	32.7	11.8
ZPPR9	Loading 37	1.7	5.8	31.6
ZPPR9	Loading 38	1.7	6.5	38.8
ZPPR9	Loading 39	1.7	6.0	47.4
ZPPR10A	Loading 33	1.2	7.6	56.2
ZPPR10A	Loading 34	1.1	3.6	37.1
ZPPR10A	Loading 37	1.1	2.9	25.1
ZPPR10A	Loading 40	1.1	3.4	27.6
ZPPR2	Loading 181	5.4	7.5	61.2
ZPPR2	Loading 183	5.1	4.3	21.2
ZPPR2	Loading 184	5.1	3.1	22.0
ZPPR2	Loading 185	5.0	2.2	12.8
ZPPR12	Loading 30	7.1	1.3	9.1
ZPPR12	Loading 33	5.6	0.7	8.5
ZPPR12	Loading 37	5.3	0.4	6.7

ZPPR-2 configurations (up to 62%), suggest a combination of modeling limitations and sensitivity to nuclear data.

In conclusion, the SVR analysis demonstrates that MCNP calculations capture the general trends of the sodium void reactivity, but with appreciable variance depending on reactor configuration.

4.4 Isothermal temperature coefficient

The isothermal temperature coefficient (ITC) results are collected in Table 4.7. For the temperature parameter, the only facility for which the analysis was carried out is FFTF. The calculation-over-experiment ratio is close to unity (0.88), corresponding to a modest deviation of 12%. The total uncertainty is consistent

(67%), primarily driven by the significant nuclear data component (64.9%), while experimental (15%) and statistical (8.1%) contributions are considerably smaller. This suggests that the reliability of the ITC calculation for FFTF is predominantly limited by the uncertainties in nuclear data, consistent with trends observed for other reactivity parameters in fast-spectrum benchmarks.

Table 4.7: ITC results: C/E and error sources

Facility	**C/E**	**C/E-1 [%]**	**Total Unc. [%]**
FFTF	0.88	12	67
Facility	**Experimental Unc. [%]**	**Statistical Unc. [%]**	**Nuclear Data Unc. [%]**
FFTF	15	8.1	64.9

4.5 Confidence levels

This section provides an overview of the distribution of the calculated-to-experimental ratios for the main reactivity parameters: the effective multiplication factor, the control rod worth, and sodium void reactivity. Furthermore, it allows an assessment of the overall consistency and reliability of the MCNP calculations relative to experimental data. Each normal distribution refers to the benchmark experiments considered for the different parameters under study.

Effective multiplication factor
The distribution of k_{eff} C/E ratios presented in Figure 4.8 displays a narrow, symmetric Gaussian profile centered at 0.99894, with 1σ confidence interval of (0.99427–1.00361). This confirms the high accuracy and consistency of the MCNP calculations in predicting system criticality and reflects the robustness of the computational model. The limited spread and the average total uncertainty in the order of 2σ further confirm that both experimental and nuclear data uncertainties are well constrained for this parameter, except for the outliers.

Control rod worth
For the control rod worth (Figure 4.9), the C/E distribution remains approximately symmetric around unity but shows a broader spread compared to k_{eff}, having 1σ standard deviation up to 0.03514. Every case lies within the 2σ confidence interval, consistent with the uncertainty levels reported in the corresponding CRW table (see Table 4.3). This dispersion, and the fact that the uncertainty of several

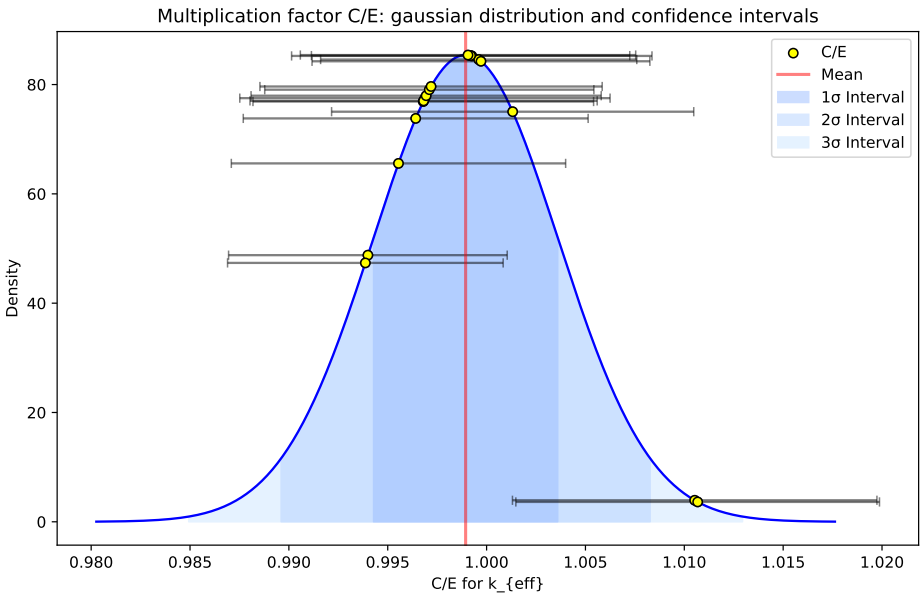

Figure 4.8: k_{eff} : normal distribution of C/E and confidence interval

cases is below 2σ, reflects the increased complexity in modeling absorber materials and control rod configurations. Also, the sensitivities are generated during the post-processing of the MCNP outputs, and this may introduce a propagation of uncertainties for the sensitivity profiles themself. Nevertheless, the Gaussian shape and the proximity of the mean to one confirm the absence of systematic errors in the simulations with respect to the benchmark values.

Sodium void reactivity

Figure 4.10 displays the widest spread among the three distributions, extending from approximately 0.5 to 1.6 in the C/E ratio, with 1σ being equal to 0.15108. This dispersion is consistent with previously observed large uncertainties (20–60%) and the strong sensitivity of the sodium void effect to different configurations. The Gaussian shape remains visible but noticeably broader, suggesting that while the simulations provide an overall good prediction, their precision is limited by the total uncertainty, which is dominated by the nuclear data component for the majority of the cases. However, the width of the error bars, crossing the mean of the distribution in nearly all cases (including the most distant ones), still indicates a global statistical coherence between calculations and experiments.

Overall, these confidence interval plots confirm the robustness of the MCNP-based assessment across the different reactivity parameters. While k_{eff} predic-

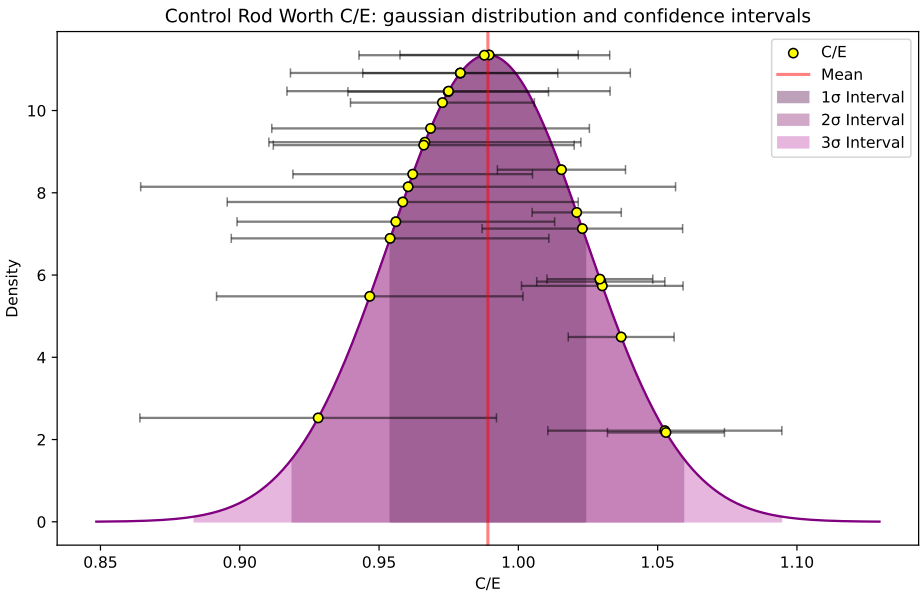

Figure 4.9: CRW: normal distribution of C/E and confidence interval

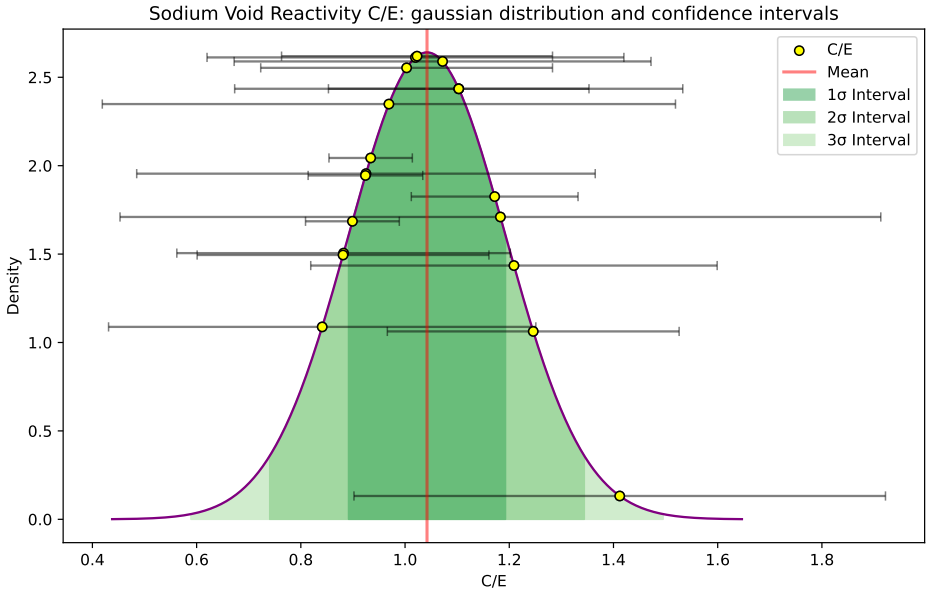

Figure 4.10: SVR: normal distribution of C/E and confidence interval

tions demonstrate excellent accuracy and consistency, CRW and in particular SVR show broader confidence intervals, dominated by nuclear data and experimental uncertainties. The increasing width of the Gaussian distributions from k_{eff} to the reactivity coefficients quantitatively suggests how modeling complexity and uncertainty sources accumulate as the parameter depends on higher-order physics phenomena. The strong central alignment of all distributions demonstrates that the methodology does not introduce systematic bias, while the normalized spread reflects realistic uncertainty propagation for the considered sets of experiments.

4.6 GLLS

In this framework, GLLS has been explored as a data assimilation algorithm to evaluate improvements in k_{eff} reduction. As detailed in Section 2.6, GLLS is commonly used to adjust nuclear data libraries, although it is here used in its variant as a critical safety assessment tool. In this context, the objective is to improve the predicted multiplication factor value for an application that does not have the experimental value for comparison (e.g., a new reactor design), using a dataset of $C - E$ values from relevant criticality experiments. What makes an experiment relevant has been discussed in Chapter 3. In this thesis, two cases are presented: one using a covariance matrix and sensitivity vectors containing thirteen isotopes that are present in each of the modeled experiments, the latter case using only the five common actinides among the calculated benchmark cases (^{235}U,^{238}U, ^{239}Pu, ^{240}Pu, ^{241}Pu).

The order of the experiments was determined using the representativeness ranking calculated in Section 3.3, where it has also been noticed that the ranking slightly changes when using these two different sets of isotopes. The two cases are presented to investigate any discrepancies on the GLLS outputs: since the actinides are the major contributors to the uncertainty due to the nuclear data for the reference reactor ALFRED, evaluating the impact on the GLLS algorithm could also be meaningful.

Figure 4.11 illustrates the impact of using experiments similar to the reference case to obtain a more accurate estimate of the reference k_{eff} value. The values labeled with experiment names represent the impact of a single contribution, while (18+17+...+) is the impact of using an incremental number of experiments combined. It can be observed that for cases where the *a priori* bias is small, the impact on the *a posteriori* bias, that is, the calculated k_{eff} value of the application subtracted from the posterior k_{eff} of the application expressed in pcm, is minimal. When the difference between the calculations and the experimental value

is positive, the GLLS method compensates with a negative contribution. This concept can be observed in Figure 4.11 and 4.13, on the left part of the plots. In particular, BSF-61-1 and BFS-61-2 experiments, which have the largest and most positive computational biases among the results' dataset, show that their singular effect is strongly negative. Conversely, if the calculation bias is negative, as in most cases in this work (see Section 4.1), the *a posteriori* bias will be positive. This means that the models are systematically underestimating the experimental values. GLLS balances this tendency, achieving an *a posteriori* value that is around 200 pcm and 55 pcm higher than the calculated value for ALFRED for the 13-isotopes and 5-actinides cases, respectively. Considering only the common actinides reduces the posterior bias significantly.

Figures 4.12 and 4.14 show that using GLLS could also lower the uncertainty due to nuclear data to around 140 pcm for both cases. Here the influence of $C - E$ is neglected since it is not part of the equations. Substantially, the *a posteriori* uncertainty is calculated using the sensitivity vectors and a new covariance matrix where the adjusted nuclear data are embedded.

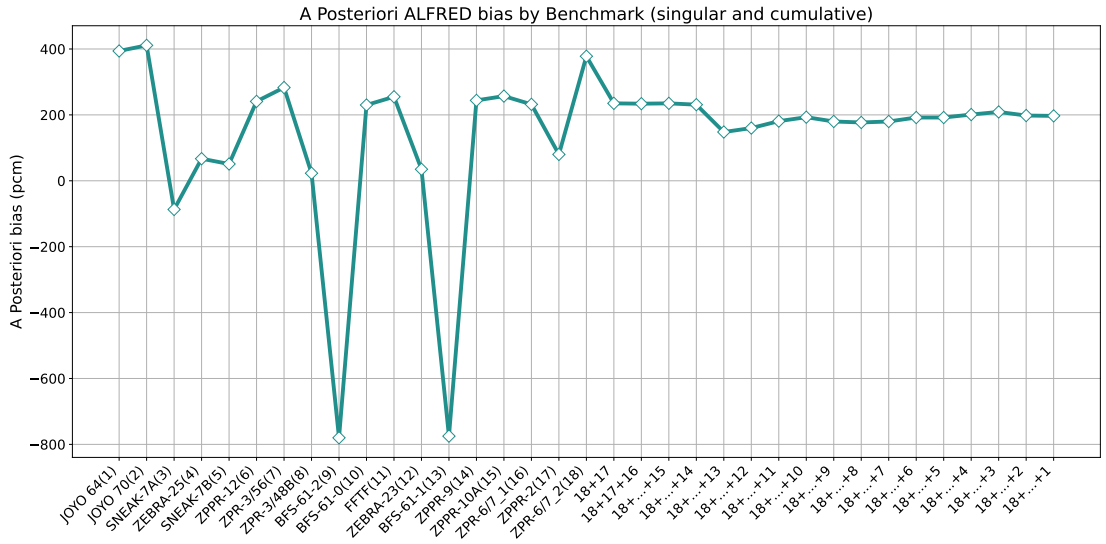

Figure 4.11: Singular and cumulative a posteriori ALFRED bias by benchmark, in the case of 13 isotopes.

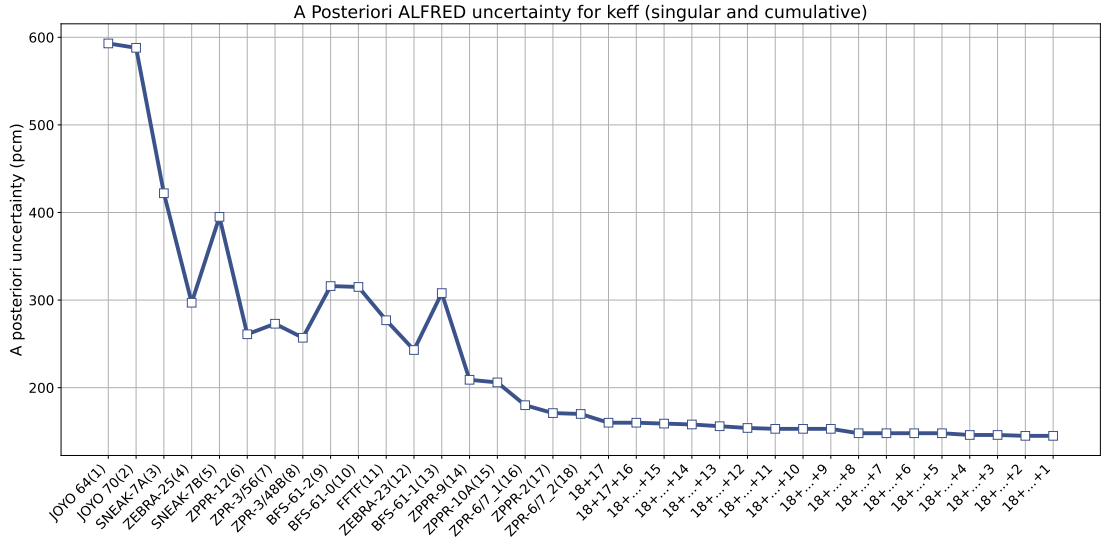

Figure 4.12: Singular and cumulative a posteriori ALFRED uncertainty for k_{eff} , in the case of 13 isotopes.

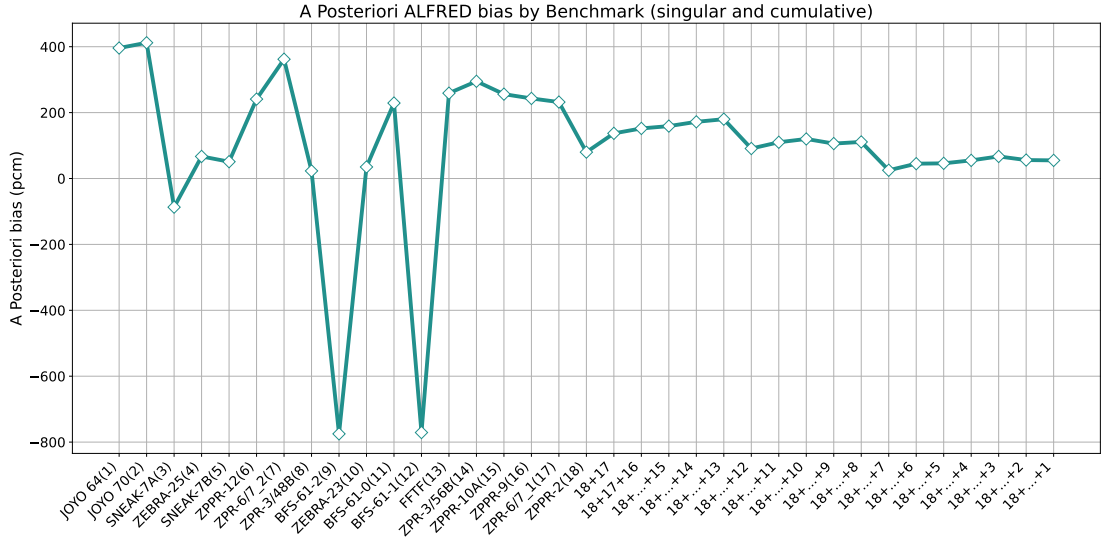

Figure 4.13: Singular and cumulative a posteriori ALFRED bias by benchmark, in the case of 5 actinides.

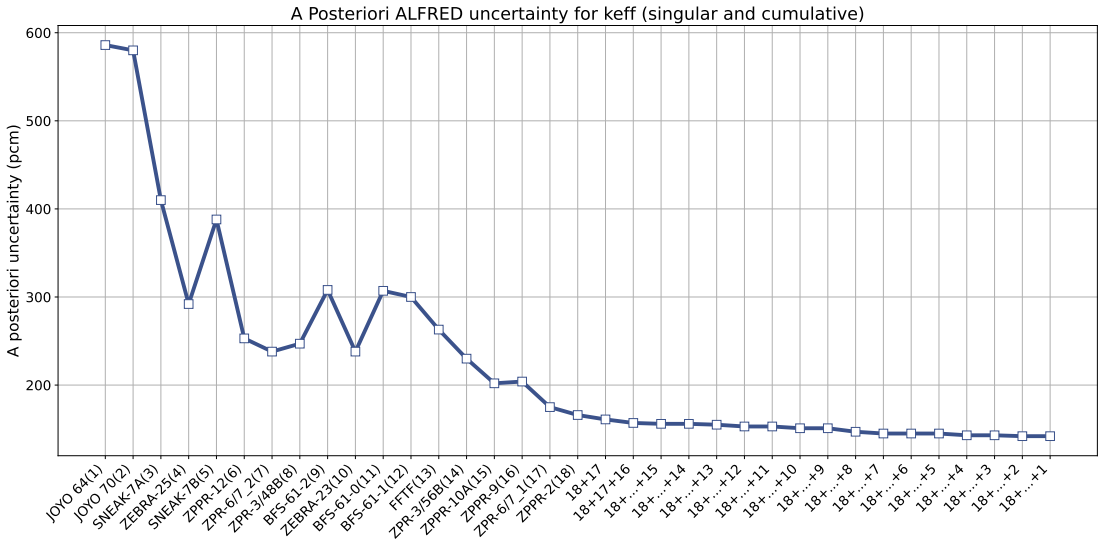

Figure 4.14: Singular and cumulative a posteriori ALFRED uncertainty for k_{eff} , in the case of 5 actinides.

4.7 Results discussion

The results presented demonstrate that MCNP, combined with ENDF/B-VIII.0 nuclear data library, provides accurate predictions for three groups of fast-spectrum benchmark experiments (k_{eff} , CRW, SVR). The total CPU time was roughly 120 hours, with individual runtimes varying from 2 to 3 hours depending on the configuration size.

For the effective multiplication factor, the C/E ratios ranged from 0.994 to 1.011, with most deviations below 1%. As expected, the analysis highlighted that nuclear data uncertainties dominate the total uncertainty (typically 700–940 pcm), while experimental and statistical components were minor. Sixteen out of eighteen benchmarks lay within the uncertainty margins, confirming strong consistency between simulations and experiments, except for the outliers. BFS-61-1 and BFS-61-2 present a large discrepancy between the calculated and the benchmark values. As already noted, the uncertainty due to the nuclear data cannot account for such a considerable deviation. These inconsistencies may indicate possible modeling approximation issues specific to these configurations.

The control rod worth benchmarks showed C/E ratios between 0.93 and 1.05, with total uncertainties ranging from 3% to 10%. Despite small systematic deviations in individual facilities (underestimation for FFTF and JOYO, overestimation for ZPPR cases), the overall balance indicated no systematic bias. Compared to other parameters under study, in the majority of the CRW cases, the experimental uncertainties are higher than the nuclear data contributions, while the Monte Carlo statistical component remained negligible. This pattern is particularly evident when observing the FFTF measurements. Here, while the calculations are consistent with the experimental results, the possibility of investigating the model accuracy and the nuclear data impact is limited by the experimental uncertainty component.

For sodium void reactivity, the C/E ratios exhibited a broader dispersion (0.84–1.41), reflecting higher sensitivity to nuclear dataand modeling assumptions. Although all cases fell within total uncertainty bands (up to 60%), the results highlighted the strong dependence of void reactivity predictions on nuclear data quality. Regarding SFR designs, many efforts have been dedicated to obtaining more reliable cross-sections using [98, 99, 100], using GLLS or comparable techniques and focusing on the sodium cross-section for specific libraries. Clearly, while these approaches are out of scope for this work, they stressed the influence and the potential benefits of the adjustment of nuclear data for tailored applications.

Since the isothermal temperature coefficient was evaluated only for FFTF, this

parameter evidently does not meet the criteria to provide a statistical basis for meaningful assessment. Consequently, it is not recommended to use this result for code validation purposes at this stage. Additional experimental data, which are not available in the current literature, are required to ensure both statistical robustness and result consistency before reliable employment in qualification activities.

The idea under GLLS is to use experiments similar to the application case to obtain a better estimate of the application value. As already mentioned, in this case study, many set-ups from the same facilities are considered, and the effect of similar benchmarks might be redundant. There is room for further investigation into how this method could be applied, as concerns may arise from the optimal number of experiments used or the isotopes taken into account, and, more importantly, the correlation between experiments as initial information (not the correlation that can be calculated through the sensitivity profiles). The selection of criticality benchmarks may have a significant effect on the estimation of the application case k_{eff} bias and its uncertainty. As reported in the final report of the WPNCS/SG11 task used for the verification process for the data assimilation method [91], for many real-life criticality safety applications, the benchmark selection impact is typically much smaller than the one observed during the computational exercise. In fact, here the *a posteriori* bias is ∼200 pcm and ∼55 pcm for thirteen and five isotopes considered respectively, while the *a posteriori* uncertainty is around 140 pcm in both cases.

On the other hand, the benchmark experiments chosen could share common characteristics, and using more experiments from the same facility, even if they bring a good representation of the application case, the effect on the bias reduction could be mitigated. Observing the results obtained in Figure 4.11 and 4.13, this pattern could be clearly recognized. In fact, for the GLLS case with 13 common isotopes, the first two most similar experiments seem to drive the final posterior value. Adding the following sixteen benchmarks does not appreciably influence the k_{eff} bias in the end. The 5-actinides case behaves similarly: here, the cumulative trend suggests a stronger influence of the first most representative case.

Unfortunately, the IRPhE database does not include correlation values between benchmark cases. Since many facilities shared different experiments, it would be invaluable to know (or at least have a reliable estimate) of the experimental correlation, particularly when the GLLS method is applied. In fact, the equation implemented (see Eq. (2.55)) includes the experimental covariance matrix, which was constructed using the variances from the experimental uncertainties in the handbook, assuming no correlation (i.e., all non-diagonal values are set to zero).

Taking into account more information regarding the experimental cases could lead to a minor overall impact on the application case. Therefore, it requires further

analysis before it can be proposed as a quantity of interest in a validation dossier. Despite this caution, it remains an important outcome of this PhD work, since it demonstrates the potential advantage resulting from the development of a fully verified algorithm that can be used with confidence in future applications.

Chapter 5

Conclusions

This thesis presented a preliminary assessment of the predictive capabilities of the MCNP code for Lead-cooled Fast Reactor (LFR) applications, with particular reference to the ALFRED design. The research was framed within the general context of uncertainty quantification and data assimilation for neutronics analyses, aiming to enhance confidence in computational results used in reactor design and to make a significant contribution to the qualification process of the MCNP code applied to LFRs. This final chapter summarizes the main findings of the study and outlines possible directions for future research.

5.1 Summary of the findings

The results obtained in this work confirm that the MCNP 6.3.0 code, along with the ENDF/B-VIII.0 nuclear data library, provides reliable predictions for a broad set of benchmark experiments from the IRPhE database, including the effective multiplication factor, control rod worth, and sodium void reactivity. Overall, the analyses revealed a strong consistency between calculated and experimental results, with most discrepancies falling within the combined uncertainty margins.

For the effective multiplication factor, the simulations achieved excellent agreement with experiments, with deviations generally below 1%. The uncertainty analysis demonstrated that nuclear data uncertainties dominate the total variance, while experimental and statistical contributions remain secondary. Similarly, the control rod worth benchmarks showed a balanced performance across different facilities, with deviations typically within 5% and no evidence of systematic bias deriving from the computational process. The set of benchmark experiments from IRPhE

with sodium coolant showed greater dispersion, reflecting the parameter's greater sensitivity to modeling assumptions and nuclear data. Nevertheless, all calculated values were found to be consistent with the reference data. The isothermal temperature coefficient, analyzed for a single FFTF case, confirmed trends observed for other parameters, though the limited dataset precludes statistical considerations.

Although there is a general agreement, the a priori accuracies credited to MCNP still impose rather large potential margins to the design, particularly, although less intuitively, for the k_{eff} : indeed, the parameter estimated with the higher accuracy. In this regard, the implementation of the GLLS data assimilation tool demonstrated its potential for integrating experimental information to enhance MCNP's predictive capability. By incorporating data from representative benchmarks, the posterior estimates for the ALFRED case showed that the bias on the calculated value could be almost eliminated, and only a slight underestimation (55–200 pcm) would remain. Moreover, the uncertainty due to nuclear data, which is the main component of the total uncertainty, could be significantly reduced to about 140 pcm. These findings confirm that data assimilation can meaningfully improve the precision of neutronic predictions, especially for systems lacking direct experimental references.

Although the GLLS results are promising, their broader applicability requires further investigation, particularly regarding the treatment of experimental correlations and the representativeness of selected benchmarks. Nonetheless, the verified implementation of this methodology represents an essential outcome of this research, establishing a foundation for future studies.

5.2 The value of implementing verified tools

During verification of the uncertainty quantification algorithm, an important finding was made. The verification was performed for a single benchmark case, SNEAK-7B, using results obtained with TSUNAMI-IP from the SCALE code system as reference.

The comparison revealed that the covariance matrix provided by ENEA does not include cross-correlations among different isotopes (e.g., fission cross sections for ^{238}U and ^{239}Pu). As a consequence, the propagated uncertainty on k_{eff} may be underestimated, particularly in systems where major actinides dominate the sensitivity profile. In contrast, the covariance data processed by TSUNAMI-IP include the mentioned cross-correlations, but lack internal correlations for the ^{238}U (e.g., elastic-inelastic, inelastic-fission reactions). This specific deficiency was identified

as a non-negligible contributor to the discrepancy observed between the total uncertainties predicted by the two approaches. Beyond the numerical comparison itself, this verification exercise demonstrated the critical impact of the covariance matrix on the uncertainty quantification. The outcome therefore provides a concrete recommendation for the ENEA NUC-ENER-PRO group: future covariance evaluations should, at minimum, incorporate cross-correlations among the major actinides to ensure a more realistic estimation of nuclear data–induced uncertainties in k_{eff} .

The availability of an in-house tool for sensitivity and covariance processing was revealed as an asset in this work, enhanced by the use of Python as a programming language, which enabled great flexibility for multiple applications. The developed Python-based framework allows for the practical manipulation of the MCNP output file to extract sensitivity coefficients, for straightforward implementation and testing of different processing modules, and also for clean visualization. During this thesis, the first phase of post-processing consisted of transforming the sensitivity coefficient and the covariance matrix in *.npy* file formats. Subsequently, this format was directly used in scripts dedicated to computing the uncertainty due to nuclear data for the modeled experiments, as well as in the representativeness formula to obtain rankings by similarity and, finally, in the GLLS methods.

Ensuring that all computational modules are properly verified is a fundamental requirement for the credibility of any uncertainty quantification or validation effort. In nuclear engineering, where safety assessments and design decisions rely heavily on numerical predictions, the use of verified tools guarantees that observed discrepancies are due to physical modeling or data uncertainties rather than coding or implementation errors. In this work, the verification of the post-processing framework was extensively done following the recommendations of the ASN Guide No. 28 [45], which emphasizes the need to treat ancillary software as an integral part of the overall qualification process. By systematically testing each module, the developed tools now ensure the robustness and reproducibility of the uncertainty propagation and data assimilation analyses. This verification step not only enhances confidence in the presented results but also establishes a reliable foundation for future extensions of the framework.

5.3 Future developments

Currently, this framework is based on the use of MCNP outputs from which sensitivity coefficients are extracted. However, any code that can calculate the energy-dependent sensitivities of a response with respect to cross-section changes can be

used. As well as for the sensitivity coefficients, any covariance matrix with the same energy discretization as the sensitivity vector can be used to propagate the uncertainties.

In this thesis, one of the objectives was to evaluate the accuracy of the specific computational "package" selected (MCNP 6.3.0 code & ENDF/B-VIII.0 library). However, both the sandwich rule and the GLLS algorithm can be used to evaluate the impact of different nuclear data libraries on the same systems. The library in use was taken as an initial condition, and comparing how different libraries behave was out of scope, since part of the effort was dedicated to implementing and verifying a computational framework to support the qualification of the transport code (with the affiliated library) in use.

Regarding the GLLS method, its potential could be further exploited. In the present implementation, the improvement of k_{eff} and the associated reduction of nuclear data uncertainty for the application case are achieved through an algorithm that implicitly incorporates nuclear data adjustments, without explicitly exposing them. Consequently, the framework could be extended to extract additional information. In particular, identifying which isotopes and which reaction energy groups undergo the most significant modifications in order to produce the observed improvement in the integral parameter of interest.

From a code development perspective, the usability of the proposed framework could be enhanced by implementing automated processes to handle the MCNP output files or by developing a graphical user interface to facilitate its use by non-expert users. In addition, since comprehensive and high-quality datasets are essential for effective code benchmarking and validation, it would be valuable to submit the newly obtained sensitivity data for LMFR cases to the OECD-NEA for evaluation and potential inclusion in the IDAT tool. At present, IDAT contains sensitivity data for only a limited number of cases based on older nuclear data libraries; thus, expanding its database with updated results would significantly improve its relevance and support the reactor physics research community in representativeness ranking and robustness of future validation studies.

5.4 Final remarks

Despite advancements in computational tools and extensive nuclear data libraries, integral experiments in zero-power facilities continue to play a significant role in the validation of nuclear data and in the licensing of new core designs, especially to avoid applying the most conservative safety margins, which could affect the overall performance of the new system in terms of economics and efficiency. Unfortunately,

experiments in the LMFR section of the IRPhE database are limited, and the majority are sodium-cooled. The need for more experimental data to serve as a benchmark for neutronics codes is evident from the statistics (18–26 cases per parameter). Developing new experimental facilities, reviving old ones, and sharing data from existing, currently private experiments could significantly improve this IRPhE section and facilitate the licensing path of new reactor designs such as LFRs.

This thesis has demonstrated that rigorous uncertainty quantification and data assimilation can significantly enhance confidence using the MCNP code for neutronic simulations along with the ENDF/B-VIII.0 nuclear data library. The proposed integrated approach supports the qualification of MCNP for LFR design application and contributes to the broader goal of establishing reliable computational results, especially in the described domain.

Bibliography

[1] IEA. *Global Energy Review 2025*. International Energy Agency, 2025. URL: https://www.iea.org/reports/global-energy-review-2025.

[2] IEA. *From Taking Stock to Taking Action*. International Energy Agency, Sept. 2024. URL: https://www.iea.org/reports/from-taking-stock-to-taking-action.

[3] IEA. *World Energy Outlook 2024*. International Energy Agency, 2024. URL: https://www.iea.org/reports/world-energy-outlook-2024.

[4] IAEA. *Nuclear Energy and Climate Change: Questions and Answers on Progress, Challenges and Opportunities*. Outlooks. Vienna: IAEA, 2023. URL: https://www.iaea.org/publications/15503/nuclear-energy-and-climate-change-questions-and-answers-on-progress-challenges-and-opportunities.

[5] NEA. *Meeting Climate Change Targets: The Role of Nuclear Energy*. Tech. rep. OECD Publishing, Paris, 2022.

[6] IAEA. *Nuclear Power Reactors in the World*. Reference Data Series 2. Vienna: IAEA, 2024. ISBN: 978-92-0-122224-4. URL: https://www.iaea.org/publications/15748/nuclear-power-reactors-in-the-world.

[7] T. Li et al. "Can nuclear power products mitigate greenhouse gas emissions? Evidence from global trade network". In: *International Journal of Environmental Research and Public Health* 19.13 (2022), p. 7808.

[8] IEA. *Nuclear Power and Secure Energy Transitions*. URL: https://www.iea.org/reports/nuclear-power-and-secure-energy-transitions. June 2022.

[9] IEA. *The Path to a New Era for Nuclear Energy*. URL: https://www.iea.org/reports/the-path-to-a-new-era-for-nuclear-energy. Jan. 2025.

[10] IAEA. *Power Reactor Information System*. 2025. URL: https://pris.iaea.org/pris/ (visited on 08/25/2025).

[11] R. A. Dunlap. *Generation IV nuclear reactors: design, operation and prospects for future energy production*. IOP Publishing, 2024. ISBN: 978-0-7503-6069-2. DOI: 10.1088/978-0-7503-6069-2. URL: https://dx.doi.org/10.1088/978-0-7503-6069-2.

[12] *A Technology Roadmap for Generation IV Nuclear Energy Systems*. U.S. DOE Nuclear Energy Research Advisory Committee and the Generation IV International Forum, 2002. URL: https://www.gen-4.org/gif/jcms/c_40481/technology-roadmap.

[13] OECD/NEA. *Technology Roadmap Update for Generation IV Nuclear Energy Systems*. Tech. rep. Generation IV International Forum - GIF, 2014.

[14] A. Alemberti et al. *LFR System Safety Assessment*. Generation IV International Forum - GIF, 2020. URL: https://www.gen-4.org/sites/default/files/2024-07/2020%20RSWG%20GIF%20LFR%20SSA%20June%202020.pdf.

[15] R. Caciuffo et al. "Generation-IV nuclear reactor systems". In: *EPJ Web of Conferences*. Vol. 246. EDP Sciences. 2020, p. 00011. DOI: 10.1051/epjconf/202024600011. URL: https://doi.org/10.1051/epjconf/202024600011.

[16] C. F. Smith et al. "Chapter 6 - Lead-cooled Fast Reactors (LFRs)". In: *Handbook of Generation IV Nuclear Reactors (Second Edition)*. Ed. by I. L. Pioro. Second Edition. Woodhead Publishing Series in Energy. Woodhead Publishing, 2023, pp. 195–230. ISBN: 978-0-12-820588-4. DOI: https://doi.org/10.1016/B978-0-12-820588-4.00018-9. URL: https://www.sciencedirect.com/science/article/pii/B9780128205884000189.

[17] Westinghouse Electric Company LLC. *Demonstration Lead-cooled Fast Reactor Details: Westinghouse Lead-cooled Fast Reactor*. Tech. rep. RT-TR-15-30, Revision 1. Idaho National Laboratory, Mar. 2016. URL: https://art.inl.gov/ART%20Document%20Library/Advanced%20Demonstration%20and%20Test%20Reactor%20Options%20Study/Attachment_4_Westinghouse_LFR_DR.pdf.

[18] K. Zhang et al. "SUMMER: A small modular lead-bismuth-cooled fast reactor for mobile energy supply". In: *Progress in Nuclear Energy* 164 (2023), p. 104860. ISSN: 0149-1970. DOI: https://doi.org/10.1016/j.pnucene.2023.104860. URL: https://www.sciencedirect.com/science/article/pii/S0149197023002950.

[19] J. Wallenius. *Status of Blykalla's commercial LFR development in Sweden*. URL: https://www.gen-4.org/resources/webinars/gif-talks-industry-series-2-lfr-developers-blykalla. July 2024.

[20] K. Aoto et al. "A summary of sodium-cooled fast reactor development". In: *Progress in Nuclear Energy* 77 (2014), pp. 247–265. ISSN: 0149-1970. DOI: https://doi.org/10.1016/j.pnucene.2014.05.008. URL: https://www.sciencedirect.com/science/article/pii/S0149197014001279.

[21] Generation IV International Forum. *GIF 2024 Annual Report*. 2024. URL: https://www.gen-4.org/resources/annual-reports/2024-gif-annual-report.

[22] G. Toshinsky et al. "Safety aspects of SVBR-75/100 reactor". In: *Advanced Nuclear* (2002), p. 71.

[23] J. Sienicki et al. "Role of small lead-cooled fast reactors for international deployment in worldwide sustainable nuclear energy supply". In: *Proceedings of ICAPP 2007*. 2007.

[24] Generation IV International Forum. *GIF 2023 Annual Report*. 2023. URL: https://www.gen-4.org/resources/annual-reports/2023-gif-annual-report.

[25] World Nuclear News. *Construction licence issued for Russia's BREST reactor*. 2021. URL: https://world-nuclear-news.org/articles/construction-licence-issued-for-russias-brest-reac (visited on 08/21/2025).

[26] M. Tarantino. *Lead-cooled Fast Reactor (LFR) Development – Status & Perspectives*. URL: https://www.gen-4.org/resources/webinars/education-and-training-series-96-lead-cooled-fast-reactor-lfr-development-status. Dec. 2024.

[27] Confindustria Press Communication. *Confindustria: steering committee on nuclear power, development of the national energy mix and Small Modular Reactors (SMRs) launched*. Oct. 2024. URL: https://www.confindustria.it/en/press_communications/confindustria-launches-steering-committee-on-nuclear-power-for-the-development-of-the-national-energy-mix-and-small-modular-reactor-smr/ (visited on 08/21/2025).

[28] World Nuclear News. *Cabinet moves to reverse Italy's anti-nuclear stance*. Mar. 2025. URL: https://www.world-nuclear-news.org/articles/cabinet-moves-to-reverse-italys-anti-nuclear-stance (visited on 08/21/2025).

[29] Reuters. *Italy's Leonardo, Enel and Ansaldo reach deal on nuclear joint venture*. 2025. URL: https://www.reuters.com/business/energy/italys-leonardo-enel-ansaldo-reach-deal-nuclear-joint-venture-2025-04-03/ (visited on 08/21/2025).

[30] W. Li et al. "Numerical study on the characteristics of the LBE thermal stratification in a scaled-down hot pool". In: *Annals of Nuclear Energy* 211 (2025), p. 110900. ISSN: 0306-4549. DOI: https://doi.org/10.1016/j.anucene.2024.110900. URL: https://www.sciencedirect.com/science/article/pii/S0306454924005632.

[31] I. S. Hwang et al. "MicroURANUS Leveraged on Inert Coolant for Maritime Safety". In: *Proceedings of GLANST-2024*. ENEA,Brasimone, Italy. 2024.

[32] J.-K. Lee. "Development of Test Facility to Study Erosion and Corrosion of Materials". In: *Proceedings of GLANST-2024*. ENEA,Brasimone, Italy. 2024.

[33] D. J. O'Grady et al. *Capability Enhancements for System-level thermal Hydraulic Modeling of Lead Fast Reactors*. Tech. rep. Argonne National Laboratory (ANL), Argonne, IL (United States); Westinghouse Electric Company LLC, Cranberry Township, PA (United States); Fauske & Associates, LLC, Burr Ridge, IL (United States), Aug. 2024. DOI: 10.2172/2429437. URL: https://www.osti.gov/biblio/2429437.

[34] C. Stansbury et al. *An Integrated Design Approach to Address Safety of the Westinghouse LFR: An Innovative Pool-Type, Liquid Lead Cooled Fast Reactor*. Tech. rep. IAEA, Vienna, Austria, 2025. URL: https://www.iaea.org/publications/15776/topical-issues-in-nuclear-installation-safety.

[35] R. A. Thomas et al. *SAS4A/SASSYS-1 Modeling Improvements for the Transition to Natural Circulation*. Tech. rep. Argonne National Laboratory (ANL), 2024. URL: https://www.osti.gov/biblio/2376867.

[36] N. E. Stauff et al. "Neutronic Benchmark on the Westinghouse Lead Fast Reactor". In: *2024 International Conference on Physics of Reactors, PHYSOR 2024*. 2024, pp. 2130–2143.

[37] Generation IV International Forum. *LFR Current Developments*. 2025. URL: https://www.gen-4.org/generation-iv-criteria-and-technologies/lead-fast-reactors-lfr (visited on 08/21/2025).

[38] G. Grasso et al. "The core design of ALFRED, a demonstrator for the European lead-cooled reactors". In: *Nuclear Engineering and Design* 278 (2014), pp. 287–301. ISSN: 0029-5493. DOI: https://doi.org/10.1016/j.nucengdes.2014.07.032. URL: https://www.sciencedirect.com/science/article/pii/S0029549314004361.

[39] M. Frignani et al. "ALFRED: A revised concept to improve pool related thermal-hydraulics". In: *Nuclear Engineering and Design* 355 (2019), p. 110359. ISSN: 0029-5493. DOI: https://doi.org/10.1016/j.nucengdes.2019.110359. URL: https://www.sciencedirect.com/science/article/pii/S0029549319303930.

[40] G. Grasso et al. "An improved design for the ALFRED core". In: *International Congress on Advances in Nuclear Power Plants (ICAPP 2019)*. SFEN. Juan-les-Pins, France, May 2019.

[41] IAEA. *Safety of Nuclear Power Plants: Design*. Specific Safety Requirements SSR-2/1 (Rev. 1). Vienna: IAEA, 2016. ISBN: 978-92-0-109315-8. URL: https://www.iaea.org/publications/10885/safety-of-nuclear-power-plants-design.

[42] IAEA. *Deterministic Safety Analysis for Nuclear Power Plants*. Specific Safety Guide SSG-2 (Rev.1). Vienna: IAEA, 2019. ISBN: 978-92-0-102119-9. URL: https://www.iaea.org/publications/12335/deterministic-safety-analysis-for-nuclear-power-plants.

[43] S. Eom et al. "Chapter 22 - Regulatory and licensing challenges with Generation-IV nuclear energy systems". In: *Handbook of Generation IV Nuclear Reactors (Second Edition)*. Ed. by I. L. Pioro. Second Edition. Woodhead Publishing Series in Energy. Woodhead Publishing, 2023, pp. 837–864. ISBN: 978-0-12-820588-4. DOI: https://doi.org/10.1016/B978-0-12-820588-4.00004-9. URL: https://www.sciencedirect.com/science/article/pii/B9780128205884000049.

[44] J. Dean et al. *Guide for Validation of Nuclear Criticality Safety Calculational Methodology*. NUREG/CR-6698. Division of Fuel Cycle Safety and Safeguards, US Nuclear Regulatory Commission, 2001. URL: https://www.nrc.gov/docs/ML0502/ML050250061.pdf.

[45] C. Herer. "ASN/IRSN guide 28: Qualification of scientific computing tools used in the nuclear safety case – 1st barrier". In: *Nuclear Engineering and Design* 405 (2023), p. 112221. ISSN: 0029-5493. DOI: https://doi.org/10.1016/j.nucengdes.2023.112221. URL: https://www.sciencedirect.com/science/article/pii/S0029549323000705.

[46] J. A. Kulesza et al. *MCNP® Code Version 6.3.0 Theory & User Manual*. Tech. rep. LA-UR-22-30006, Rev. 1. Los Alamos, NM, USA: Los Alamos National Laboratory, Sept. 2022. DOI: 10.2172/1889957. URL: https://www.osti.gov/biblio/1889957.

[47] C. J. Josey et al. *MCNP® Code Version 6.3.0 Verification & Validation Testing*. Tech. rep. LA-UR-22-32951, Rev. 1. Los Alamos, NM, USA: Los Alamos National Laboratory, Dec. 2022. DOI: 10.2172/1907750. URL: https://www.osti.gov/biblio/1907750.

[48] J.-F. Parisot. *Neutronics*. CEA, 2015. URL: https://www.cea.fr/english/Pages/resources/nuclear-energy-monographs/neutronics.aspx.

[49] A. Del Nevo et al. *Development of best estimate numerical tools for LFR design and safety analysis*. Tech. rep. ENEA, 2017. URL: https://hdl.handle.net/20.500.12079/8016.

[50] J. Leppänen. *Development of a new Monte Carlo reactor physics code*. VTT Technical Research Centre of Finland, 2007. URL: https://aaltodoc.aalto.fi/items/3088278f-283b-4893-a329-0283fce28b05.

[51] A. L. Lund et al. *Implementation and Validation of Photon Transport in OpenMC*. Tech. rep. Argonne National Laboratory (ANL), Argonne, IL (United States), Dec. 2018. DOI: 10.2172/1490825. URL: https://www.osti.gov/biblio/1490825.

[52] J. D. Bess et al. "Intrinsic value of the international benchmark projects, ICSBEP and IRPhEP, for advanced reactor development". In: *Frontiers in Energy Research* 11 (2023), p. 1085788. ISSN: ISSN 2296-598X. DOI: 10.3389/fenrg.2023.1085788. URL: https://www.osti.gov/biblio/1969136.

[53] J. B. Briggs et al. "The International Criticality Safety Benchmark Evaluation Project". In: *Nuclear Science and Engineering* 145.1 (Sept. 2003), pp. 1–10. ISSN: 0029-5639. DOI: 10.13182/NSE03-14. URL: https://www.osti.gov/biblio/20804870.

[54] J. B. Briggs et al. "An Overview of the International Reactor Physics Experiment Evaluation Project". In: *Nuclear Science and Engineering* 178.3 (Oct. 2014), pp. 269–279. ISSN: 0029-5639. DOI: 10.13182/NSE14-27. URL: https://www.osti.gov/biblio/1178048.

[55] NEA. *International Handbook of Evaluated Reactor Physics Benchmark Experiments*. Paris, France: OECD Nuclear Energy Agency, 2023. URL: https://www.oecd-nea.org/jcms/pl_20279/international-handbook-of-evaluated-reactor-physics-benchmark-experiments-irphe.

[56] V. Dean et al. "ICSBEP Guide to the Expression of Uncertainties". In: *Nuclear Energy Agency* (2008). URL: https://www.oecd-nea.org/upload/docs/application/pdf/2020-03/icsbep_guide_to_the_expression_of_uncertainties.pdf.

[57] A. Dos Santos et al. "Overview of the international reactor physics experiments evaluation project (IRPhEP) guide to the expression of uncertainty". In: *2018 International Conference on Physics of Reactors: Reactor Physics Paving the Way Towards More Efficient Systems, PHYSOR 2018*. Sociedad Nuclear Mexicana, AC. 2018, pp. 3698–3708.

[58] Kochetkov, Anatoly et al. "The Lead-Based VENUS-F Facility: Status of the FREYA Project". In: *EPJ Web of Conferences* 106 (2016), p. 06004. DOI: 10.1051/epjconf/201610606004. URL: https://doi.org/10.1051/epjconf/201610606004.

[59] H. Aït Abderrahim et al. "MYRRHA–A multi-purpose fast spectrum research reactor". In: *Energy conversion and management* 63 (2012), pp. 4–10. ISSN: 0196-8904. DOI: https://doi.org/10.1016/j.enconman.2012.02.025. URL: https://www.sciencedirect.com/science/article/pii/S0196890412000982.

[60] S. M. Bednyakov et al. "The BFS complex–a unique facility to justify the neutronic parameters of the new generation fast reactor cores". In: *Nuclear Energy and Technology* 8.2 (2022), pp. 97–105. DOI: 10.3897/nucet.8.83655.

[61] A. Kochetkov et al. "Integral experiments in the VENUS-F reactor". In: *Annals of Nuclear Energy* 157 (2021), p. 108230. ISSN: 0306-4549. DOI: https://doi.org/10.1016/j.anucene.2021.108230. URL: https://www.sciencedirect.com/science/article/pii/S0306454921001067.

[62] A. Krása et al. "The VENUS-F Reactor for Nuclear Data Validation". In: *Reactor Dosimetry: 16th International Symposium*. ASTM International, Nov. 2018. ISBN: 978-0-8031-7661-4. DOI: 10.1520/STP160820170078. eprint: https://dl.astm.org/stps/book/chapter-pdf/31173/10_1520_stp160820170078.pdf. URL: https://doi.org/10.1520/STP160820170078.

[63] IAEA. *Power Reactors and Sub-Critical Blanket Systems with Lead and Lead-Bismuth as Coolant and/or Target Material*. TECDOC Series 1348. Vienna: IAEA, 2003. ISBN: 92-0-101503-8. URL: https://www.iaea.org/publications/6727/power-reactors-and-sub-critical-blanket-systems-with-lead-and-lead-bismuth-as-coolant-andor-target-material.

[64] M. Tarantino et al. "Overview on lead-cooled fast reactor design and related technologies development in ENEA". In: *Energies* 14.16 (2021). ISSN: 1996-1073. DOI: 10.3390/en14165157. URL: https://www.mdpi.com/1996-1073/14/16/5157.

[65] W. L. Dunn et al. *Exploring Monte Carlo methods*. Elsevier, 2010.

[66] F. B. Brown. *Fundamentals of Monte Carlo Particle Transport*. Presentation LA-UR-05-4983. Los Alamos, NM, USA: Los Alamos National Laboratory, 2005. URL: http://permalink.lanl.gov/object/tr?what=info:lanl-repo/lareport/LA-UR-05-4983.

[67] J. C. Armstrong. *MCNP6.3 Executions in Parallel on Snow*. Tech. rep. Los Alamos National Laboratory (LANL), Los Alamos, NM (United States), 2023. URL: https://www.osti.gov/biblio/2005770.

[68] R. Macfarlane et al. *The NJOY nuclear data processing system, version 2016*. Tech. rep. Los Alamos National Laboratory (LANL), Los Alamos, NM (United States), 2017. DOI: 10.2172/1338791. URL: https://www.osti.gov/biblio/1338791.

[69] F. B. Brown et al. *Guide for Using ENDF/B-VIII.0 Nuclear Data with MCNP*. Tech. rep. LA-UR-20-30460.(Los Alamos National Laboratory, Los Alamos, 2020), 2020. DOI: 10.2172/1755877. URL: https://www.osti.gov/biblio/1755877.

[70] J. L. Conlin et al. *Release of ENDF/B-VIII.0-based ACE data files*. Tech. rep. Los Alamos National Laboratory (LANL), Los Alamos, NM (United States), 2018. DOI: 10.2172/1438139. URL: https://www.osti.gov/biblio/1438139.

[71] C. de Saint Jean et al. "Evaluating nuclear data and their uncertainties". In: *EPJ - Nuclear Sciences & Technologies* 4 (2018). ISSN: 2491-9292. DOI: https://doi.org/10.1051/epjn/2018032. URL: https://www.sciencedirect.com/science/article/pii/S2491929218000456.

[72] *Lib80x - Library based on ENDF/B-VIII.0*. https://nucleardata.lanl.gov/ace/lib80x. Accessed: 2025-09-12.

[73] D. A. Brown. *ENDF-6 formats manual-data formats and procedures for the evaluated nuclear data files ENDF/B-VI, ENDF/B-VII and ENDF/B-VIII*. Tech. rep. Brookhaven National Laboratory (BNL), Upton, NY (United States), 2023. DOI: 10.2172/2007538. URL: https://www.osti.gov/biblio/2007538.

[74] S. Panizo et al. "Sensitivity and uncertainty analyses for advanced nuclear systems (ALFRED, ASTRID, ESFR and MYRRHA)". In: *Progress in Nuclear Energy* 172 (2024), p. 105207. ISSN: 0149-1970. DOI: https://doi.org/10.1016/j.pnucene.2024.105207. URL: https://www.sciencedirect.com/science/article/pii/S0149197024001574.

[75] J. R. Lamproe et al. "Preliminary verification of the MCNP perturbation and fixed-source tally sensitivity tools". In: *Annals of Nuclear Energy* 194 (2023), p. 110040. ISSN: 0306-4549. DOI: https://doi.org/10.1016/j.anucene.2023.110040. URL: https://www.sciencedirect.com/science/article/pii/S0306454923003596.

[76] B. Broadhead et al. "Sensitivity and uncertainty analyses applied to criticality safety validation". In: *NUREG0CR-6655, Vols* 1 (1999). URL: https://www.nrc.gov/reading-rm/doc-collections/nuregs/contract/cr6655/v1/index.

[77] B. T. Rearden. "TSUNAMI-3D: Control module for three-dimensional cross-section sensitivity and uncertainty analysis for criticality". In: *SCALE 5.1 Manual* (2006). URL: https://cir.nii.ac.jp/crid/1573950399774300160.

[78] W. Wieselquist et al. *SCALE 6.3.1 User Manual*. Tech. rep. Oak Ridge National Laboratory (ORNL), Oak Ridge, TN (United States), Feb. 2023. DOI: 10.2172/1959594. URL: https://www.osti.gov/biblio/1959594.

[79] B. C. Kiedrowski. *MCNP6.1 k-Eigenvalue Sensitivity Capability: A User's Guide*. Tech. rep. Los Alamos National Laboratory (LANL), Los Alamos, NM (United States), Mar. 2013. DOI: 10.2172/1072231. URL: https://www.osti.gov/biblio/1072231.

[80] M. L. Williams et al. "Sensitivity analysis of reactivity responses using one-dimensional discrete ordinates and three-dimensional Monte Carlo methods". In: *Proceedings of PHYSOR–2006, American Nuclear Society Topical Meeting on Reactor Physics: Advances in Nuclear Analysis and Simulation*. 2006.

[81] M. Williams et al. *6.7. TSAR: Tool for Sensitivity Analysis of Reactivity Responses*. https://scale-manual.ornl.gov/tsar.html.

[82] https://www.oecd-nea.org/jcms/pl_39859/sensitivities-viewer.

[83] D. G. Cacuci. *Handbook of nuclear engineering*. Vol. 3. Springer Science & Business Media, 2010.

[84] B. T. Rearden et al. *6.3.1 TSUNAMI-IP*. https://scale-manual.ornl.gov/tsunami-ip.html.

[85] *SCALE - Sensitivity and Uncertainty Analysis*. https://www.ornl.gov/team/scale/sensitivity-and-uncertainty-analysis-0. Accessed: 09/04/2025.

[86] M. Salvatores et al. "Methods and issues for the combined use of integral experiments and covariance data: results of a NEA international collaborative study". In: *Nuclear Data Sheets* 118 (2014), pp. 38–71. ISSN: 0090-3752. DOI: https://doi.org/10.1016/j.nds.2014.04.005. URL: https://www.sciencedirect.com/science/article/pii/S0090375214000350.

[87] T. Ivanova et al. "Methodology and issues of integral experiments selection for nuclear data validation". In: *EPJ Web of Conferences* 146 (Jan. 2017), p. 06002. DOI: 10.1051/epjconf/201714606002.

[88] D. Siefman et al. "Stochastic vs. sensitivity-based integral parameter and nuclear data adjustments". In: *The European Physical Journal Plus* 133.10 (2018), p. 429. DOI: https://doi.org/10.1140/epjp/i2018-12303-8.

[89] E. Ivanov et al. "Nuclear data assimilation, scientific basis and current status". In: *EPJ N-Nuclear Sciences & Technologies* 7 (2021), p. 9. ISSN: 2491-9292. DOI: https://doi.org/10.1051/epjn/2021008. URL: https://www.sciencedirect.com/science/article/pii/S2491929221000121.

[90] NEA. *Working Party on Nuclear Criticality Safety (WPNCS)*. https://www.oecd-nea.org/jcms/pl_23012/working-party-on-nuclear-criticality-safety-wpncs. Accessed: 2025-09-10.

[91] A. Hoefer et al. "Bias and correlated data, comparison of methods". In: *Proceedings of ICNC*. 2023, pp. 1–6.

[92] U. Mertyurek. *NEA/WPNCS Sub-Group 14: Performance Benchmark for Error Recovery and Experimental Coverage*. https://sg14.ornl.gov/. Accessed: 2025-09-10.

[93] G. Van Rossum et al. *Python 3 Reference Manual*. Scotts Valley, CA: CreateSpace, 2009. ISBN: 1441412697.

[94] F. Perez et al. "Python: an ecosystem for scientific computing". In: *Computing in Science & Engineering* 13.2 (2010), pp. 13–21. DOI: 10.1109/MCSE.2010.119.

[95] A. Nouri et al. "DICE: database for the international criticality safety benchmark evaluation program handbook". In: *Nuclear science and engineering* 145.1 (2003), pp. 11–19. DOI: 10.13182/NSE03-15. URL: https://doi.org/10.13182/NSE03-15.

[96] I. Hill et al. "IDAT: The international handbook of evaluated reactor physics benchmark experiments database and Analysis tool". In: *Nuclear Science and Engineering* 178.3 (2014), pp. 280–294. DOI: 10.13182/NSE14-37. URL: https://doi.org/10.13182/NSE14-37.

[97] D. M. Castelluccio. "Assessment of the impact of nuclear data uncertainties on the core design of ALFRED". PhD thesis. Università degli Studi di Roma Tor Vergata, 2020.

[98] J. Tommasi et al. "Validation of the sodium void reactivity effect prediction using JEFF-3.1 nuclear data". In: *Annals of Nuclear Energy* 37.11 (2010), pp. 1534–1553. ISSN: 0306-4549. DOI: https://doi.org/10.1016/j.anucene.2010.06.010. URL: https://www.sciencedirect.com/science/article/pii/S0306454910002124.

[99] A. Jiménez-Carrascosa et al. "Nuclear data assimilation for Sodium-cooled Fast Reactors using integral experiments". In: *Spanish Nuclear Society Annual Meeting*. 2022, p. 10.

[100] Y. Wang et al. "Multi-parameter nuclear data adjustment for sodium fast reactor". In: *Progress in Nuclear Energy* 159 (2023), p. 104654. ISSN: 0149-1970. DOI: https://doi.org/10.1016/j.pnucene.2023.104654. URL: https://www.sciencedirect.com/science/article/pii/S0149197023000896.

[101] IAEA. "Liquid Metal Coolants for Fast Reactors Cooled by Sodium, Lead and Lead-Bismuth Eutectic". In: *IAEA Nuclear Energy Series No. NPT-1.6* (2012). URL: www.iaea.org/publications/8589/liquid-metal-coolants-for-fast-reactors-cooled-by-sodium-lead-and-lead-bismuth-eutectic.

[102] B. L. Broadhead et al. "Sensitivity-and uncertainty-based criticality safety validation techniques". In: *Nuclear science and engineering* 146.3 (2004), pp. 340–366. DOI: 10.13182/NSE03-2. URL: https://doi.org/10.13182/NSE03-2.

[103] A. Hoefer et al. "MOCABA: A general Monte Carlo–Bayes procedure for improved predictions of integral functions of nuclear data". In: *Annals of Nuclear Energy* 77 (2015), pp. 514–521. ISSN: 0306-4549. DOI: https://doi.org/10.1016/j.anucene.2014.11.038. URL: https://www.sciencedirect.com/science/article/pii/S0306454914006409.

Appendix A

Sensitivity output formats

In this appendix, different sensitivity coefficient formats are presented.
In listing A.1, the typical MCNP output section that is printed when the `KSEN` card is activated is shown. Here, the sensitivity profile relative to ^{239}Pu fission cross section is reported as an example. The left columns report the energy discretization, as requested in the input card. The energy ranges vary from the lowest to the highest energy. On the right, the sensitivity coefficients are presented in a column, along with their relative uncertainty for each energy group.

The second listing A.2 represents an MCNP output as well, but in this case, a separate file is produced while the code is running. This occurs when, for a `KCODE` calculation with a `KSEN` card selected, users also specify the option to print the sensitivity coefficient in different file formats. This can be obtained by adding the option `KSENTAL` to the card `KOPTS`. The most useful format is likely to be the `TSUNAMI-B`, since it reproduces the sensitivity data format *.sdf*, the most common and widespread in sensitivity analysis tools. It is worth noting that this option was not available before version 6.3.0 of the MCNP Monte Carlo code.

In this format, the energy discretization is specified at the beginning of the output file (*energy boundaries*), the energy ranges are ordered in descending order, and the units are keV instead of MeV present in MCNP output. A header block, which comprises lines 13-15 of the listing, indicates:

- the isotope using the ZAID identifier and the library used in the simulation;
- the reaction name;
- the nuclide number (specific for the simulation);
- the respective `MT` number of the reaction;

- the unit number
- the region number within unit;
- the total volume region, which is always zero for region-integrated profiles;
- Zone number or negative of material number;
- number of times region is referenced in the problem;
- material ID

Line 16 reports the energy-integrated sensitivity coefficients:

- the energy-integrated sensitivity coefficient for that profile;
- standard deviation for energy integrated sensitivity coefficient;
- sum of absolute values of the group-wise sensitivities;
- sum of the group-wise sensitivities with opposite sign as energy integrated value (osc);
- standard deviation for osc. group-wise sensitivity.

Finally, the group-wise sensitivity coefficients lines (17-23 in example A.2), are followed by the corresponding uncertainties (lines 24-30). For additional information on sensitivity data format, see [78].

Listing A.3 is structurally identical to the previous one, although it is obtained with a Python script during the post-processing. It can be generated both from the MCNP output file or after building the combined sensitivity vector for reactivity effect cases, to print the coefficient in this standardized format.

Listing A.1: Example of a sensitivity coefficient from MCNP output

```
 nuclear data keff sensitivity coefficients

      sensitivity profile      1
         94239.00c fission

             energy range (MeV)          sensitivity   rel. unc.

        1.1000E-10  1.0000E-07           0.0000E+00      0.0000
        1.0000E-07  5.4000E-07          -8.4788E-08      1.2951
        5.4000E-07  4.0000E-06           1.6688E-06      0.9175
        4.0000E-06  8.3153E-06           1.2817E-06      0.3720
        8.3153E-06  1.3710E-05           8.6806E-07      0.8115
        1.3710E-05  2.2603E-05           2.7689E-06      0.5121
        2.2603E-05  4.0169E-05           2.9089E-06      0.4849
        4.0169E-05  6.7904E-05           1.4678E-05      0.0763
        6.7904E-05  9.1661E-05           1.5825E-05      0.3265
        9.1661E-05  1.4863E-04           7.8865E-05      0.1024
        1.4863E-04  3.0432E-04           5.8143E-04      0.0307
        3.0432E-04  4.5400E-04           5.9307E-04      0.0258
        4.5400E-04  7.4852E-04           1.9220E-03      0.0097
        7.4852E-04  1.2341E-03           3.8575E-03      0.0089
        1.2341E-03  2.0347E-03           5.9119E-03      0.0080
        2.0347E-03  3.3546E-03           9.5403E-03      0.0044
        3.3546E-03  5.5308E-03           1.1260E-02      0.0052
        5.5308E-03  9.1188E-03           1.4214E-02      0.0062
        9.1188E-03  1.5034E-02           2.0721E-02      0.0047
        1.5034E-02  2.4788E-02           2.8281E-02      0.0033
        2.4788E-02  4.0868E-02           3.1952E-02      0.0028
        4.0868E-02  6.7379E-02           4.1828E-02      0.0023
        6.7379E-02  1.1109E-01           4.7300E-02      0.0029
        1.1109E-01  1.8316E-01           5.3126E-02      0.0026
        1.8316E-01  3.0197E-01           5.4268E-02      0.0026
        3.0197E-01  4.9787E-01           4.2186E-02      0.0015
        4.9787E-01  8.2085E-01           5.7054E-02      0.0013
        8.2085E-01  1.3534E+00           2.9312E-02      0.0033
        1.3534E+00  2.2313E+00           2.6958E-02      0.0015
        2.2313E+00  3.6788E+00           2.2079E-02      0.0034
        3.6788E+00  6.0653E+00           9.5826E-03      0.0034
        6.0653E+00  1.0000E+01           2.7455E-03      0.0051
        1.0000E+01  1.9640E+01           2.0391E-04      0.0334
```

Listing A.2: Example of MCNP output when `KSENTAL=TSUNAMI-B` card is activated

```
mcnp66 keff nuclear data sensitivity      1 in tsunami-b format.
        33 number of neutron groups
       217   number of sensitivity profiles           0 are region integrated
  1.000849 +/-   0.000020  k-eff from the forward case
energy boundaries:
  1.964033E+07  1.000000E+07  6.065307E+06  3.678794E+06  2.231302E+06
  1.353353E+06  8.208500E+05  4.978707E+05  3.019738E+05  1.831564E+05
  1.110900E+05  6.737947E+04  4.086771E+04  2.478752E+04  1.503439E+04
  9.118820E+03  5.530844E+03  3.354626E+03  2.034684E+03  1.234098E+03
  7.485183E+02  4.539993E+02  3.043248E+02  1.486254E+02  9.166088E+01
  6.790405E+01  4.016900E+01  2.260329E+01  1.370959E+01  8.315287E+00
  4.000000E+00  5.400000E-01  1.000000E-01  1.100000E-04
94239.00c    fission     36     18
      0      0
  0.000000E+00  0.000000E+00       0      0
  5.160748E-01  3.870785E-04  5.160755E-01 -3.701032E-07  6.521087E-07
  2.019998E-04  2.786303E-03  9.657998E-03  2.211977E-02  2.689256E-02
  2.910077E-02  5.722976E-02  4.216229E-02  5.411471E-02  5.337274E-02
  4.746253E-02  4.178152E-02  3.218336E-02  2.834913E-02  2.078908E-02
  1.416238E-02  1.134640E-02  9.359989E-03  5.897450E-03  3.841259E-03
  1.953660E-03  5.747639E-04  6.096684E-04  7.917022E-05  2.081315E-05
  1.808262E-05 -4.070492E-08  2.520119E-06  8.084702E-07  1.134459E-06
  2.499222E-06 -3.293983E-07  4.645052E-08
  5.533279E-06  1.994206E-05  4.502941E-05  5.912479E-05  8.150354E-05
  6.397310E-05  1.215679E-04  1.405516E-04  1.622914E-04  1.273140E-04
  9.752889E-05  1.186158E-04  7.695074E-05  4.901382E-05  9.620118E-05
  7.236744E-05  4.962902E-05  4.445658E-05  3.888036E-05  4.124193E-05
  3.775724E-05  1.528685E-05  1.748733E-05  5.502450E-06  2.750180E-06
  1.849496E-06  5.369502E-07  1.798457E-06  9.028110E-07  5.268112E-07
  1.268096E-06  3.700407E-07  2.938082E-08
```

Listing A.3: Example of .sdf output obtained with post-processing tool

```
sensitivity coefficients MCNP in .sdf format
        33 number of neutron groups
        37 number of sensitivity profiles            37 are nuclide integrated
  1.000849 +/-   0.000020  k-eff from the forward case
energy boundaries:
  1.964033E+07  1.000000E+07  6.065307E+06  3.678794E+06  2.231302E+06
  1.353353E+06  8.208500E+05  4.978707E+05  3.019738E+05  1.831564E+05
  1.110900E+05  6.737947E+04  4.086771E+04  2.478752E+04  1.503439E+04
  9.118820E+03  5.530844E+03  3.354626E+03  2.034684E+03  1.234098E+03
  7.485183E+02  4.539993E+02  3.043248E+02  1.486254E+02  9.166088E+01
  6.790405E+01  4.016900E+01  2.260329E+01  1.370959E+01  8.315287E+00
  4.000000E+00  5.400000E-01  1.000000E-01  1.100000E-04
pu-239          fission         94239           18
      0      0
  0.000000E+00  0.000000E+00      0      0
  5.160748E-01  3.870785E-04  5.160755E-01 -3.701032E-07  6.521087E-07
  2.019998E-04  2.786303E-03  9.657998E-03  2.211977E-02  2.689256E-02
  2.910077E-02  5.722976E-02  4.216229E-02  5.411471E-02  5.337274E-02
  4.746253E-02  4.178152E-02  3.218336E-02  2.834913E-02  2.078908E-02
  1.416238E-02  1.134640E-02  9.359989E-03  5.897450E-03  3.841259E-03
  1.953660E-03  5.747639E-04  6.096684E-04  7.917022E-05  2.081315E-05
  1.808262E-05 -4.070492E-08  2.520119E-06  8.084702E-07  1.134459E-06
  2.499222E-06 -3.293983E-07  4.645052E-08
  5.533279E-06  1.994206E-05  4.502941E-05  5.912479E-05  8.150354E-05
  6.397310E-05  1.215679E-04  1.405516E-04  1.622914E-04  1.273140E-04
  9.752889E-05  1.186158E-04  7.695074E-05  4.901382E-05  9.620118E-05
  7.236744E-05  4.962902E-05  4.445658E-05  3.888036E-05  4.124193E-05
  3.775724E-05  1.528685E-05  1.748733E-05  5.502450E-06  2.750180E-06
  1.849496E-06  5.369502E-07  1.798457E-06  9.028110E-07  5.268112E-07
  1.268096E-06  3.700407E-07  2.938082E-08
```

Appendix B

Generalized-Linear-Least-Square: formal derivation

This appendix presents two complementary derivations of the Generalized Linear Least Squares (GLLS) method used in the thesis. Both approaches are well established in the nuclear data community [102, 88, 91]. The first uses a Bayesian framework with Gaussian priors and likelihoods (derived from the MOCABA equation [103]). In contrast, the second can be obtained from a generalized least-squares minimization (adapted from NUREG/CR-6655, Appendix B [76]).

Bayesian derivation In a Bayesian interpretation, the nuclear data vector $\boldsymbol{\sigma}$ is modeled as a random variable with a Gaussian prior distribution:

$$p(\boldsymbol{\sigma}) \propto \exp\left[-\frac{1}{2}(\boldsymbol{\sigma}-\boldsymbol{\sigma}_0)^T \mathbf{M}_\sigma^{-1}(\boldsymbol{\sigma}-\boldsymbol{\sigma}_0)\right] \quad ,$$

where $\boldsymbol{\sigma}_0$ and $\mathbf{M}_\sigma$ denote the prior mean and covariance, respectively.

Measurements $\mathbf{E}$ of integral quantities are assumed to be related to the model predictions $\mathbf{C}(\boldsymbol{\sigma})$ through

$$\mathbf{E} = \mathbf{C}(\boldsymbol{\sigma}) + \boldsymbol{\varepsilon} \quad ,$$

with Gaussian-distributed errors $\boldsymbol{\varepsilon} \sim \mathcal{N}(\mathbf{0}, \mathbf{R})$, where the covariance matrix $\mathbf{R} = \mathbf{M}_E + \mathbf{M}_M$ includes both experimental and modeling uncertainties.

The likelihood of observing $\mathbf{E}$ for a given $\boldsymbol{\sigma}$ is therefore

$$p(\mathbf{E} \mid \boldsymbol{\sigma}) \propto \exp\left[-\frac{1}{2}(\mathbf{E}-\mathbf{C}(\boldsymbol{\sigma}))^T \mathbf{R}^{-1}(\mathbf{E}-\mathbf{C}(\boldsymbol{\sigma}))\right] \quad .$$

Since $\mathbf{C}(\boldsymbol{\sigma})$ is nonlinear in the nuclear data, we linearize it about the nominal prior $\boldsymbol{\sigma}_0$:

$$\mathbf{C}(\boldsymbol{\sigma}) \approx \mathbf{C}(\boldsymbol{\sigma}_0) + \mathbf{S}(\boldsymbol{\sigma} - \boldsymbol{\sigma}_0) \quad , \tag{B.1}$$

where $\mathbf{S}$ is the sensitivity matrix $\mathbf{S} = \partial\mathbf{C}/\partial\boldsymbol{\sigma}|_{\boldsymbol{\sigma}_0}$.

Applying Bayes' theorem gives the posterior distribution:

$$p(\boldsymbol{\sigma} \mid \mathbf{E}) \propto p(\mathbf{E} \mid \boldsymbol{\sigma})\, p(\boldsymbol{\sigma}) \quad .$$

Substituting the linearized likelihood and the Gaussian prior, and completing the square, leads to a Gaussian posterior with mean $\boldsymbol{\sigma}' = \boldsymbol{\sigma}_0 + \Delta\boldsymbol{\sigma}$ and covariance $\mathbf{M}'_\sigma$ given by

$$\Delta\boldsymbol{\sigma} = \mathbf{M}_\sigma \mathbf{S}^T \left[\mathbf{S}\mathbf{M}_\sigma\mathbf{S}^T + \mathbf{M}_E + \mathbf{M}_M\right]^{-1} \left[\mathbf{E} - \mathbf{C}(\boldsymbol{\sigma}_0)\right] \quad , \tag{B.2}$$

$$\mathbf{M}'_\sigma = \mathbf{M}_\sigma - \mathbf{M}_\sigma \mathbf{S}^T \left[\mathbf{S}\mathbf{M}_\sigma\mathbf{S}^T + \mathbf{M}_E + \mathbf{M}_M\right]^{-1} \mathbf{S}\mathbf{M}_\sigma \quad . \tag{B.3}$$

Equations (B.2)–(B.3) correspond to the so-called GLLS update equations. In the Bayesian interpretation, the posterior mean is the most probable nuclear data vector given the prior and experimental information.

Generalized Least-Squares Derivation Here, the derivation is presented in a consistent notation with the Bayesian formulation to underscore their equivalence.

Let the vector of nuclear data parameters be $\boldsymbol{\sigma}$ with prior estimate $\boldsymbol{\sigma}_0$ and prior covariance matrix $\mathbf{M}_\sigma$. Integral measurements are collected in the vector $\mathbf{E}$ with associated covariance matrix $\mathbf{R}$. The model prediction of these experiments is given by $\mathbf{C}(\boldsymbol{\sigma})$, which depends on the nuclear data. Linearizing the model around the prior yields

$$\mathbf{C}(\boldsymbol{\sigma}) \simeq \mathbf{C}(\boldsymbol{\sigma}_0) + \mathbf{S}(\boldsymbol{\sigma} - \boldsymbol{\sigma}_0) \quad , \tag{B.4}$$

where $\mathbf{S}$ is the sensitivity matrix with elements $S_{ij} = \partial C_i/\partial\alpha_j$.

Define the residual between the experimental and calculated values at the prior as

$$\mathbf{d} = \mathbf{E} - \mathbf{C}(\boldsymbol{\sigma}_0) \quad , \tag{B.5}$$

and the parameter update $\Delta\boldsymbol{\sigma} = \boldsymbol{\sigma} - \boldsymbol{\sigma}_0$. Assuming small deviations and linear consistency between adjusted model and measurement data, the adjusted responses satisfy

$$\mathbf{y} = \mathbf{d} - \mathbf{S}\,\Delta\boldsymbol{\sigma} \quad , \tag{B.6}$$

where $\mathbf{y}$ represents the remaining mismatch after adjustment.

The GLLS method determines $\Delta\boldsymbol{\sigma}$ by minimizing a quadratic form that weights deviations according to their prior covariances:

$$Q(\Delta\boldsymbol{\sigma}, \mathbf{y}) = \frac{1}{2} \begin{pmatrix} \mathbf{y} \\ \Delta\boldsymbol{\sigma} \end{pmatrix}^T \mathbf{C}^{-1} \begin{pmatrix} \mathbf{y} \\ \Delta\boldsymbol{\sigma} \end{pmatrix}, \qquad \mathbf{C} = \begin{pmatrix} \mathbf{R} & \mathbf{C}_{\sigma E}^T \\ \mathbf{C}_{\sigma E} & \mathbf{M}_\sigma \end{pmatrix} \quad , \tag{B.7}$$

subject to the linear constraint (B.6). The off-diagonal block $\mathbf{C}_{\sigma E}$ represents the cross-covariance between model parameters and measurements, which can be retained for generality but is often neglected in first-order adjustments.

Introducing a vector of Lagrange multipliers $\boldsymbol{\lambda}$, the problem is recast as the unconstrained minimization of

$$\mathcal{R}(\Delta\boldsymbol{\sigma}, \mathbf{y}, \boldsymbol{\lambda}) = Q(\Delta\boldsymbol{\sigma}, \mathbf{y}) + \boldsymbol{\lambda}^T \big(\mathbf{y} + \mathbf{S}\,\Delta\boldsymbol{\sigma} - \mathbf{d}\big) \quad . \tag{B.8}$$

Setting the partial derivatives of $\mathcal{R}$ with respect to $\Delta\boldsymbol{\sigma}$, $\mathbf{y}$, and $\boldsymbol{\lambda}$ to zero leads to the following first-order conditions:

$$\mathbf{C}_{\Delta\sigma\Delta\sigma}^{-1}\,\Delta\boldsymbol{\sigma} + \mathbf{C}_{\Delta\sigma y}^{-1}\,\mathbf{y} + \mathbf{S}^T\boldsymbol{\lambda} = 0 \quad , \tag{B.9}$$

$$\mathbf{C}_{yy}^{-1}\,\mathbf{y} + \mathbf{C}_{y\Delta\sigma}^{-1}\,\Delta\boldsymbol{\sigma} + \boldsymbol{\lambda} = 0 \quad , \tag{B.10}$$

$$\mathbf{y} + \mathbf{S}\,\Delta\boldsymbol{\sigma} - \mathbf{d} = 0 \quad . \tag{B.11}$$

Eliminating $\mathbf{y}$ and $\boldsymbol{\lambda}$ yields a linear system for $\Delta\boldsymbol{\sigma}$. Neglecting cross-covariances ($\mathbf{C}_{\sigma E} = \mathbf{0}$) and simplifying, the solution becomes

$$\Delta\boldsymbol{\sigma} = \mathbf{M}_\sigma \mathbf{S}^T \big(\mathbf{S}\,\mathbf{M}_\sigma\,\mathbf{S}^T + \mathbf{R}\big)^{-1} \big[\mathbf{E} - \mathbf{C}(\boldsymbol{\sigma}_0)\big] \quad . \tag{B.12}$$

The update depends on the prior uncertainty $\mathbf{M}_\sigma$, the sensitivities $\mathbf{S}$, and the total experimental covariance $\mathbf{S}\mathbf{M}_\sigma\mathbf{S}^T + \mathbf{R}$.

The covariance of the adjusted parameters $\boldsymbol{\sigma}^* = \boldsymbol{\sigma}_0 + \Delta\boldsymbol{\sigma}$ follows from the propagation of uncertainties through the same linear model. The resulting posterior covariance is

$$\mathbf{M}_\sigma^* = \mathbf{M}_\sigma - \mathbf{M}_\sigma\,\mathbf{S}^T \big(\mathbf{S}\,\mathbf{M}_\sigma\,\mathbf{S}^T + \mathbf{R}\big)^{-1} \mathbf{S}\,\mathbf{M}_\sigma \quad . \tag{B.13}$$

Equivalence with the Bayesian formulation Comparing Eqs. (B.12) and (B.13) with the corresponding results from the Bayesian formulation (Eqs. (B.2) and (B.4)) show that the two approaches are algebraically identical under the linearization approximation (B.4). In their current form, these equations are usually suited for use in the nuclear data adjustment field, whereas for nuclear criticality

safety assessment, they are used in the form presented in chapter 2. Substantially, since there is no interest in obtaining posterior value for cross sections in input, $\boldsymbol{\Delta}\sigma$ is inserted in Equation (B.1) to obtain the posterior value for the quantity of interest, that is k_{eff} in this study. Conversely, the posterior covariance matrix is directly inserted in the sandwich formula to obtain the posterior uncertainty for the application case.